

# **Micro-tensile creep testing for polycrystalline and single crystalline nickel-based high temperature alloys**

Zur Erlangung des akademischen Grades eines  
**Doktors der Ingenieurwissenschaften (Dr.-Ing.)**  
von der KIT - Fakultät für Maschinenbau des  
Karlsruher Instituts für Technologie (KIT)

angenommene

**Dissertation**

von

M.Sc. LiKang Luan  
aus Shanghai, China

Tag der mündlichen Prüfung: 29. 01. 2020

Hauptreferent: Prof. Dr. Martin Heilmaier

Korreferent: Prof. Dr. Thomas Böhlke



# Abstract

Creep test is one important mechanical testing method to ensure a suitable working condition and lifetime prediction for components such as turbine blades in a high-temperature working environment. For a higher energy density, the miniaturization of such components is continuously developed resulting in the urgent demand for the development of small scale creep testing and the understanding of the influence of specimen miniaturization on creep behavior.

The main aim of this thesis is to gain fundamental knowledge about the creep behavior of miniaturized specimens at sub-mm scale and up to a temperature of 1000 °C. A customized setup was designed for micro-tensile creep testing under constant load and stress. A contactless strain measurement based on digital image correlation (DIC) was developed, which enables the analysis of the strain distribution evolution on the specimen surfaces. The creep behavior of the dog-bone shaped miniaturized specimens of Nimonic 75 polycrystal and NiAl single crystals in different sizes was analyzed and compared with the creep behavior of the conventional specimens in mm scale at the similar experimental conditions.

The influence of specimen miniaturization on the creep behavior is dependent on multiple factors: Nimonic 75 polycrystalline miniaturized specimens showed a “thickness debit effect” that reduced creep resistance was observed due to the intergranular cracks generated from the specimen surfaces resulting in strain localization. Meanwhile, the creep behavior of NiAl single crystalline miniaturized specimens shows a “size effect” that decreasing creep strain rate was observed in specimens with increasing length to

square of thickness ratio ( $L/h^2$ ) because of a larger density of the geometrically necessary dislocations (GND) generated by the setup misalignment due to the accuracy limitation. The influence of the GNDs on the creep behavior showed a dependence on the crystal orientation because of the different dominated creep mechanism, i.e.,  $\langle 100 \rangle$  dislocation glide in [110] soft orientation and sessile  $\langle 110 \rangle$  dislocation glide via  $\langle 100 \rangle$  dislocation climb in [100] hard orientation.

# Kurzfassung

Der Kriechversuch ist eine wichtige mechanische Prüfmethode, um einen geeigneten Betriebszustand und eine Lebensdauervorhersage für Komponenten wie Turbinenblätter unter Hochtemperaturbeanspruchung sicherzustellen. Zur Erreichung einer höheren Energiedichte wird die Miniaturisierung solcher Komponenten kontinuierlich weiterentwickelt. Dadurch entsteht ein dringender Bedarf nach der Entwicklung von Kriechversuchen für kleine Probengeometrien und nach Kenntnissen des Einflusses der Miniaturisierung von Proben auf das Kriechverhalten.

Das Hauptziel dieser Arbeit ist, eine vertiefte Kenntnis über das Kriechverhalten miniaturisierter Proben in der Submillimeterskala bis zu einer Temperatur von 1000 °C zu erlangen. Für den Mikrozug-Kriechversuch unter konstanter Kraft und Spannung wurde ein selbstentwickelter Versuchsstand verwendet. Es wurde eine berührungslose Dehnungsmessung basierend auf der digitalen Bildkorrelation (DIC) entwickelt, mit der die Entwicklung der Dehnungsverteilung auf den Probenoberflächen analysiert werden kann. Das Kriechverhalten von hundeknochenförmigen miniaturisierten Proben von Nimonic 75-Polykristall- und NiAl-Einkristallen in verschiedenen Größen wurde analysiert und verglichen mit den üblichen Proben im mm-Maßstab bei ähnlichen Versuchsbedingungen.

Der Einfluss der Probenminiaturisierung auf das Kriechverhalten ist von mehreren Faktoren abhängig: miniaturisierte polykristalline Nimonic 75 Proben zeigten einen “thickness debit” Effekt. Eine weniger gute Kriechbeständigkeit wurde aufgrund der von den Probenoberflächen erzeugten intergranularen Risse beobachtet, die eine stärkere Dehnungslokalisierung

verursachen. Das Kriechverhalten von einkristallinen miniaturisierten NiAl-Proben zeigt einen Größeneffekt, demzufolge eine niedrigere Kriechrate bei Proben mit größerem Verhältnis von Länge zum Quadrat der Dicke ( $L/h^2$ ) beobachtet wurde, die eine erhöhte Dichte von geometrisch notwendigen Versetzungen (Geometrically Necessary Dislocations - GND) aufwiesen. Der Einfluss der GNDs auf das Kriechverhalten zeigte eine Abhängigkeit von der Kristallorientierung aufgrund des unterschiedlichen dominierten Kriechmechanismus, d.h.  $\langle 100 \rangle$  Versetzungsgleiten in  $[110]$  weicher Orientierung und sessile  $\langle 110 \rangle$  Versetzungsgleiten durch  $\langle 100 \rangle$  Versetzungsklettern in  $[100]$  harter Orientierung.

# Contents

<b>Abstract</b> . . . . .	<b>i</b>
<b>Kurzfassung</b> . . . . .	<b>iii</b>
<b>1 Introduction and background</b> . . . . .	<b>1</b>
1.1 Motivation of specimen miniaturization . . . . .	1
1.2 Small scale creep testing . . . . .	4
1.2.1 Setup miniaturization . . . . .	6
1.2.2 Specimen miniaturization . . . . .	8
1.2.3 Material selection . . . . .	15
1.3 Thesis overview . . . . .	16
<b>2 Development of high temperature tensile creep setup</b> . .	<b>19</b>
2.1 Design of miniaturized specimens . . . . .	19
2.2 Design of adapter . . . . .	21
2.3 Design of customized tensile creep setup . . . . .	22
2.3.1 Heating method . . . . .	22
2.3.2 Load and displacement control . . . . .	24
2.3.3 Measurement uncertainty in stress . . . . .	24
2.3.4 Influence of oxidation . . . . .	25
2.4 Strain measurement with Digital Image Correlation (DIC) . .	26
2.4.1 Basic principles . . . . .	26
2.4.2 Strain rate calculation . . . . .	29
2.5 DIC influencing factors . . . . .	31

2.5.1	Theoretical accuracy . . . . .	31
2.5.2	Subset size influence . . . . .	33
2.5.3	Room temperature test . . . . .	36
2.5.4	High temperature test at 1000 °C . . . . .	38
2.5.5	Update of reference images in longtime tests . . . . .	40
2.6	Constant stress test . . . . .	42
<b>3</b>	<b>Tensile creep testing of Nimonic 75 polycrystal . . . . .</b>	<b>45</b>
3.1	Specimen preparation . . . . .	45
3.2	Experimental results . . . . .	46
3.3	Characterization of the miniaturized specimens . . . . .	54
3.3.1	Analysis of strain distribution . . . . .	54
3.3.2	Influence of crack generation . . . . .	56
3.3.3	Influence of oxidation . . . . .	63
3.4	Summary for Nimonic 75 miniaturized specimens . . . . .	67
<b>4</b>	<b>Tensile creep testing of NiAl single crystals . . . . .</b>	<b>69</b>
4.1	Specimen preparation . . . . .	70
4.2	Tensile creep testing in [110] soft orientation . . . . .	71
4.2.1	Experimental results . . . . .	71
4.2.2	Fracture surface and slip systems . . . . .	77
4.2.3	Analysis of strain distribution . . . . .	83
4.2.4	Influence of stress localization . . . . .	90
4.2.5	Influence of oxidation . . . . .	91
4.2.6	Geometrically Necessary Dislocations (GND) de- termination with EBSD . . . . .	95
4.2.7	Influence of GNDs on creep behavior . . . . .	104
4.2.8	Accuracy of the GND determination . . . . .	113
4.2.9	Equivalent GND determination with the DIC method	115



---

4.2.10	Summary for NiAl miniaturized specimens in [110] soft orientation . . . . .	123
4.3	Tensile creep testing in [100] hard orientation . . . . .	124
4.3.1	Experimental results . . . . .	124
4.3.2	Fracture surface and slip systems . . . . .	127
4.3.3	Analysis of strain distribution . . . . .	133
4.3.4	Influence of oxidation . . . . .	137
4.3.5	Geometrically Necessary Dislocations (GND) determination with EBSD . . . . .	138
4.3.6	Tensile creep testing at different temperatures . . . . .	141
4.3.7	Summary for NiAl miniaturized specimens in [100] hard orientation . . . . .	143
<b>5</b>	<b>Summary . . . . .</b>	<b>145</b>
<b>6</b>	<b>Outlook . . . . .</b>	<b>147</b>
<b>A</b>	<b>Appendix . . . . .</b>	<b>151</b>
	<b>References . . . . .</b>	<b>156</b>



# 1 Introduction and background

## 1.1 Motivation of specimen miniaturization

In 1959, Richard Feynman gave his famous talk “There is plenty of room at the bottom” [1]. He was the first to envision the importance of manipulating and controlling things on a small scale, i.e., miniaturization. Nowadays, many applications benefited from miniaturization are already available in our daily life: the performance of any modern smartphone overwhelms the computing machines in that time, whose sizes were huge and filled rooms. Capsule sized medical robot can be used to check health status by merely swallowing it, etc. One of the most important application fields of the miniaturization technology is in the aerospace and aircraft industries. For example, gas turbine blades with new structure, such as cooling holes or reduced thickness [2–5] are developed to increase the energy efficiency by increasing working temperature or reducing weight, which is both economically and environmentally beneficial. With the development of the microelectronics industry in the 1970s, gas turbine systems in millimeter-scale can be produced due to the development of micromachining capability based on semiconductor manufacturing techniques, devices manufactured by this method are known as micro-electro-mechanical systems (MEMS) [4]. Such a small gas turbine system can provide a higher energy density than the best batteries available today, which is a promising candidate for mobile devices such as ground robots and small aircraft.

To ensure the reliability and performance of these devices at high-temperature working conditions, their mechanical properties should be systematically

studied. Creep test is one important mechanical testing method for these devices. For example, the turbine blades are continuously under centrifugal load in the working condition, the time-dependent deformation of the turbine blades needs to be systematically analyzed at different temperatures and stress to ensure a suitable working condition and lifetime prediction. Specimens for creep test need to be modified to fit the actual size of the turbine blades, i.e., specimen miniaturization is necessary. The reason is that creep test results with conventional specimens in centimeter or millimeter scale can't represent the actual performance of the turbine blades, which have complicated structure or endure inhomogeneous stress distribution due to cooling holes or reduced thickness. By miniaturizing specimen sizes, material from various regions of interest can be separately cut out so that the heterogeneous local mechanical properties can be explicitly researched. For material that is difficult to manufacture in massive parts, such as multilayer or direction solidification alloys, it is not economically and scientifically feasible to use conventional specimens in this kind of material, because the amount of material is usually not sufficient for mechanical testing with conventional specimens, and the increased demand for bulk material also raises the cost. The designed structure in this kind of material is generally not perfect as expected, defects such as misalignment of the fibrous or lamellar microstructure in the directionally solidified alloys can lead to cellular or dendritic regions [6], which contain different material properties compared to the designated well-aligned structure. Therefore, the testing results with conventional specimens can't represent the true material properties when such defects exist in the specimens. With miniaturized specimens, multiple tests for a systematic and reproducible study of the mechanical properties in the limited area of the bulk material is possible. Additionally, the miniaturized specimens can be manufactured in different directions from the bulk material to study the orientation dependence on the mechanical properties [7]. Besides these mentioned advantages of specimen miniaturization, some scientifically interesting features of miniaturized specimens

with sizes into the micrometer regime appear: the mechanical properties of material follow no longer the general scaling laws, but contain various extraordinary properties. Early work in the year 1956 from Brenner [8, 9] demonstrated that the specimen size of small whiskers is important to the material properties that increased material strengths were detected with decreasing specimen sizes, which were close to the lower estimated strength of perfect crystals. They have also found the whiskers exhibited extremely sharp yield points and extensive easy “glide” regions due to the propagation of the Lüders bands, then a repeated yielding was observed because propagation of the Lüders bands were obstructed in the plastic region. With the development of Scanning Electron Microscope (SEM) and Focused Ion Beam (FIB), Uchic et al. [10] have done the first pillar compression with diameters from 5 to 40  $\mu\text{m}$  in 2004 and found increased mechanical strength in Ni single crystalline micropillars with smaller diameter. This extraordinary “smaller is stronger” phenomenon, which is also known as “size effect”, arises the problem that the mechanical properties are unable to be predicted and quantified at this scale. At elevated temperature in creep tests, additional factors such as diffusion or oxidation influence the creep behavior of miniaturized specimens. Seetharaman et al. [11] have reported a thickness debit effect in the PWA 1484 superalloy in creep testing: reduced rupture life was observed in the miniaturized specimens with decreasing thickness from 3.18 mm to 0.38 mm due to enhanced stress concentration around the interdendritic voids formed during creep deformation. The complex experimental environment of the miniaturized specimens in creep testing results in enhanced difficulty to predict the material properties in such a situation, because multiple influencing factors such as increased demand for experimental setup stability, specimen sizes, and surface oxidation, etc., need to be considered. There exists an urgent demand for the fundamental understanding of the creep mechanisms in sub-mm scale, because industry keeps pushing devices to even smaller sizes for cost-saving or increasing efficiency.

Therefore the main aim of this thesis is to gain further fundamental knowledge about the creep behavior of miniaturized specimens in sub-mm scale up to temperature 1000 °C. To fulfill this purpose, a suitable experimental setup needs to be developed. The creep behavior of miniaturized specimens needs to be analyzed based on different influencing factors such as specimen sizes, material microstructure, and oxidation. Creep behaviors between conventional specimens and miniaturized specimens will be compared and their difference will be analyzed to get further knowledge about the influence of specimen miniaturization on the creep behavior.

The basic working principle of creep test and the conventional creep machine will be introduced in the next section for a better understanding of the technical challenges of creep test with miniaturized specimens. Some recent works of small scale mechanical testing will then be introduced as a guideline for the experimental plan for material selection, appropriate specimen size and geometry for the micro-creep testing.

## **1.2 Small scale creep testing**

Creep is a time-dependent deformation, which means material can deform slowly and permanently at a constant temperature under stresses even below the yield strength [12]. Figure 1.1 (a) shows a typical creep curve. A creep curve usually has three stages: the primary stage as the first stage which normally represents a region of decreasing creep rate, creep resistance is increased in this stage due to working hardening. In the secondary stage, the strain rate reaches a minimum and becomes near constant due to the balance between the working hardening and recovery process. Therefore the secondary stage is also called steady-state creep stage. The minimum or steady-state strain rate is one of the most important material properties in creep tests. It is dependent on the experimental temperature and stress and is also considered as one important engineering design criterion [12]. For

example, the creep of turbine blades causes contact between the blades and the casing. To prevent this damage, the lifetime of turbine blades needs to be predicted by measuring the minimum, or steady-state creep strain rate under the actual working condition, thus the blades can be repaired or replaced before damage appears. In the tertiary stage, the strain rate increases because of necking phenomena or internal damage in specimens, which leads to increased stress resulting in specimen fracture.

To study the creep behavior of specimens with miniaturized sizes, there are some technical challenges in the design of the experimental setup. For a better understanding of the challenges of creep test with miniaturized specimens, a typical creep machine will be first introduced, then the technical challenges for the testing of conventional specimens will be discussed. Figure 1.1 (b) sketches the setup of a typical creep machine.

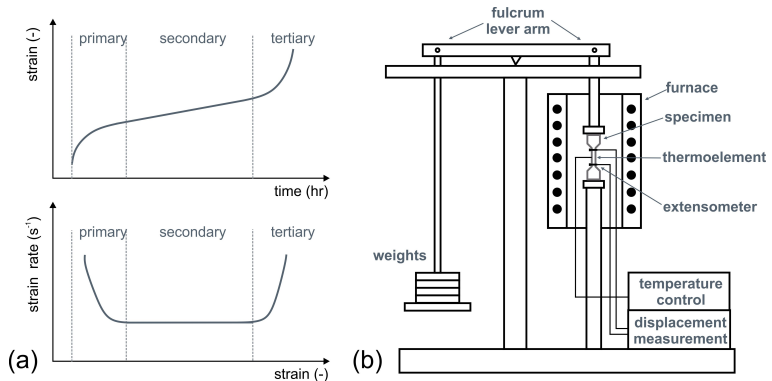


Figure 1.1: Schematic diagram of one typical creep testing machine.

In creep tests, the specimen is fixed with two pull rods in the middle of the furnace and heated to the designated temperature. The temperature on the specimen is measured usually with a thermocouple, which provides a feedback signal to the temperature control system to maintain the designated temperature. Once the stable temperature condition is reached, a constant

load or engineering stress will be added on the specimens by activating the corresponding weights on the end of the fulcrum lever arm. The strain measurement is generally achieved by using an extensometer in the gauge length of the specimen. The length increment is measured and converted into the strain value. For precise test results, the load or stress and the temperature on the specimen should be maintained constant, simultaneously, accurate strain measurement from the gauge length is also necessary.

### 1.2.1 Setup miniaturization

The challenges of setup miniaturization for micro creep tests are the increased requirements of accuracy and stability in temperature, stress control and strain measurement due to the miniaturized specimen sizes.

For the temperature control, the miniaturized specimens can be either heated resistively, which means the miniaturized specimens are heated by using integrated heaters on themselves, or be heated globally in a furnace. The disadvantage of the resistive heating is that the temperature distribution is not homogenous, especially a local increase of temperature is inevitable when necking takes place in the strained miniaturized specimens [13–16]. Leisen et al. [17] has developed a furnace heating method with a resistance heating via a spiral-shaped Kanthal A1 wire for tensile tests with SiC thin films up to a temperature of 1000°C, with a thermocouple placed on the specimen surface for temperature measurement. This furnace heating method has an accuracy of temperature control better than  $\pm 1$  °C. We have chosen the furnace heating method with a similar design from Leisen’s work for the micro creep tests in this study, because the temperature control with this method is independent of the electrical and thermal properties of the miniaturized specimens.

Load control with weights and the fulcrum lever arm is no longer a reliable choice for miniaturized specimens, because the minimum weight block limits the load accuracy, even though smaller weight blocks could be used, the



deteriorated precision of weight due to abrasion or pollution after multiple creep tests result in load accuracy error. Instead, a combination of a load cell and an actuator is one good solution, since the accuracy of a load cell can reach nowadays in the mN range and the minimum step size of an actuator is in  $\mu\text{m}$  or even smaller.

Considering the size of the miniaturized specimens, the strain measurement with a common extensometer is not suitable. A straightforward alternative is to measure the crosshead displacement of the miniaturized specimens and convert it into a strain value. However, Zhao et al. [18] have analyzed the influence of variations of specimen geometry on the experimental strain measurements from the crosshead displacement of miniaturized dog bone shape tensile specimens in sub-millimeter scale. They have found that the uniform elongation and the post-necking elongation both increase with increasing specimen thickness and decreasing gauge length: For specimens with a gauge length of 1 mm with increasing thickness from 250  $\mu\text{m}$  to 2100  $\mu\text{m}$ , the uniform elongation increased from 154% to 192%, and the post-necking elongation increased from 34% to 110%. Meanwhile, for specimens with a fixed thickness of 250  $\mu\text{m}$  with decreasing gauge length from 10 mm to 1 mm, the uniform elongation increased from 41% to 154% and the post-necking elongation increased from 5% to 34%. Sharpe et al. [19] have developed a laser-based technique named ISDG that enables a contactless strain measurement on a thin-film specimen in micrometer scale, which has a resolution of 5 microstrain and relative uncertainty of  $\pm 3\%$ . They place two reflective markers on a specimen and illuminate them with a laser so that interference fringe patterns can be generated, the fringes move as the specimen is strained and the motion is recorded with photodiode arrays for strain calculation. However, this method of strain measurement is possibly not suitable in high-temperature creep test, because the surface oxidation may deteriorate the quality of reflective markers resulting in strain error. A more recent direct method for strain measurement is Digital Image Correl-

ation (DIC). Digital Image Correlation is an optical method that analyzes the deformation of the specimen surface by comparing a series of images before and after deformation [20]. This measurement method was first developed by a group of researchers at the University of South Carolina in the 1980s [21–25]. During the past few years, the DIC method is continuously optimized and applied even at elevated temperatures [26–29], which makes DIC a promising method of strain measurement for miniaturized specimens in high-temperature creep testing. Simultaneously, analysis of strain distribution on the specimen surface is available with DIC method [30–32] so that the evolution of strain localization can be analyzed for a better understanding of the creep damage behavior in the later stages of creep on conventional and miniaturized specimens.

### **1.2.2 Specimen miniaturization**

When the specimen size is miniaturized into micrometer scale, material mechanical properties follow no longer the general scaling laws, but show a “smaller is stronger” phenomenon, i.e., the mechanical “size effect”. Several review articles [33–36] conclude the most important findings and the understanding of the mechanical size effect, which can be classified into two broad categories: intrinsic and extrinsic size effects. The intrinsic size effect is related to the variation of the microstructure in materials. One well-known example of the intrinsic size effect is the influence of the grain sizes on the mechanical properties, which was first reported by Hall and Petch [37, 38]: the grain boundaries act as obstacles to the dislocation motion resulting in dislocation pile-up on the grain boundaries so that increased strength in the material can be observed, which is the so-called “Hall-Petch” relationship. But when the grain sizes are reduced to nm scale, decreased material strength is detected in several systems such as Cu and Ni resulting in an “inverse Hall-Petch” phenomenon [39, 40]. The extrinsic size effect is related to the specimen dimensions. The mechanical properties such as

increased flow stress or stronger strain hardening are strongly influenced, when one or more dimensions of the specimen size are in the range or below micrometer scale [41]. Numerous studies have been done to research the extrinsic size effect, there exist several theories to explain the different mechanical properties in scale from nanometer to micrometer, such as dislocation starvation theory [42], strain gradient plasticity theory [43] and dislocation pile-up due to the specimen geometry [44], etc. This indicates that the extrinsic size effect can't be simply explained with one single mechanism. Different mechanisms dominate or co-exist influencing the mechanical properties at different boundary conditions. Therefore various aspects should be considered for the specimen miniaturization for creep testing.

The **first aspect** is the determination of a suitable specimen size. Some recent works on the impact of extrinsic size effect at room temperature and the corresponding main influencing factors of mechanical properties will be first introduced as a guideline of specimen miniaturization for micro creep testing. Uchic et al. [10] did the first pillar compression in 2004. Single crystal micropillars with diameters from 5 to 40  $\mu\text{m}$  were manufactured with a focused ion beam (FIB) microscope and tested with a nanoindenter under compressive load. Increased mechanical strength of micropillars with diameters below 10  $\mu\text{m}$  was detected, which suggested that the external geometry is one important parameter to characterize material strength at micrometer scale. This work inspired numerous new studies of specimen size effect with pillar compression testing [45–48]. A dislocation starvation theory was first put forward in a study by Greer et al. on  $\langle 001 \rangle$  oriented single crystalline Au pillars with diameters varying between 300 and 7450 nm under uniaxial compression tests [42]. They suggested that dislocations leave the specimen surface more rapidly than new dislocations are generated due to the small specimen sizes, which leads to a “starved” status of dislocations resulting in the requirement of high stress for dislocation nucleation. In the work of Bei et al. [49], Mo micropillars with diameter up to 1.2  $\mu\text{m}$  were

prepared from selective etching of a NiAl/Mo directionally solidified alloy, two important findings were noteworthy: First the initial dislocation density actually softens micropillars, the micropillars prestrained to 4% were on average stronger than those prestrained to 11%. However, for the micropillars under dislocation free conditions, the flow stress was found to be independent of pillar size and approached to the theoretical strength. Shan et al. [50] found a phenomenon named as “mechanical annealing”, the micropillar with a diameter below 300 nm obtained a dislocation-free status through mechanical deformation, increased stress was needed for the activation of new dislocation sources for plastic deformation, which confirmed the dislocation starvation theory.

Simultaneously, an increased influence of strain gradient is expected in the plastic deformation of miniaturized specimens, where “strain gradient plasticity model” [43, 51–55] plays a significant role for explaining the mechanical size effect. Based on this theory, the flow stress in miniaturized specimens is increased due to the so-called geometrically necessary dislocations (GNDs), which are related to the strain gradient in the deformation field. Micro-beam bending testing is therefore ideal for a more detailed study of the influence of strain gradient on the mechanical size effect. Motz et al. [56] have done the micro-sized copper bending beam testing to study the gradient dominated deformation. Micro-sized bending beams of single crystal copper with thickness from 1  $\mu\text{m}$  to 7.5  $\mu\text{m}$  were fabricated with FIB and loaded with a nano-indenter. They have found increased flow stress in the micro beams with reduced thicknesses, and they suggested that the strong size effect is due to the combination of two dislocation mechanisms: The limitation of available dislocation sources and a dislocation pile-up at the beam center. Demir et al. [57] have conducted microscale bending of copper single crystal beams with thicknesses between 0.7 and 5  $\mu\text{m}$  and carried out subsequent EBSD characterization. They have introduced a mean-field breakdown theory to explain the mechanical size effect of the copper single

crystal beams. They have suggested the mechanical size effect is exclusively due to the availability of dislocation sources and the relationship between the dislocation correlation length and the specimen size. If the specimen size is smaller than the correlation length, the potential dislocation sources are limited resulting in a strong size effect in the mean-field breakdown regime. When the specimen size exceeds the correlation length, the experiment is conducted in the mean-field domain that generation of GNDs was observed in the beams, which contribute to the flow stress. Konijnenberg et al. [58] have attempted to verify the GND density based on 3D EBSD measurements. By using the Nye's dislocation tensor [59], the experimentally determined GND density was compared to a theoretical lower bound estimation for a homogeneous bending of a cantilever, both values showed a good agreement, and the main deformation of the cantilever is also related to GNDs. In the micro-beam bending testing, the increased influence of GNDs on the mechanical size effect was determined.

Apart from the mechanical "size effect" at room temperature, a so-called "thickness debit" effect was detected in creep tests with miniaturized specimens in sub-millimeter to millimeter scale at elevated temperatures [11, 60–63], meaning that a reduction in rupture lives and fracture strain were observed with reduced specimen thickness. Srivastava et al. [64] have studied the creep behavior of PWA1484 Ni-based single crystal superalloy sheet specimens of thickness 3.18 mm and 0.51 mm at two test conditions: low-temperature, high-stress condition and high-temperature, low-stress condition. They have concluded that at low-temperature, high-stress condition, reduced creep strain and the time to rupture were observed with decreasing specimen thickness. For specimens with thickness 3.18 mm, a mixed-mode of failure involving ductile void growth and cleavage-like cracking was observed, while for specimens with thickness 0.51 mm, cleavage-like cracking was more dominant on the failure surface. At high-temperature, low-stress condition increased steady-state creep rate and a decreased time

to rupture were observed with decreasing specimen thickness, but there existed no systematic dependence of the creep strain to rupture on specimen thickness. For specimens with thickness 3.18 mm, the failure mode was void nucleation, growth and coalescence, while for specimens with thickness 0.51 mm, a mixed-mode of ductile and cleavage-like fracture was observed. The influence of oxidation on the creep behavior was investigated by Bensch et al. [65]. They found that oxidation sharply reduces the volume fraction of  $\gamma'$  precipitates in the surface-near regions of the single crystal nickel-based superalloy M247LC SX thin-walled specimens with different thickness down to 0.1 mm. The influence of oxidation on the creep behavior increases with decreasing specimen thickness. Based on this result, five single crystal nickel-based superalloys with different compositions have been cast, which represent the specimens affected by oxidation in different surface-near regions containing different  $\gamma'$ -volume fraction. Creep experiments were carried out on these alloys. For specimens with reduced  $\gamma'$ -volume fraction, increased minimum creep rates and Norton exponent  $n$  were observed due to the change in mechanism from dislocation climb and cutting to the by-pass mechanism. For a reduced influence of oxidation, the miniaturized specimen can be aluminized [66–68] for a protective alumina scale for less scatter in creep behavior and better creep resistance than non-coated specimens. Still, there may exist a stress uncertainty with the aluminized specimens in these works, since the stress was determined by the cross-section of the specimens in the non-coating area without considering the influence of the coating layer. Mälzer et al. [69] have tested single crystalline superalloy LEK94 miniaturized specimens with a cross-section of  $2 \times 3 \text{ mm}^2$  and a gauge length of 9 mm in tensile creep testing. They reported that the creep behavior of these miniaturized specimens showed a good agreement with the conventional specimens. They also found that the aligned cast micropores in the miniaturized specimens can significantly affect the onset of tertiary creep and rupture strains. Miniaturized specimens with pre-existing cast micropores perpendicular to the load direction showed

an earlier onset of a rapid tertiary creep and smaller rupture strains. Peter et al. [70] have modified the testing machine of Mälzer, they have developed an inert gas system to perform creep tests at temperatures up to 1150 °C to keep high-temperature oxidation at a minimum. With this new method, they found that the surface variation of the miniaturized specimens such as creep cavity formation in Cu and localized deformation events in Cu can be directly studied without the influence of oxidation.

Based on these recent works on small scale testing at room temperature and creep tests at elevated temperatures, the suitable size for specimen thickness and width in this study is determined in sub-millimeter scale, i.e., hundreds of micrometer. It is scientifically interesting to study the creep behavior of miniaturized specimens in this scale under the potential influence of mechanical “size effect” or “thickness debit effect”.

The **second aspect** is the loading method in creep tests, the miniaturized specimens can be either loaded in compression or tension in creep tests. In this study, we have decided to choose the tensile creep method since there exist several severe drawbacks of compression test with miniaturized specimens. For example, in the work of Kiener et al. [71] and Shade [72] et al. the lateral constraint showed an apparent effect on the flow stress and strain hardening effect in the micropillars, suggesting the degree of lateral constraint is one crucial influencing factor in the pillar compression testing. Frick et al. [74] had reported that a dramatic increase in strain hardening was observed with decreasing pillar diameter. Dislocation pile-up at the pillar bottom suggested that the strain hardening is also influenced by the specimen’s geometry and the direction of slip systems based on the crystal orientation. Compared to micro-compression testing, tension experiments offer several benefits such as no limitation to high aspect ratios of the specimens, no influence of constraints arising from the friction or further uncertainties caused by the alignment between the indenter and specimen [75]. However, there are no standards yet evolved for micro-tensile testing res-

ulting in difficulty in the comparison of experimental results [76–78]. The mechanical behavior of the miniaturized specimens shows a dependence on the specimen geometry, which is the **third aspect** for the specimen miniaturization. For example, Kiener et al. [44] have developed a method for in situ testing of copper single crystals miniaturized tension specimens with diameters ranging from 0.5  $\mu\text{m}$  to 8  $\mu\text{m}$  and aspect ratios between 13.5:1 and 1:1. Both groups of miniaturized specimens showed a size dependence of the flow stress: For high aspect ratios, strain hardening was negligible in the miniaturized specimens, meanwhile, for specimens with low aspect ratios, a pronounced strain hardening was observed as a result of dislocation pile-ups at the shoulder of tension specimens. Kirchlechner et al. [79] provided an in situ  $\mu$ -Laue tensile study to obtain the evolution of type and density of stored dislocations in the micro-sized single crystalline specimens with diameters from 3  $\mu\text{m}$  to 6  $\mu\text{m}$  and an aspect ratio of 5:1. Glide on the slip system with the highest Schmid factor without any storage of GNDs was observed in the gauge length area, and the storage of GNDs was detected at the region adjacent to the specimen head and base. Sergueeva et al. [80] have tested dog-bone tensile specimens with a gauge width of 1 mm and gauge lengths from 2 mm to 40 mm. They found the results of the tensile testing were dependent on the specimen size and geometry that a significant drop in uniform elongation was observed for miniaturized specimens with increasing gauge length to width ratio, but the miniaturized specimens did not reveal any noticeable effect of the gauge length on strength characteristics. Zhao et al. [18] have reported that the strain measurement based on the crosshead displacement may contain serious errors depending on the specimen geometry and size at sub-millimeter scale, both the uniform elongation and the post-necking elongation increase with decreased gauge length and increased specimen thickness resulting varied tensile ductilities. Yuan et al. [81] also observed the same behavior in their work with the miniaturized specimens even in millimeter scale. All these works suggested that the geometry of the miniaturized specimens plays a significant role in mechanical proper-



ties in scale from micrometer to millimeter. For a better understanding of the influence of specimen geometry on creep behavior, it is necessary to design miniaturized specimens with different length-to-width ratios ( $L/W$ ) for micro-tensile creep tests. Simultaneously, the miniaturized tensile specimens should have identical thicknesses and widths to obtain a rectangular cross-section so that the miniaturized specimens contain similar geometry as the conventional specimens.

### 1.2.3 Material selection

Two materials were chosen to research the influence of specimen miniaturization on the creep behavior.

In the **first step**, the solid solution strengthened 80/20 nickel-chromium alloy Nimonic 75 polycrystal was tested as reference material. The Nimonic 75 alloy is used for sheet-metal fabrications in gas-turbine engines due to its excellent mechanical properties and oxidation resistance at high temperatures. The test results of the Nimonic 75 miniaturized specimens will be compared with conventional specimens [82, 83] (diameter 6 mm, gauge length 30 mm) at identical experimental conditions, for which experimental data are readily available. With the obtained data, the accuracy and stability of the customized micro-tensile creeping setup can be verified. Simultaneously, the influence of specimen miniaturization on the creep behavior of the Nimonic 75 polycrystal can also be studied.

In a **second step**, stoichiometric NiAl single crystalline miniaturized specimens were tested. While the first step was mainly aimed at a successful verification of the customized test setup and a comparison of miniaturized specimens with results for conventional creep tests, the second step was driven by the scientific interest in the material characterization of the single crystalline NiAl alloy. The intermetallic alloy NiAl provides excellent oxidation resistance, reduced density and very high thermal conductivity compared to other Nickel-based superalloys [84–86], which makes NiAl alloy a

promising candidate for the next generation of high-temperature materials. However, the low creep strength limited the application of NiAl at elevated temperatures, such as in gas turbine engines. Strengthening with oxide dispersion [87] or directional solidification technique to process NiAl-based composites [88–90] were provided to be promising methods to improve the creep resistance by numerous studies. Before starting micro-tensile creep tests with these enhanced materials, it is necessary to systemically study the influence of specimen miniaturization on the creep behavior of NiAl single crystals by comparing with the conventional specimens at identical experimental conditions [91–93]. Because NiAl single crystals are considered as matrix materials in the enhanced materials, the understanding of the creep behavior of NiAl single crystalline miniaturized specimens is therefore the basis for subsequent research of the enhanced materials. Additionally, the creep behavior of NiAl single crystals shows a strong dependence on the crystal orientations: the [110] soft orientation, where the creep deformation is dominated by the glide of  $\langle 100 \rangle$  dislocations [94–97], and [100] hard orientation, where no driving force exists for the  $\langle 100 \rangle$  dislocation glide, the creep deformation is mainly controlled by the  $\langle 110 \rangle$  dislocation glides via dislocation climb [93, 98–100]. Hence it is also scientifically interesting to study the influence of crystal orientations on the creep behavior of miniaturized specimens.

### 1.3 Thesis overview

The main aim of this thesis is to study the influence of specimen miniaturization on creep behavior in sub-mm scale up to temperature 1000 °C. The thesis is structured as follows:

In Section 2, the design of miniaturized specimens and the development of a customized setup for micro-tensile creep tests are introduced. The accuracy and stability of temperature and load control of the customized setup are

analyzed. Digital Image Correlation (DIC) is used for a contactless strain measurement. The basic principles of the DIC method are introduced, then factors affecting the accuracy of strain measurement with the DIC method will be analyzed in detail. A constant stress test method based on the closed-loop feedback from the load and strain signals is developed.

In Section 3, Nimonic 75 polycrystalline miniaturized specimens were tested as reference material for the calibration of the customized setup by comparing with the test results of conventional specimens [82, 101] at identical experimental conditions. Analyses of fracture mechanism, the influence of oxidation and strain distribution on the miniaturized specimen surface were carried out to study the creep behavior of the Nimonic 75 polycrystalline miniaturized specimens.

In Section 4, NiAl single crystalline miniaturized specimens were first tested with different specimen sizes and length-to-width ratios in [110] soft orientation. Test results were compared to the conventional specimens in the same experimental conditions [91–93]. Analysis of fracture mechanism, strain distribution, oxidation effect and geometrically necessary dislocations (GNDs) of the miniaturized specimens were carried out step by step to confirm the main influencing factors that are responsible for the creep behavior of the miniaturized specimens. Additionally, the creep behavior of the miniaturized specimens tested in [100] hard orientation was analyzed with the identical methods to study the influence of crystal orientations on the creep behavior of the miniaturized specimens.

In the final section, the scientific key findings of small scale creep testing are summarized. Finally, the outlook of improvement possibilities for micro-tensile creep testing is discussed.



## 2 Development of high temperature tensile creep setup

### 2.1 Design of miniaturized specimens

The design guidelines of miniaturized specimens in micro-tensile creep testing are: A similar geometric shape of the miniaturized specimens to conventional specimens is needed for the comparison of creep behavior; The cross-section area can be precisely and easily measured for stress calculation; Different length-to-width ( $L/W$ ) ratios of the miniaturized specimens are necessary to study the influence of specimen geometry on creep behavior. Therefore, we have designed the dog-bone shaped specimens with a rectangular cross-section in three different sizes for the micro-tensile creep tests. Figure 2.1 details the design of the miniaturized specimens, and the unit is in millimeter.

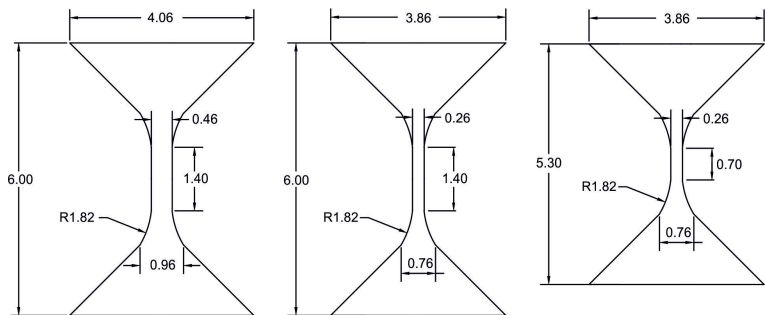


Figure 2.1: An illustration of the design drawing of the dog-bone shaped miniaturized specimens with a rectangular cross-section in three specimens sizes

The specimens from the two materials (Nimonic 75, single crystal NiAl) were cut by using Electrical Discharge Machining (EDM). The processing error of the EDM machine concerning dimensional accuracy is  $0.25\ \mu\text{m}$ . After the EDM processing, a recast layer on the specimens was observed with a thickness from 1 to  $5\ \mu\text{m}$ . To remove the recast layer and reduce the surface roughness, the miniaturized specimens were mechanically polished with 4000 grit sandpaper and afterward electropolished for further optimization of the surface roughness. Unfortunately, the surface quality after electropolishing is not ideally optimized in both materials. Uneven surfaces were observed after electropolishing in both materials due to an inhomogeneous voltage distribution on the specimen surface since the specimen size is too small for a conventional electropolishing machine. For Nimonic 75 polycrystalline specimens, electropolishing causes material elimination in the grain boundaries on the specimen surface resulting in potential stress localization in tensile creep tests. For NiAl single crystalline specimens, even though no grain boundaries exist in this material, the rectangular cross-section was rounded after electropolishing, which increases the uncertainty of stress calculation. Therefore all the miniaturized specimens tested in this study were mechanically polished with 4000 grit sandpaper to a surface roughness below  $\pm 1\ \mu\text{m}$ . The polished specimens were abbreviated for a convenient identification in this study. (see Table 2.1)

Table 2.1: Abbreviation of the miniaturized specimens

<b>miniaturized specimen types</b>	<b>abbreviation</b>
$400 \times 400 \times 1400\ \mu\text{m}^3$	<i>L400</i>
$200 \times 200 \times 1400\ \mu\text{m}^3$	<i>L200</i>
$200 \times 200 \times 700\ \mu\text{m}^3$	<i>S200</i>



## 2.3 Design of customized tensile creep setup

The custom-built setup, as shown in Figure 2.3, has been originally designed by Leisen et al. [17] for SiC thin-film high-temperature characterization and was adopted in the present thesis for high-temperature micro-tensile creep tests. The essential components of the setup are a vertical split hinged furnace for the specimen heating, a load cell combined with an actuator for load control, and a camera providing the DIC data for strain measurements. The specimen is fixed in a vertical arrangement with two adapters and is placed in the center of the furnace. The temperature is measured with a thermocouple (type S) next to the specimen but without direct contact. The furnace can be flooded by an inert gas such as Ar to prevent oxidation.

### 2.3.1 Heating method

A resistance heating via a spiral-shaped Kanthal A1 wire (Sandvik AB, Hallstahammar, Sweden) with a thermocouple was used for temperature control. The thermocouple is set through the furnace door with its top point located next to the miniaturized specimen but without direct contact (see Figure 2.3). The specimen is positioned in the center of the furnace at an equal distance to the heating wire. A self-developed temperature control coded by LabVIEW based on electric heating control was used. The heating system allows fast heating rates up to 30 K/s with a temperature control stability of  $\pm 0.1$  °C. Uniform temperature distribution in the furnace was confirmed by using measurements from three thermocouples at equal distance (5 mm) along the specimen. The maximum temperature difference between the upper/lower thermocouples and the central one is  $\pm 2$  °C at 1000 °C. The temperature accuracy along the gauge length of the specimens is, therefore, expected to be better than  $\pm 1$  °C.



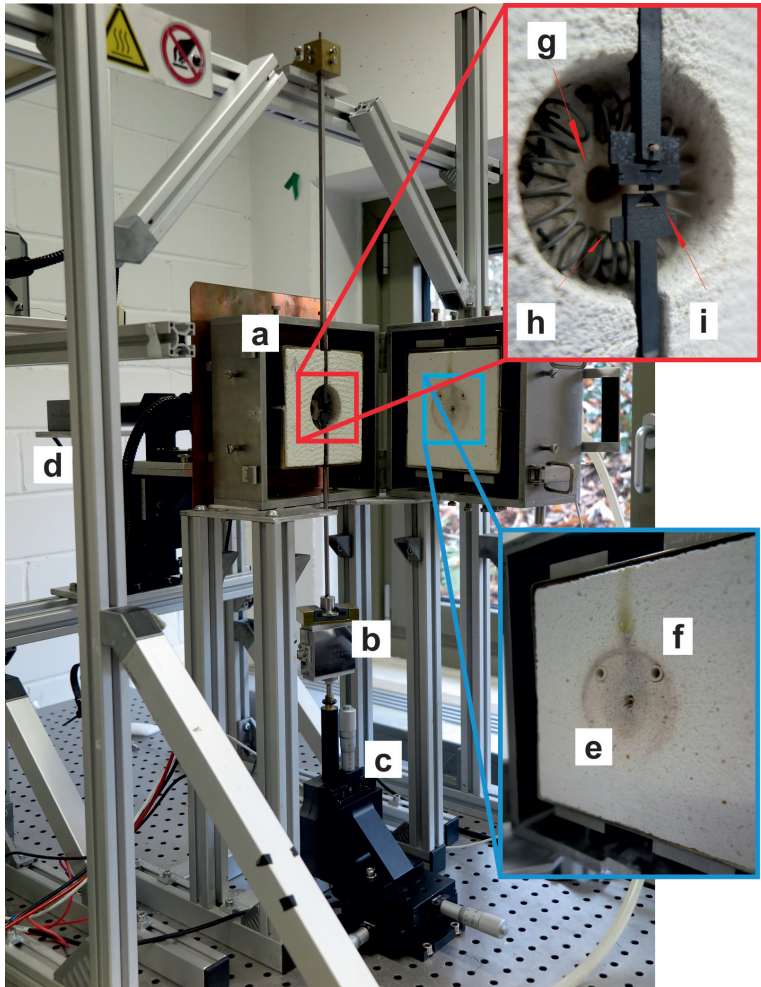


Figure 2.3: Micro-tensile creep setup. (a) furnace, (b) load cell, (c) actuator, (d) camera for DIC analysis, (e) thermocouple through furnace door, (f) port for inert gas, (g) view port, (h) heating wire and (i) the assembled specimen and adapter

### 2.3.2 Load and displacement control

A 10 N load cell (FN 3148- A1-10 N from disynet, Brüggem-Bracht, Germany) and a DC actuator (M-230.25 from Physik Instrumente PI, Karlsruhe, Germany) are combined for the load control in the micro-tensile creep tests. The actuator has a 25 mm working distance and a minimum increment of 0.1  $\mu\text{m}$ . For a specimen with a gauge length of 1.4 mm, a minimum strain increment of  $7 \times 10^{-5}$  based on the minimum increment of the actuator was enabled. The design resolution of the actuator is better than 5 nm, and the displacement measured by the actuator is the sum of the specimen elongation and the elastic deformation of the upper and lower rod in the micro-tensile creep tests. Therefore the actual displacement resolution of the miniaturized specimens is at nm level, and the minimum strain increment may be even smaller. The accuracy of the load cell as specified by the manufacturer is 10 mN. Fluctuations in the load signal during high-temperature creep tests can be caused by the thermal expansion, creep deformation of the loading rods as well as the heating instability from the furnace. The corresponding fluctuation was measured to be,  $\pm 1$  mN at room temperature and,  $\pm 3$  mN at 1000 °C.

### 2.3.3 Measurement uncertainty in stress

There are two error sources of the stress calculation: The measurement error of the specimen cross-section and the load fluctuation during tests. The cross-section of each specimen was measured with a Nikon Eclipse LV150N optical microscope, and the measurement error caused by the measuring uncertainty and the surface roughness is  $\pm 1$   $\mu\text{m}$ . The load fluctuation has a maximum amplitude of 3 mN. Hence, the corresponding error  $\Delta\sigma$  in the stress  $\sigma = \frac{F}{w \cdot t}$  from a Gaussian error analysis can be expressed by:

$$\Delta\sigma = \sqrt{\left(\frac{\Delta F}{w \cdot t}\right)^2 + \left(\frac{F \cdot \Delta t}{w \cdot t^2}\right)^2 + \left(\frac{F \cdot \Delta w}{w^2 \cdot t}\right)^2} \quad (2.1)$$

Here  $F$  is load,  $w$  and  $t$  are the specimen width and thickness,  $\Delta w$  and  $\Delta t$  are the dimensional measurement errors ( $\pm 1 \mu\text{m}$ ), and  $\Delta F$  is the sum of the maximum fluctuation of the load amplitude (3 mN) plus the maximum accuracy of the load cell (10 mN) so that  $\Delta F = \pm 13 \text{ mN}$ . The nominal cross-sections of the miniaturized specimens are  $200 \times 200 \mu\text{m}^2$  and  $400 \times 400 \mu\text{m}^2$ . At a stress level 10 MPa, the corresponding load is 0.4 N and 1.6 N, which leads to the relative stress error  $\Delta\sigma/\sigma$  3.33% and 0.8%. The stress error reduces with increasing stress, for initial stress larger than 75 MPa, the relative error is below 0.8% for the L200 specimens. Therefore, the stress error of the customized setup is at an acceptable level.

### 2.3.4 Influence of oxidation

It is also recommended to test the miniaturized specimens in vacuum or inert gas conditions to prevent the influence of oxidation on the creep behavior. Peter et al. [70] have developed a customized setup for creep tests with miniaturized specimens in millimeter scale under an inert gas atmosphere at temperatures up to 1150 °C, their experimental method allows to keep high-temperature oxidation at a minimum. Based on this idea, we use two ports through the furnace door to input the inert Ar gas (see Figure 2.3). One miniaturized specimen was tested to study the oxidation influence in the inert Ar gas environment. Unfortunately, the oxide layer was still formed due to the imperfect airtightness of the furnace in our customized setup, it is also observed that the input inert gas caused temperature fluctuation in the furnace resulting in reduced specimen stability and varied air refraction. Therefore the quality of the images is no longer good enough for the DIC method, which led to reduced accuracy of the strain measurement. Based on the actual experimental conditions in our case, we have decided to test all the miniaturized specimens in air.

## 2.4 Strain measurement with Digital Image Correlation (DIC)

### 2.4.1 Basic principles

Digital Image Correlation is an optical method that analyzes the deformation of the specimen surface by comparing a series of images before and after deformation. In this study, a MATLAB open source code with a sub-pixel resolution is used and optimized to fulfill the requirement of micro-tensile creep tests [104]. In the routine implementation of the DIC method, a region of interest (ROI) should be first defined as evenly spaced virtual grids in a reference image, each point in the virtual grids has a subset ( $n \times n$  pixels) and a search area ( $N \times N$  pixels) (see Figure 2.4). A cross-correlation calculation is used to track the new positions of each point by finding the maximum of the correlation array between pixel intensity array subsets on the reference image and the subsequent image after deformation in the search area.

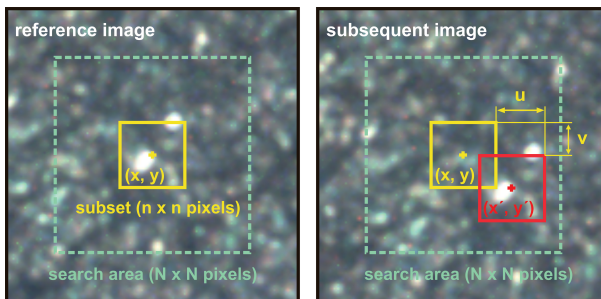


Figure 2.4: The schematic diagram for the basic principle of Digital Image Correlation: Tracking of the new point position ( $x'$ ,  $y'$ ) in the subsequent image after deformation from the initial point position ( $x$ ,  $y$ ) in the reference image, the point contains a subset ( $n \times n$  pixels) and a search area ( $N \times N$  pixels).

After determination of the new point position  $(x', y')$  in the following image of the deformed specimen, the displacement of the point in the x- and y-axis direction can be calculated as:

$$\begin{aligned} u &= x' - x \\ v &= y' - y \end{aligned} \quad (2.2)$$

Here  $u$  is the displacement of a point in the x-axis direction and  $v$  is the displacement in the y-axis direction. The corresponding strains can be calculated as:

$$\begin{aligned} \varepsilon_x &= \frac{\partial u}{\partial x} \\ \varepsilon_y &= \frac{\partial v}{\partial y} \\ \varepsilon_{xy} &= \frac{1}{2} \left( \frac{\partial u}{\partial x} + \frac{\partial v}{\partial y} \right) \end{aligned} \quad (2.3)$$

Here  $\varepsilon_x$  and  $\varepsilon_y$  are the strains in the x- and y-axis,  $\varepsilon_{xy}$  is the shear strain. Considering the fluctuation of points caused by the instability during the micro-tensile creep tests, e.g., fluctuation of load and temperature on the specimen resulting in deteriorated image quality, linear regression is used in the ROI containing multiple points for strain calculation with enhanced accuracy. Figure 2.5 shows the result of strain calculation with a Nimonic 75 specimen tested at 850°C, 80 MPa and interrupted before fracture as an example: the strain here equals the slope of the fitted displacement line. Since the displacement of points (blue points in Figure 2.5 (b)) in the miniaturized specimen is not perfectly linearly distributed due to necking or strain localization in the gauge length area, in order to correctly calculate the global strain, only points (red points) from two ends of the gauge length area were selected for linear regression. This method is similar to the common strain calculation with an extensometer. The global strain here is determined as  $\varepsilon = 0.12$ .

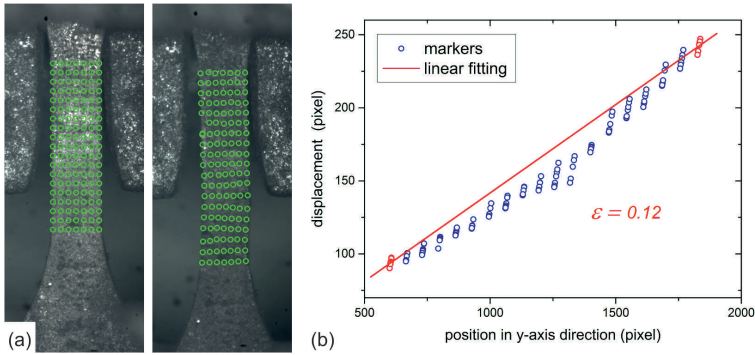


Figure 2.5: An example of strain calculation with the DIC method. (a) the positions of points as virtual grids in the reference image and the image of the deformed specimen. (b) the global strain calculation with linear regression of the red points located at both specimen ends.

Besides the global strain calculation, a strain distribution analysis on the specimen surface is possible with the DIC method (see Figure 2.6 (a)). The working principle is that the strain of each point can be calculated with at least two neighbor points in x- or y-axis direction by linear regression to obtain the strain distribution of the specimen surface. Figure 2.6 (b) shows the strain distribution of the same specimen in Figure 2.5 in the y-axis direction, where a strain localization was observed. A high degree of overlap is detected between the strain localization and the damage distribution in the polished specimen surface. The analysis of the strain distribution is only based on the specimen surface information, i.e., the status of the strain distribution inside the specimen or on the other specimen surfaces is unknown. But considering the size of the miniaturized specimens, any strain localization in the specimen will result in an apparent corresponding strain localization on the specimen surface. Additionally, with the DIC method, it is possible to study the evolution of the strain distribution and detect the influence of strain localization on the creep behavior of the miniaturized specimens.

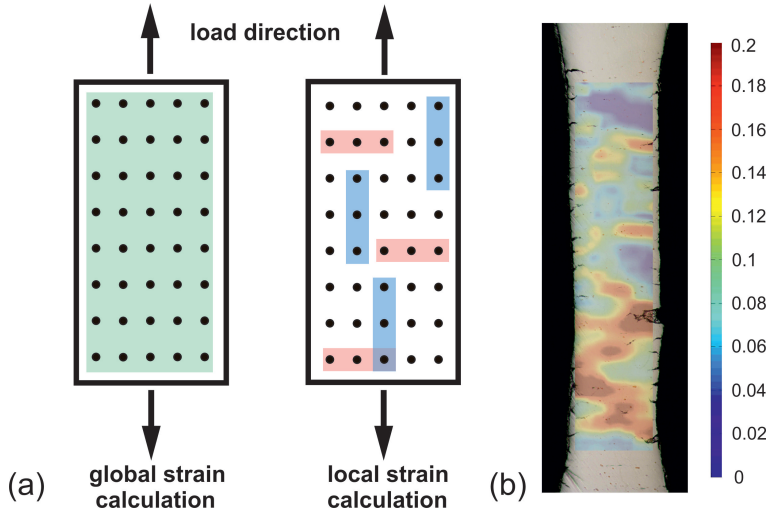


Figure 2.6: (a) Schematic diagrams of the global strain calculation, one strain data with linear regression to represent the overall elongation of the specimen in the gauge length area, and the local strain calculation, a summary of strain data from each point calculated with its neighbor points to obtain the strain distribution. (b) A high degree of overlap between the strain distribution calculated by the DIC method and the damage distribution in the polished specimen surface is detected, the Nimonic 75 specimen was tested at 850°C, 80 MPa and interrupted before fracture.

## 2.4.2 Strain rate calculation

Since creep is a time-dependent deformation under a constant applied load, the deformation rate, i.e., the creep strain rate, is an essential parameter of the material creep properties. The creep strain rate of each data point is the slope calculated with linear regression by choosing an interpolation range containing a certain number of its neighbor points in the Creep Strain vs. Time curve (see Figure 2.7). Therefore the total number of the neighbor points in the interpolation range can influence the linear fit result of the creep strain rate: an extensive range of neighbor points causes an over-smoothing of the creep strain rate and results in a loss of detail information in the Creep Strain Rate vs. Strain curve. Oppositely, too few neighbor points result in

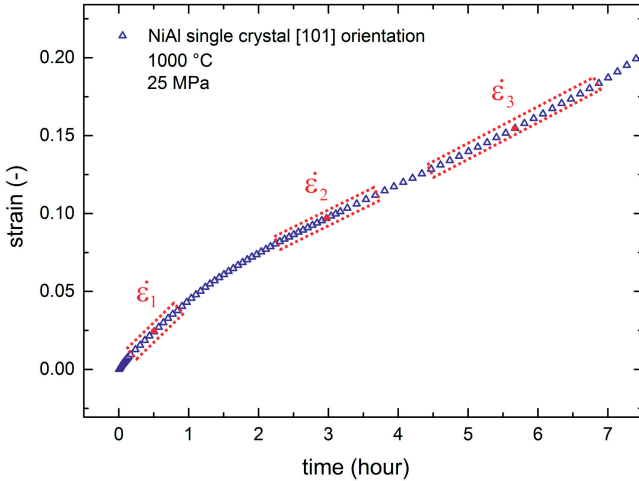


Figure 2.7: Strain rate calculation with linear regression by choosing an appropriate interpolation range of each data point.

an increased signal noise, because the fluctuation of data points have an increased influence on linear regression. Therefore an appropriate interpolation range containing suitable neighbor points for each data point is the essential requirement to obtain a reasonable creep strain rate data.

The strain data here were calculated from the images captured with different time intervals with the DIC method. The purpose is to reduce unnecessary data volume, therefore the time interval between the data points is not identical (see Figure 2.7). The interpolation range of each data point should be modified individually to obtain the best quality of the creep strain rate data. The working principle of the creep strain rate calculation here is: The slope of each data point is calculated with increasing interpolation range until a preset threshold of determination coefficient of linear regression is reached, usually  $R^2 > 0.95$  is used in this study. This slope value is defined as the most accurate creep strain rate, and no more slope calculation with a broader interpolation range will be continued at this data point to prevent



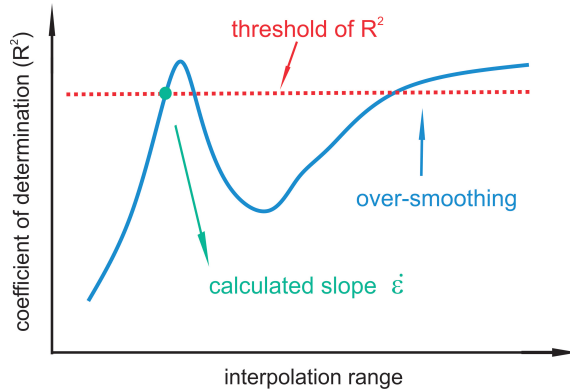


Figure 2.8: Schematic diagram of the determination of an appropriate interpolation range to prevent over smoothing

over smoothing. The schematic diagram in Figure 2.8 shows the explanation of the determination of an appropriate interpolation range for strain rate calculation.

## 2.5 DIC influencing factors

The accuracy limit of the DIC method in strain measurement is based on the quality of the obtained images in the customized micro tensile creep tests setup. Different influence factors will be discussed in the following section.

### 2.5.1 Theoretical accuracy

The theoretical accuracy of the DIC method is based on the calculation accuracy of the software program, the MATLAB code used in this study provides a maximum accuracy of 0.001 pixels. Assuming the gauge length of the miniaturized specimen occupies 1000 pixel, a corresponding strain accuracy below  $2 \times 10^{-6}$  is expected. However, the actual accuracy of the strain measurement is dependent on the experimental condition. In this study, a lens with  $4\times$  magnification was used under a light condition with

an average wavelength of 550 nm in the customized setup. According to the Abbé diffraction limit [105], the optical resolution of the optical lens with 0.1 NA (numerical aperture) here is:

$$d = \frac{\lambda}{2NA} = \frac{0.55\mu m}{2 \cdot 0.1} = 2.75\mu m \quad (2.4)$$

This means the minimum distance  $d$  required to distinguish two optical signals with enough contrast in this experimental condition is 2.75  $\mu m$  and the corresponding image size projected onto the CCD surface is the multiplication of the optical resolution (2.75  $\mu m$ ) and the lens magnification (4 $\times$ ) yielding a result of 11  $\mu m$ . With the pixel sensor size of 3.5  $\mu m$ , one recognizable optical signal unit contains more than 3 pixels. Figure 2.9 shows the schematic diagram of the signal status in this experimental condition. The blue curve represents the initial signal obtained from the specimen surface with the maximum optical resolution  $d=2.75\mu m$  and the blue rectangles

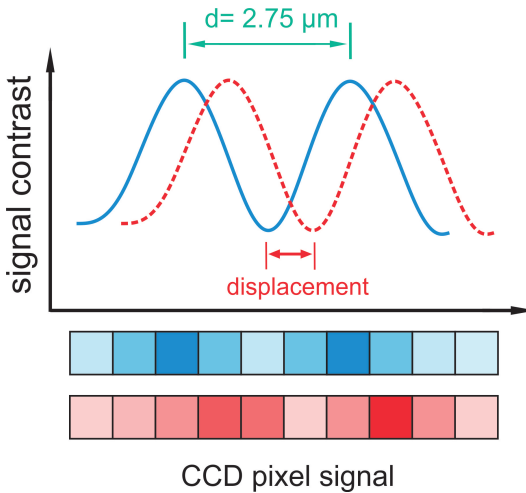


Figure 2.9: Schematic diagram of the signal status with a maximum optical resolution  $d=2.75\mu m$  in this study

are the pixel unit in the CCD camera containing the corresponding signal intensity. The red curve and rectangles are the new signal status after the specimen deformation or displacement. Even though the displacement is smaller than the maximum optical resolution, the DIC method calculates the difference between the recognizable signals before and after deformation to obtain the displacement value. Hence the accuracy of the displacement measurement is available in the sub-pixel range. To obtain a more accurate result of the displacement calculation with the DIC method, a minimum subset size containing several recognizable signals is necessary for a reliable cross-correlation calculation [106, 107]. Therefore the theoretical accuracy is dependent on both the code algorithm and the actual signal status, i.e., the experimental condition and the subset size.

### 2.5.2 Subset size influence

A set of reference images with preset displacement (<http://sem.org/dic-challenge>) was used to study the influence of subset sizes on the accuracy of the DIC method. All the ten images have random speckle patterns with a signal noise of 1.5 GL (gray level) to simulate the specimen surface in the

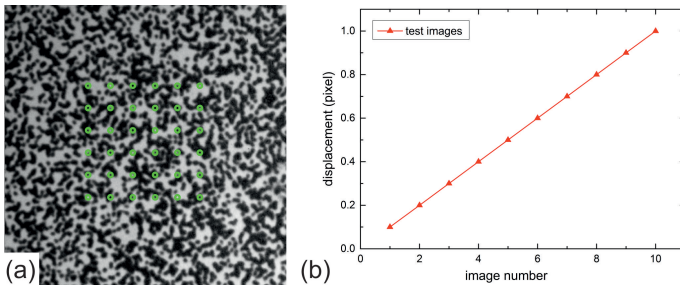


Figure 2.10: (a) One test image with random speckle patterns and virtual grids with size  $200 \times 200$  pixels and points spacing  $40 \times 40$  pixels as the region of interest. (b) the ten test images have a preset displacement of 0.1 pixels between each image in both x- and y-direction resulting in a total displacement of 1 pixel.

experimental condition, between each image a shift (displacement) of 0.1 pixels in both x- and y-direction was preset resulting in a total displacement of 1 pixel. Virtual grids with size  $200 \times 200$  pixels and points spacing  $40 \times 40$  pixels were generated as the region of interest for the analysis of the code accuracy (see Figure 2.10). Different subset sizes with  $5 \times 5$ ,  $20 \times 20$ ,  $40 \times 40$  and  $60 \times 60$  pixels were calculated to test the influence on the code accuracy and the displacement error between the preset displacement. The calculated results were plotted in Figure 2.11. Since the images have an equal displacement in both x- and y-direction and virtual square grids were used, identical results of the calculated displacement in x- and y-direction are expected so that only the displacement error in the y-direction was analyzed here. With increased subset size, the scatter level of points in each image

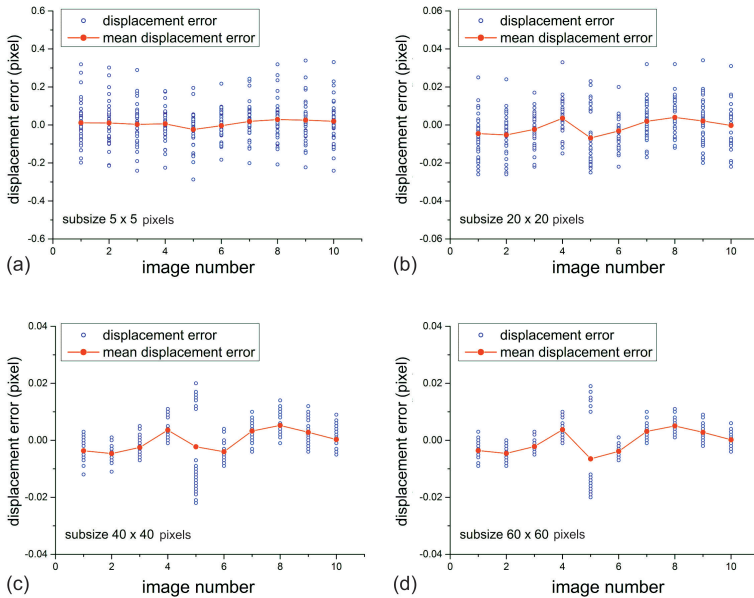


Figure 2.11: The displacement errors between the preset displacement and the calculated results with different subset sizes.

and the mean displacement error were decreased from  $\pm 0.4$  pixels in subset size  $5 \times 5$  pixels to  $\pm 0.02$  pixels in subset size  $40 \times 40$  pixels. No further improvement of the displacement error was observed with the subset size  $60 \times 60$  pixels, which shows the accuracy of the DIC method has an upper limit by increasing the subset size [106, 107]. An optimal subset size should be determined for the best accuracy and simultaneous time-saving since a bigger subset size means longer calculating time. With the subset size  $40 \times 40$  pixels here, a maximum theoretical accuracy with a displacement error below 0.02 pixels is determined, and the corresponding strain error is shown in Figure 2.12. Since the images contain only displacement change

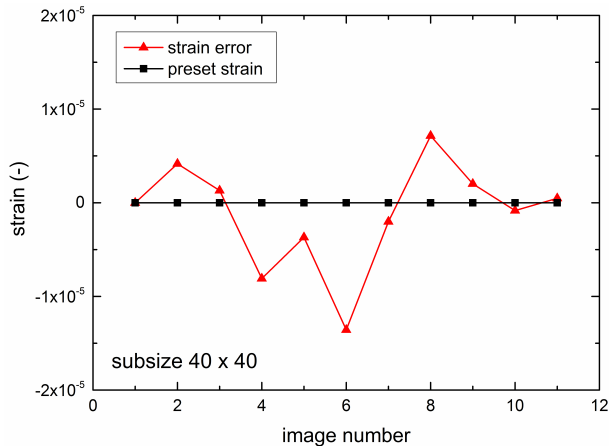


Figure 2.12: Strain calculation from the virtual grids with subset size  $40 \times 40$  in comparison with the preset strain. The strain error is below  $2 \times 10^{-5}$ .

in x- and y-direction, i.e., no strain exists. Therefore the strain error here is caused by the accuracy limitation of the DIC method. In summary, the minimum theoretical displacement accuracy based on the DIC code in this study here is determined below 0.02 pixels, and the corresponding strain accuracy is below  $2 \times 10^{-5}$  with a virtual grid  $200 \times 200$  pixels as gauge length. In

the next section, the actual strain measurement accuracy of the DIC method will be analyzed from a micro-tensile test at room temperature.

### 2.5.3 Room temperature test

The stability of the strain measurement with the DIC method in the actual experimental condition suffers more influencing factors, such as the out of plane shift and the rotation of the specimen during tests [108], the temperature and load fluctuation and the change of specimen surface contrast due to oxidation and damage [26–28]. All these influence factors result in an increased noise signal in the strain measurement with the DIC method.

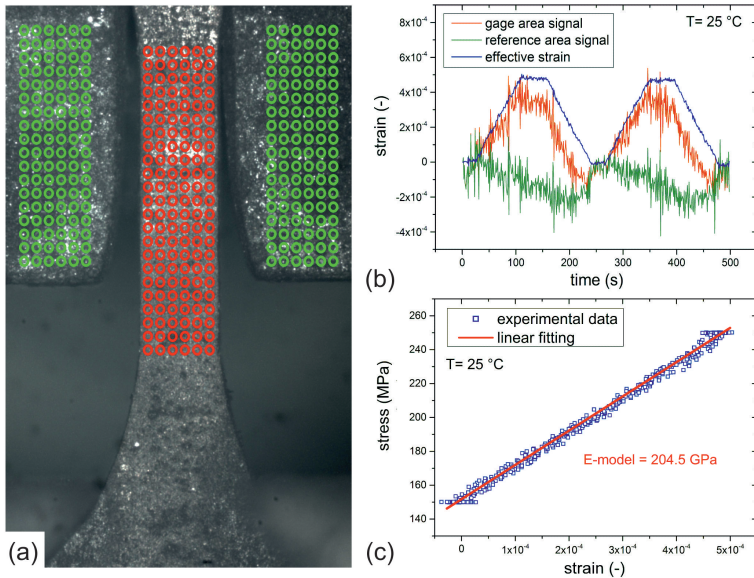


Figure 2.13: Confirmation of the strain measurement accuracy of the DIC method by tensile testing at room temperature. (a) the application of the reference area (green dots) on the unstrained adapter surface and the gauge area (red dots) in the gauge length of the specimen, (b) effective strain curve calculated from these two signals, (c) determination of Young's modulus with linear regression

Two signal sources from the gauge length area of the specimen and the adapter are used to calculate a differential value as the effective strain of the specimen [17] to reduce the noise influence. The working principle is shown in Figure 2.13 (a). The area with green dots represents the reference area, an unstrained adapter surface containing no deformation during the tests. The area with red dots is the strained area in the gauge length of the specimen. These two areas stay in the same translational plane resulting in the same strain errors in the tests. To verify the accuracy limit of the customized setup at room temperature, a tensile test of a miniaturized specimen with V4-steel was carried out. The specimen was loaded and unloaded two times in the elastic range to check the stability and accuracy of the setup, and the test result is shown in Figure 2.13 (b,c). The red curve in Figure 2.13 (b) is the strain measured in the gauge length area containing the effective strain in the specimen and the noise signal. The green curve shows the strain signal in the undeformed reference area, which is a pure noise signal due to the fluctuation of the specimen. The blue curve is the effective strain and can be calculated as:

$$\epsilon_{effective} = \epsilon_{gauge} - \epsilon_{reference} \quad (2.5)$$

The effective strain signal in the blue curve shows excellent stability with a strain error below  $5 \times 10^{-5}$ . After two times of load and unload process in the elastic range, the effective strain located at the same start point, which shows a reliable reproducibility of the customized setup. In Figure 2.13(c), the effective strain was plotted with the corresponding stress signal to calculate the Young's modulus of the specimen, the result here is 204.5 GPa, compared to the literature data 206.5 GPa [109], this customized setup shows a remarkable accuracy and stability in a micro-tensile test at room temperature.

### 2.5.4 High temperature test at 1000 °C

In the micro-tensile creep tests, the accuracy and the stability of effective strain signal decrease because that the temperature fluctuation increases due to the unavoidable hot airflow disturbance in the heating furnace, which influences the air refraction between the specimen and the camera. Hence the accuracy and stability of the strain measurement are influenced due to the deteriorated image quality. For a stable experimental condition, the miniaturized specimen should be kept in the furnace at least one hour after the assigned temperature is reached before the test starts, the purpose is to maintain a relatively stable heating condition in the furnace and provide enough time for specimen surface to form a stable oxide layer. Also, more frames can be averaged for each image taken from the camera to suppress the noise signal caused by the sudden fluctuation of the miniaturized specimen. Still, the accuracy of the strain measurement deteriorates in longtime creep tests due to the significant variation of the characteristic speckle patterns on the specimen surface in the subsequent images compared to the initial reference image, which leads to reduced accuracy of the cross-correlation calculation. Figure 2.14 shows the deteriorated accuracy of the DIC method in one NiAl single crystalline miniaturized specimen tested at 1000°C and 20 MPa. Figure 2.14 (a) shows the images of the specimen at the beginning of the experiment and just before fracture. Obvious surface deformation and damage, which are caused by necking, crack generation and continuous oxidation effect, can be observed resulting in the variation of image contrast and the feature of speckle pattern of each point in the virtual grids, which reduce the accuracy of the cross-correlation. Therefore a new reference image is needed to maintain the stability and accuracy of the DIC method in longtime tests. A filter function is used here to supervise the quality of the cross-correlation calculation between the latest images and the initial reference image [104]. The working principle of the filter function is that the relative points displacement between each point and their 10 neighbor points is



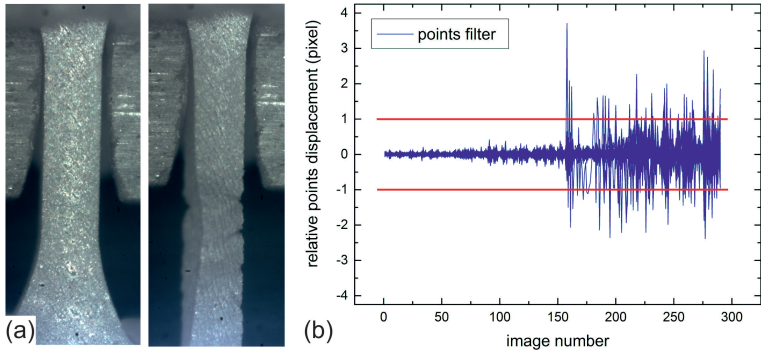


Figure 2.14: (a) Evident specimen deformation after a longtime creep test resulting in (b) reduced accuracy with the DIC method, increased relative points displacement starting from the 150th image was observed, which exceeds the filter range.

calculated and plotted versus image number. If a sudden change of one data point takes place, a spike can be detected in the relative points displacement suggesting that the cross-correlation quality of this point calculated between the latest image and the initial reference image is not good enough to maintain the accurate strain measurement of the DIC method. Figure 2.14 (b) shows the result of the filter function in a longtime creep test. After the 150th image, the relative points displacement increased significantly indicating the requirement of a new reference image. Additionally, points with apparent noise can also be deleted with the filter function to improve the accuracy of the strain calculation with the linear regression method.

With the update of the reference image, this customized setup of micro-tensile creep tests showed enough stability and accuracy of strain measurement with the DIC method at a temperature up to 1000 °C. Figure 2.15 shows the creep curves of the NiAl single crystalline miniaturized specimen tested at 1000 °C and 20MPa. Figure 2.15 (b) displays a magnified view of the beginning area of the creep curve, the noise level in the strain signal was significantly reduced with the application of the effective strain and the

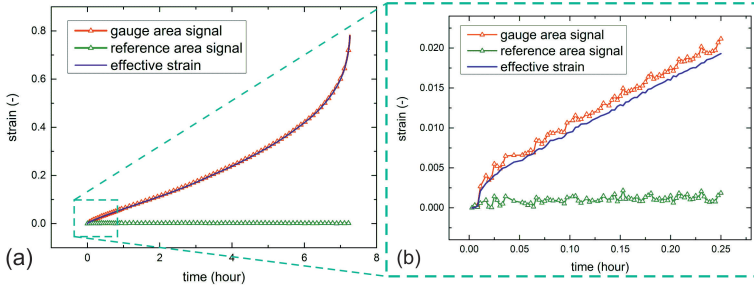


Figure 2.15: (a) Creep curve of one NiAl single crystalline miniaturized specimen tested at 1000 °C and 20MPa, (b) the magnified area at the beginning of the creep curve, a strain accuracy around  $10^{-4}$  is determined

filter function. A strain accuracy of  $10^{-4}$  is available with this customized setup at temperature up to 1000 °C.

## 2.5.5 Update of reference images in longtime tests

As discussed in the last section, the update of reference images is required in longtime tests if the quality of cross-correlation calculation between the latest image and the initial reference image is deteriorated. For example, the image  $n$  shows insufficient quality to the reference image, so that the image  $(n - 1)$  will be set as the new reference image. The point positions in the new reference image  $(n - 1)$  are now the initial positions for the subsequent images and the total global strain of the miniaturized specimen can be calculated as:

$$\begin{aligned}
 L' &= L_0 \cdot (1 + \varepsilon_{all}) \\
 L' &= L_0 \cdot (1 + \varepsilon_1) \cdot (1 + \varepsilon_2) \\
 \varepsilon_{all} &= \varepsilon_1 + \varepsilon_2 + \varepsilon_1 \cdot \varepsilon_2
 \end{aligned} \tag{2.6}$$

Here  $L_0$  is the initial gauge length of the miniaturized specimen and  $L'$  is the actual gauge length,  $\varepsilon_1$  is the strain calculated until image  $(n - 1)$  with the initial reference image,  $\varepsilon_2$  is the strain calculated from the subsequent

images based on the new reference image ( $n - 1$ ), therefore the total global strain is the addition of the two strain values. With this method, the global strain of the miniaturized specimen in the region of interest can be calculated continuously by updating new reference images to maintain the accuracy of the strain measurement. However, artificial errors are unavoidable in the strain distribution calculation with this method by simply updating a new reference image. A schematic diagram is shown in Figure 2.16 to explain this problem: The black dots represent an arbitrary point position obtained

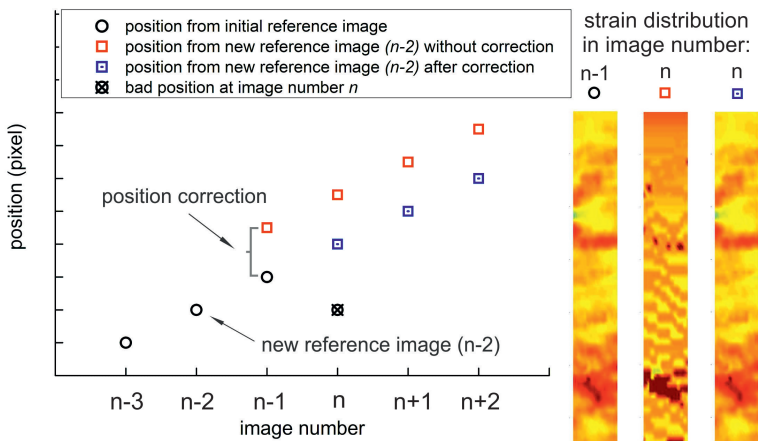


Figure 2.16: Artificial error caused by updating a new reference image and the corresponding correction method

by the correlation calculation between the initial reference image and the subsequent images. The black dots with a cross represents the inaccurate point position due to the deteriorated image quality for cross-correlation calculation. A new reference image, here image  $n - 2$ , is set for the subsequent strain distribution calculation. The new point positions based on the new reference image ( $n - 2$ ) are plotted as red dots, a difference of the positions in image ( $n - 1$ ) can be observed. The reason for this difference is that the points in the new reference image have a different characteristic

pattern in their subsets compared to the initial reference image so that an unavoidable position difference in sub-pixel level appears and can result in an unignorable artificial error in the calculation of the strain distribution. To minimize this artificial error, a position correction is calculated from the point positions in image  $(n - 1)$  between the black and red dots, thus the following points beginning at image  $n$  based on the new reference image  $(n - 2)$  will all be corrected and plotted in Figure 2.16 as blue dots. The strain distribution plot after the correction contains a better smoothness and continuity in the diagram; no obvious artificial error is detected.

It is noteworthy that the strain distribution calculation in this study is not a perfect quantitative result, because the strain data in each point is usually calculated with two neighbor points, increased influence of signal noise is expected compared to the global strain calculation, as well as the update of reference images is unavoidable due to the deterioration of the cross-correlation calculation in longtime tests. Both factors limit an accurate quantitative result of the strain distribution. Despite this weak point, the analysis of the strain distribution on the gauge length of the miniaturized specimen can still provide much useful information, such as the analysis of the strain distribution evolution with increasing time or the global strain so that an early strain localization can be detected.

## 2.6 Constant stress test

During tensile creep tests, the load or stress control on the specimen is based on the cooperation of the load cell and the actuator by using a close loop feedback to maintain the load on the specimen constant. In high-temperature creep tests, not only the miniaturized specimen, the upper and lower rod have also creep deformation, both lead to the load drop and fluctuation. A LabVIEW program is used to maintain a constant load control:

$$V_{corr} = \left( \frac{F_{measure} - F_{set}}{F_{set}} \right) \cdot K \cdot V_{min} \quad (2.7)$$

Here,  $F_{set}$  is the set load on the specimen,  $F_{measure}$  is the actual load measured by the load cell,  $V_{min}$  is the minimum movement velocity of the actuator and  $K$  is an adjustment parameter depending on  $F_{set}$ . The load error between  $F_{set}$  and  $F_{measure}$  is calculated at a time interval of 0.1 s in tests, if the load error is larger than a preset threshold value (see Figure 2.17), the actuator will move with  $V_{corr}$  until the load error becomes smaller than the threshold value. The movement velocity of the actuator  $V_{corr}$  has a linear relationship with the magnitude of the load error in this formula indicating that the load control is more stable with a smaller load error and also has a fast response by a sudden load drop in the micro-tensile creep tests.

In combination with the strain measured with the DIC method, a constant stress tensile creep test is available. The working principle is that the specimen volume is considered as constant ( $V = V_0$ ) before the tertiary creep stage so that the actual cross-section  $S'$  can be calculated according to :

$$S' = \frac{V}{L_0 \cdot (1 + \epsilon)} = S_0 \cdot \frac{1}{1 + \epsilon} \quad (2.8)$$

Therefore the actual cross-section  $S'$  is dependent on the global strain of the specimen. For constant stress, the load on the specimen is corrected as:

$$F_{set} = \frac{F_0}{1 + \epsilon} \quad (2.9)$$

So that a corrected set load  $F_{set}$  can be obtained for constant stress in micro-tensile creep tests. The frequency of the load correction is based on the strain calculation time of the DIC method, a minimum time interval of 10 seconds is available for a load correction in this study. Figure 2.17 shows the flow

diagram of the constant stress micro-tensile creep test with the customized setup.

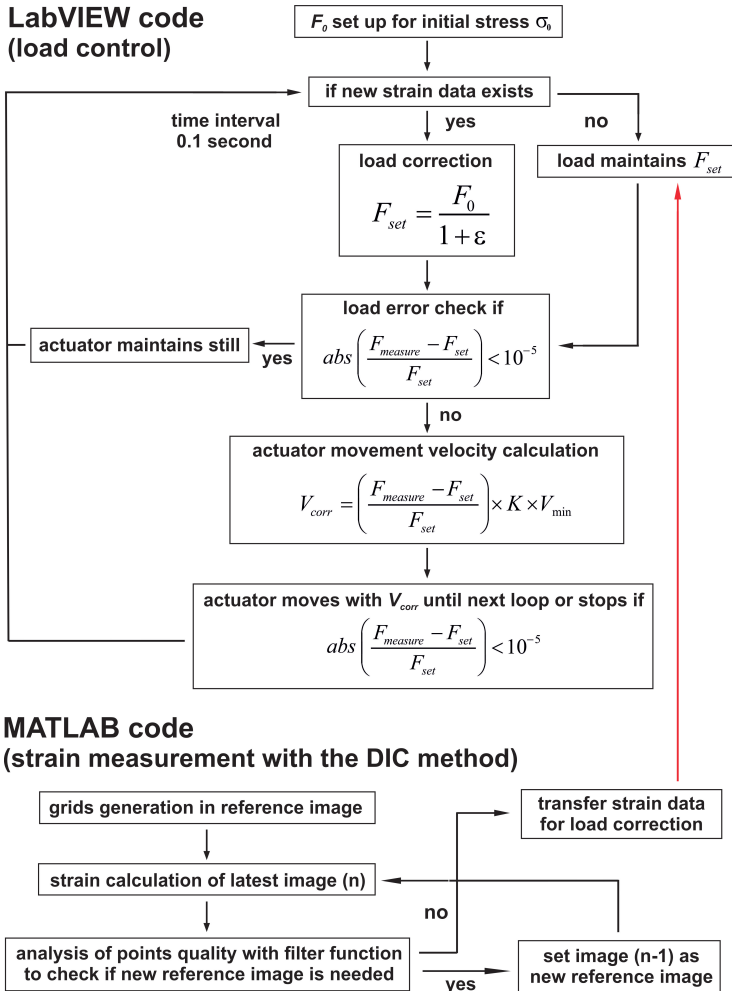


Figure 2.17: The flow diagram for constant stress tensile creep test with the customized setup

## 3 Tensile creep testing of Nimonic 75 polycrystal

Nimonic 75 is a solid solution strengthened 80/20 nickel-chromium alloy with controlled addition of titanium and carbon, which is used for sheet-metal applications in gas-turbine engines due to excellent mechanical properties and oxidation resistance at high temperatures [110]. The miniaturized Nimonic 75 polycrystalline specimens were tested for two purposes: First, they were tested as reference material to verify the accuracy of the customized setup for micro-tensile creep testing. The test results of the miniaturized specimens were then compared with the conventional specimens (diameter 6 mm, gauge length 30 mm) [82, 83] at the same experimental conditions. Second, the creep behaviors between miniaturized specimens and conventional specimens were compared to study the influence of specimen miniaturization on creep behavior for polycrystalline material.

### 3.1 Specimen preparation

Two groups of Nimonic 75 specimens were tested: the L400 ( $400 \times 400 \times 1400 \mu\text{m}^3$ ) and L200 ( $200 \times 200 \times 1400 \mu\text{m}^3$ ) specimens (see Table 2.1 in Section 2.1). The miniaturized specimens were cut by using electrical discharge machining (EDM) longitudinally from a Nimonic 75 cylinder with a 15 mm diameter. All the specimens were then mechanically polished with 4000 grit sandpaper to remove the recast layer from the EDM processing. The thickness and the width of each specimen were individually measured with an optical microscope (Nikon Eclipse LV150N, Nikon GmBH, Düsseldorf,

Germany) for accurate stress calculation. The polished miniaturized specimens have a surface roughness of  $\pm 1 \mu\text{m}$ . An average grain size of 70...110  $\mu\text{m}$  was detected. The miniaturized specimens were tested at temperatures of 850 °C and 1000 °C under a constant load or constant stress from 20 to 120 MPa and the results were compared with the conventional specimens. The performance of the customized setup and the creep behavior of the miniaturized specimens were discussed.

## 3.2 Experimental results

The creep results of the L200 and L400 specimens tested at 850 °C and 80 MPa under constant load and constant stress are plotted in Figure 3.1 as a strain rate vs. strain diagram, together with one creep curve of the conventional specimen for comparison. All the specimens were tested until fracture.

Compared to the conventional specimen, all the miniaturized specimens showed reduced fracture strain. The L400 specimens showed a minimum creep strain rate of  $1.55 \times 10^{-5} \text{ s}^{-1}$  under constant load and  $2.66 \times 10^{-5} \text{ s}^{-1}$  under constant stress before a strain of 0.02 is reached. This minimum strain rate is similar to the one of the conventional specimen being  $1.52 \times 10^{-5} \text{ s}^{-1}$ . After the minimum creep strain rate, both creep curves showed increasing creep rates until a plateau with  $4.53 \times 10^{-5} \text{ s}^{-1}$  under constant load and  $3.93 \times 10^{-5} \text{ s}^{-1}$  under constant stress conditions is reached. The creep curve under constant load has smaller fracture strain and shorter plateau in the steady-state creep stage, which can be explained by the increased stress on the cross-section due to the continuous elongation of the specimen.

The L200 specimens showed a minimum creep strain rate  $1.29 \times 10^{-5} \text{ s}^{-1}$  under constant load and  $1.24 \times 10^{-5} \text{ s}^{-1}$  under constant stress conditions before a strain of 0.02. No plateau or steady-state creep stage was observed. No difference in creep behavior was observed for the L200 specimens un-



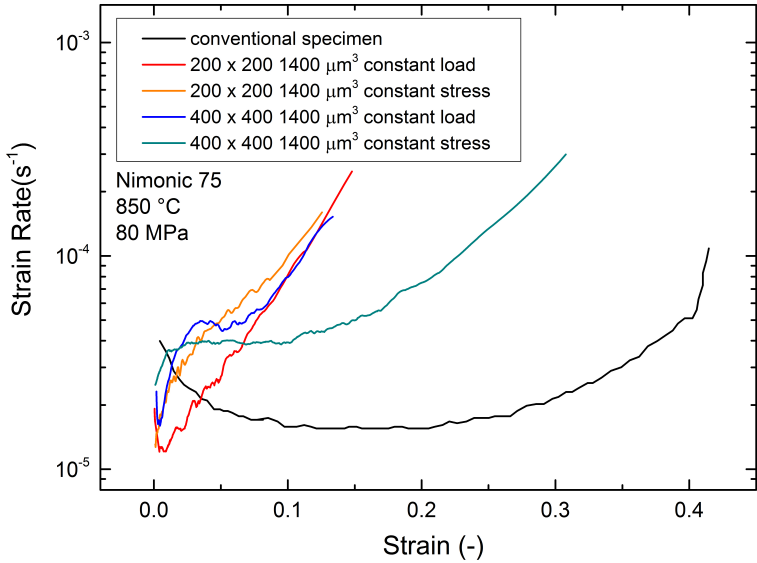


Figure 3.1: Creep curves of the miniaturized specimens tested at 850 °C and 80 MPa under constant load and constant stress in comparison with the conventional specimen (diameter 6 mm, gauge length 30 mm) [82, 83].

der constant load or constant stress load conditions. The creep strain rates increased continuously after the minimum creep rate.

The dependence of minimum creep rate on the stress of the Nimonic 75 miniaturized specimens tested at temperature 850 °C was plotted as the Norton-plot in Figure 3.2. Regardless of the different creep behaviors of the miniaturized specimens compared to the conventional specimens, the minimum creep strain rates of the miniaturized specimens showed a good agreement with the literature data of the conventional specimens. The minimum creep strain rates of the miniaturized specimen tested under stress from 20 to 70 MPa fall into the same range as the steady-state values of the conventional specimens. For stress above 70 MPa, increased minimum creep strain rates of the miniaturized specimens were observed and the scatter of

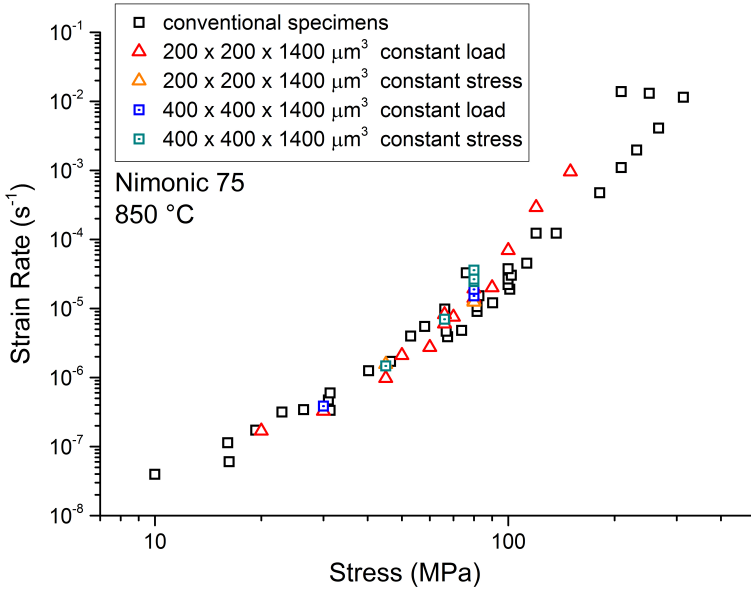


Figure 3.2: Norton-plot of Nimonic 75 summarizing minimum creep strain rates at 850 °C in comparison of the steady-state creep strain rates of the conventional specimens (diameter 6 mm, gauge length 30 mm) from the literature [82, 83]

the data points is increased. All the fracture strains of the L200 specimens are below 0.15. For the L400 specimens, due to the increased cross-section, the fracture strains lie in the range of 0.1 ~ 0.35, while the fracture strains of the conventional specimens usually are larger than 0.3 [83]. All the creep curves of the miniaturized specimens showed a thickness debit effect [11] that reduced fracture strain and early onset of tertiary creep stage were observed.

The creep results of the L200 and L400 miniaturized specimens tested at 1000 °C and 40 MPa with constant load and constant stress until fracture are plotted in Figure 3.3. The creep behavior of the L200 and L400 miniaturized specimens also showed a dependence on the specimen sizes. Both L400 specimens showed a minimum creep strain rate before a strain of 0.02

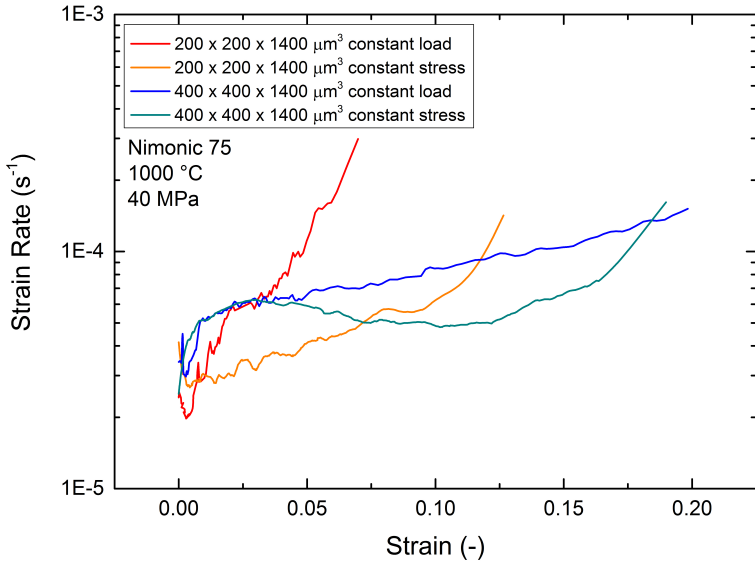


Figure 3.3: Creep curves of the miniaturized specimens tested at 1000 °C and 40 MPa by constant load and constant stress

was reached, which assumed values of  $2.92 \times 10^{-5} \text{ s}^{-1}$  under constant load and  $2.96 \times 10^{-5} \text{ s}^{-1}$  under constant stress. After the minimum creep strain rate, an increment of the creep strain rate was observed in both creep curves. The specimen under constant load has an increasing creep strain rate until fracture. Meanwhile, the specimen under constant stress showed a secondary creep stage with a second minimum creep strain rate of  $4.82 \times 10^{-5} \text{ s}^{-1}$ .

For the L200 specimens, only minimum creep strain rates with values of  $2.04 \times 10^{-5} \text{ s}^{-1}$  under constant load and  $2.89 \times 10^{-5} \text{ s}^{-1}$  under constant stress were observed. After the minimum creep strain rates, both creep curves showed increasing creep strain rates until fracture, no secondary creep stage was detected. For the specimen under constant load, the increment of the creep strain rate was faster compared to the specimen under

constant stress, which can be explained again by the increasing stress on the specimen under constant load. Even though there is no creep curve of a conventional specimen for comparison, the miniaturized specimens also showed a thickness debit effect at a higher temperature, reduced creep resistance is detected with smaller specimen sizes.

Creep results of Nimonic 75 miniaturized specimens tested at a temperature of 1000 °C with initial stresses from 10 to 80 MPa were plotted as the Norton-plot in Figure 3.4. The minimum creep strain rates of both L400 and L200 miniaturized specimens under constant load and constant stress conditions showed good agreement with the literature data of the conventional specimens. For stresses larger than 80 MPa, no reliable data points were available due to the too fast creep strain rates for the customized setup. The fracture strains of the L200 specimen were all under 0.15, while the fracture strain of the L400 usually is larger than 0.2.

Additional tensile creep tests of the L200 miniaturized specimens at initial stress 30 MPa under temperature 900 °C and 950 °C were done to calculate the activation energy. In Figure 3.5 the activation energy of the L200 miniaturized specimens has been determined to be 303 kJ/mol, which is in good agreement with the results of the conventional specimen of 285 kJ/mol. This is supported by the activation energies for self-diffusion and Cr diffusion according to Frost and Ashby [101].

Figure 3.6 shows all the creep results of the miniaturized specimens and the conventional specimens in one joint Norton Plot. In this Figure, the following points from the tensile creep tests of the Nimonic 75 miniaturized specimens can be summarized:

The minimum creep strain rates and the activation energy of creep of both L200 and L400 specimens were in good agreement with the results of the conventional specimens, which suggest that the accuracy and stability of the customized setup meets the requirement of tensile creep tests with miniaturized specimens up to temperature 1000 °C.

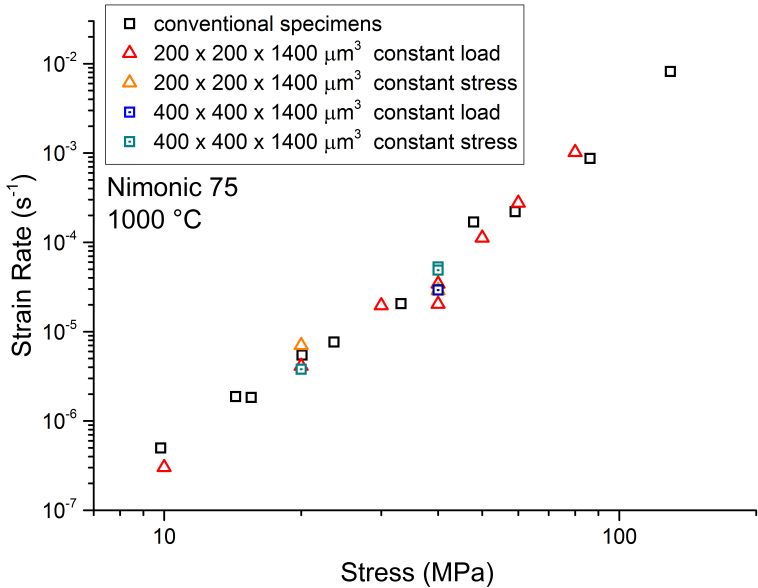


Figure 3.4: Norton-plot of Nimonic 75 summarizing minimum creep strain rates at 1000 °C in comparison of the steady-state creep strain rates for conventional specimens (diameter 6 mm, gauge length 30 mm) from the literature [82, 83]

Reduced creep resistance of the miniaturized specimens compared to the conventional specimens was observed for the miniaturized specimens tested in both temperatures and specimen sizes. For the L200 specimens, no secondary creep stage was obtained, the creep strain rates increased continuously after the minimum creep strain rates until fracture, the fracture strains are all below 0.15. For the L400 specimens, an increment of strain rate can be obtained after the minimum creep strain rate point. Subsequently, a short secondary creep stage with increased creep strain rates appeared.

The minimum creep strain rates of the miniaturized specimens under constant load and constant stress conditions showed similar results because most minimum creep strain rates were observed at strain smaller than 0.05 so that the difference of the effective stress between these two load methods

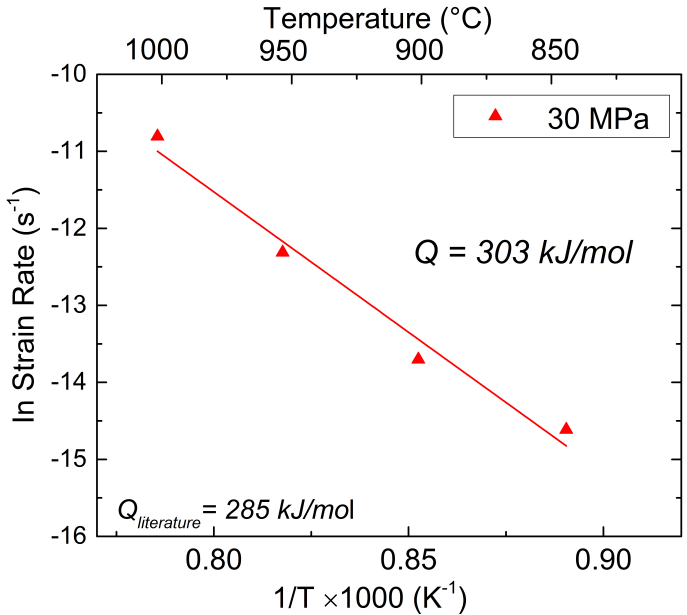


Figure 3.5: Arrhenius plot for an initial stress level of 30 MPa for four temperatures of 850, 900, 950 and 1000 °C, respectively.

can be ignored. But the creep curves of the miniaturized specimens under constant load showed accelerated creep strain rates after the minimum creep strain rate points and an earlier appearance of tertiary creep stage. This was observed because of the increased effective stress on the reduced cross-section during specimen elongation.

At temperature 850 °C with stress over 70 MPa, the minimum creep strain rates of the miniaturized specimens are apparently higher than the results of the conventional specimens and the data dispersion is also increased, which suggests that the creep behavior of the miniaturized specimens is sensitive to the magnitude of the initial stress.

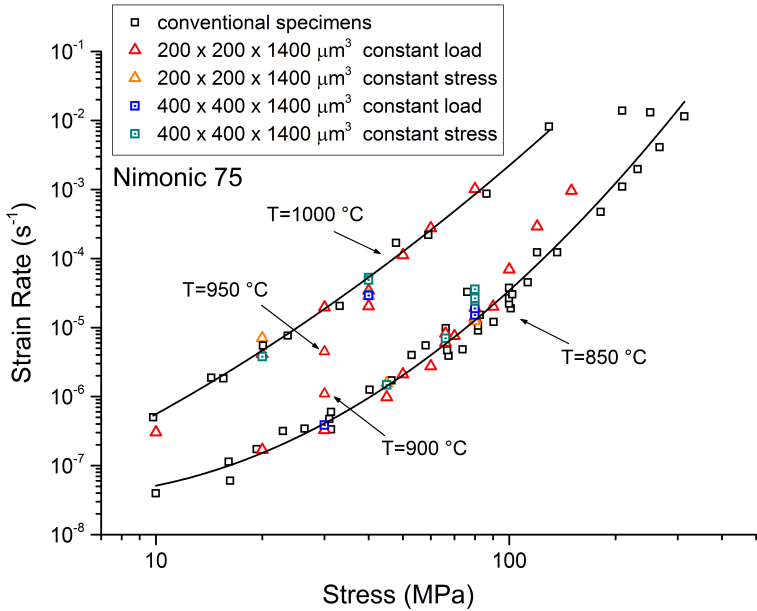


Figure 3.6: Norton-plot of Nimonic 75 summarizing minimum creep strain rates at 850 °C and 1000 °C in comparison of the steady-state creep strain rates for conventional specimens from the literature [82, 83]

From all the results above, even though the minimum creep strain rates of the miniaturized specimens were in good agreement with the steady-state creep strain rates of the conventional specimens, the different creep behaviors of the miniaturized specimens need to be investigated to understand the unusual creep properties. In the next section, the following influencing factors will be discussed:

1. Influence of the strain distribution on the miniaturized specimens.
2. Influence of the grain size on the different miniaturized specimen sizes.
3. Influence of oxidation at temperatures 850 °C and 1000 °C.

## 3.3 Characterization of the miniaturized specimens

### 3.3.1 Analysis of strain distribution

The evolution of the strain distribution of one L200 and one L400 specimen tested at 850 °C and constant stress 80 MPa was analyzed with the DIC method. Since increasing creep strain rates were already observed at the early creep stage of the L200 specimen (see Figure 3.7 (a)), the analysis of the strain distribution will more focus on the early creep stage. The strain distributions of both specimens were analyzed and compared with each other at global strains of 0.005, 0.01, 0.02 and up to 0.05, where the L400 specimen reached the steady-state creep stage.

Figure 3.7 (b) shows the results of the strain distribution in the direction along the gauge length of both miniaturized specimens up to a global strain of 0.05. The results of the strain distribution of the L200 specimen are shown in the red frame and the L400 specimen in the blue frame. The colorbars in each figure are set to be 1.5 times of the current global strain. For the L200 specimen at a strain of 0.005, two areas on the specimen showed evident strain localization at a level over 0.0075 resulting in an inhomogeneous strain distribution even at the very beginning of the tensile creep test. With increased strain, the distribution of the strain localization remains similar in shape and the strain magnitude in the localization areas increased continuously until fracture. Therefore the creep strain rate of the L200 specimen kept increasing due to the intense strain localization. Meanwhile, for the L400 specimen, a more homogeneous strain distribution was observed compared to the L200 specimen, and the evolution of a slight strain localization was detected starting at a strain of 0.02.

Figure 3.8 shows the images of these two specimens just before and after fracture, together with the corresponding strain distribution. Specimen fracture in both specimens was located in the areas with the strongest strain



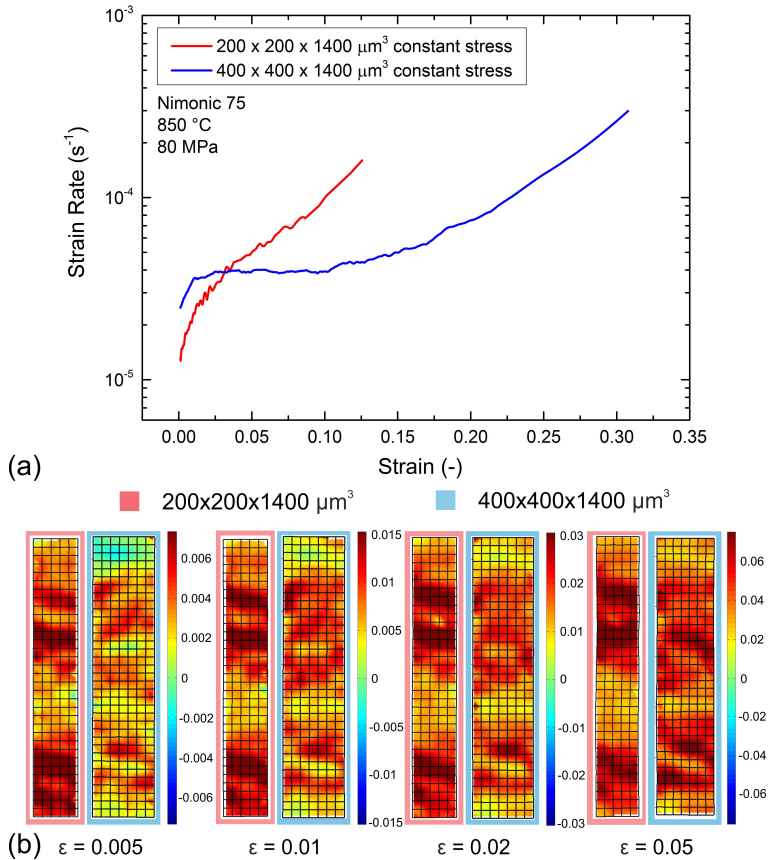


Figure 3.7: (a) Creep curves of one L200 and one L400 specimen tested at 850 °C and constant stress 80 MPa for the strain distribution analysis. (b) Strain distribution of both miniaturized specimens at global strains of 0.005, 0.01, 0.02 and 0.05.

localization. These areas are the same locations, where strain localization was first observed at the beginning of the creep tests, which implied that some damage already appeared in the miniaturized specimens at the beginning of the creep tests. The L400 specimen showed a more homogeneous strain distribution and a better resistance to strain localization due to its lar-

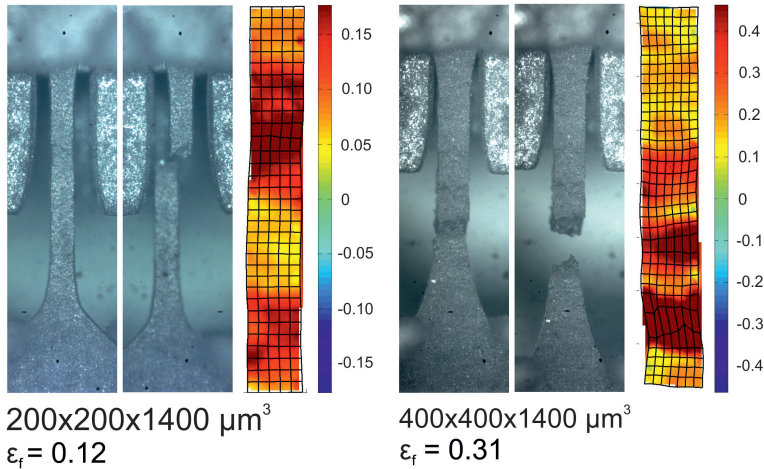


Figure 3.8: Specimen images and strain distribution of one L200 and one L400 specimen tested at constant stress 80 MPa and 850 °C before fracture

ger cross-section compared to the L200 specimen so that the creep behavior of the L400 specimen is more similar to the conventional specimen.

### 3.3.2 Influence of crack generation

By the analysis of the strain distribution on the L200 and L400 specimens, the different creep behavior of the miniaturized specimens is believed to be an early strain localization which leads to increased creep strain rates. One L200 and one L400 specimen were tested at 850 °C at constant stress 80 MPa to study the cause of the strain localization, and both tests were interrupted at a strain of 0.05. Afterwards, both specimens were mechanically polished. The corresponding strain distribution was analyzed and compared with the material damage observed in the polished specimen surfaces. Figure 3.9 shows the results of these two specimens and another L400 specimen, which was tested at the same condition and interrupted just before fracture. Figure 3.9 shows that both specimens at a strain of 0.05 have strain

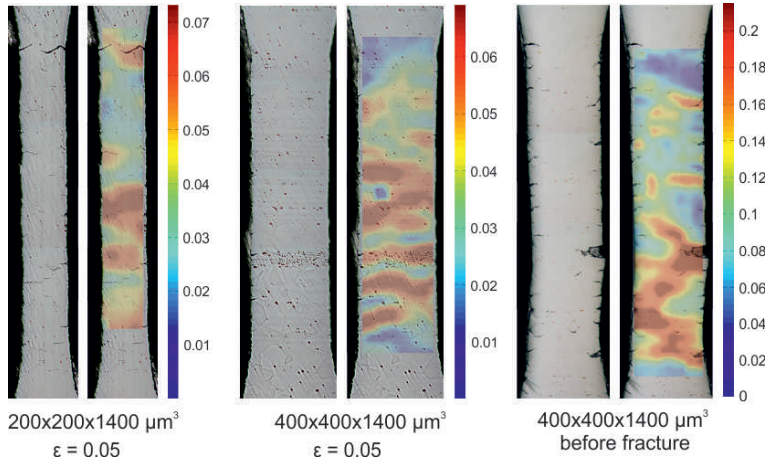


Figure 3.9: Analysis of the strain distribution and mechanically polished surface of the miniaturized specimens tested at 850 ° and constant stress 80 MPa, which were interrupted at a strain of 0.05 and before fracture

localization at the cracks, which were generated from the specimen surfaces and grew intergranular. For the L200 specimen, due to its relatively smaller cross-section compared to the L400 specimen, the resistance to crack growth is weaker and some cracks went through half the width of the specimen, consequently, a strong strain localization was detected. For the L400 specimen, no evident crack growth was found at a strain of 0.05. Still, some cracks were generated from the specimen surface and caused strain localization, but most cracks were stopped at the triple points in the grain boundaries. For the L400 specimen just before fracture, more cracks generated from the specimen surface were observed and grew until the triple points. One major crack grew intergranularly and is the potential fracture position. This result indicates that the cracks generated from the specimen surface are responsible for the strain localization in the miniaturized specimens.

In order to study the fracture mechanism and the influence of cracks on the miniaturized specimens under different temperature and initial stress condi-

tions, specimens in both sizes were tested at 850 °C with relative smaller stress 45 MPa and larger stress 80 MPa and at 1000 °C with stresses of 20 MPa and 40 MPa until fracture. All the specimens were mechanically polished to analyze the fracture mechanism, the results are shown in Figure 3.10 and Figure 3.11.

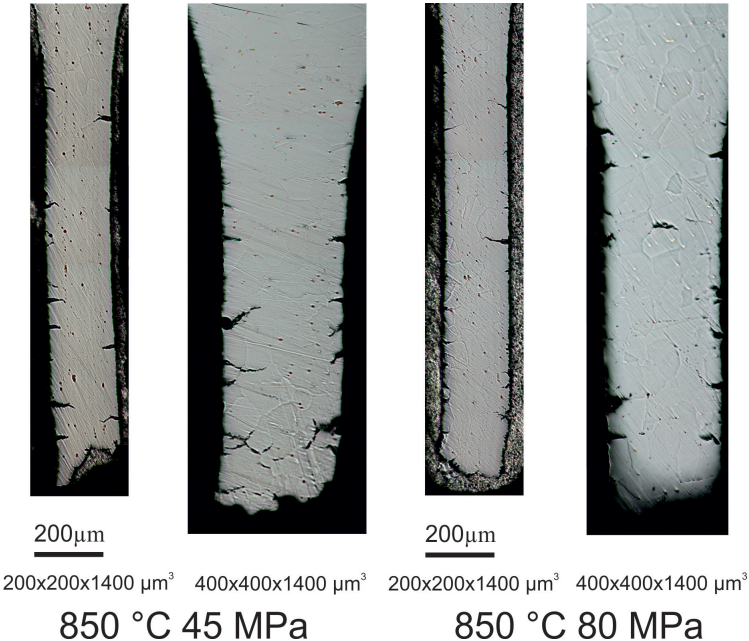


Figure 3.10: Mechanically polished surfaces of the L200 and L400 specimens tested at 850 °C under stress 45 MPa and 80 MPa after fracture.

At 850 °C 45 MPa, more cracks generated from the specimen surfaces were observed in the L400 specimen compared to the L200 specimen. Most cracks in both specimens stopped at the triple points among the grain boundaries and their growth directions are vertical to the load direction. At 850 °C and 80 MPa, a reduced crack density in both specimens was observed in comparison with the same specimens tested at 45 MPa. This suggests that

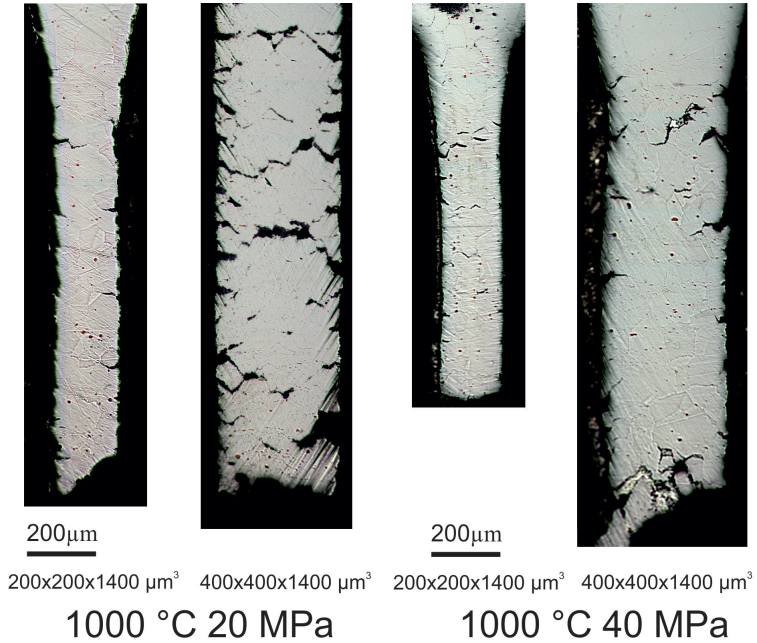


Figure 3.11: Mechanically polished surfaces of the L200 and L400 specimens tested at 1000 °C under stress 20 MPa and 40 MPa after fracture

the propagation of individual cracks at high stress is dominant since more stress increment is expected with larger initial stress when the cross-section area is reduced due to crack growth. Additionally, the increased creep strain rate at larger initial stress provides less time for other cracks to grow by coalescence of voids due to grain boundary diffusion. Therefore a reduced crack density was observed in the miniaturized specimens tested at larger initial stress. At 1000 °C and 20 MPa, lots of intergranular cracks were observed in the L400 specimen, which is similar to the intergranular creep fracture in conventional polycrystal specimens [111], while the L200 specimen have fewer cracks indicating the domination of the propagation of individual cracks. At 1000 °C and 40 MPa, both specimens showed reduced

crack density due to the increased stress. This phenomenon suggests again that the resistance of the miniaturized specimens to cracks is weaker with smaller cross-section and increased initial stress even at a higher temperature. It is also noteworthy, an increased density of intergranular cracks was observed in the miniaturized specimens tested at 1000 °C compared to the specimens tested at 850 °C, especially for the L400 specimen at 20 MPa. This is because of the increased grain boundary diffusion rate at a higher temperature.

Cracks generated from the specimen surfaces were observed in all the miniaturized specimens under different experimental conditions, which led to strain localization. The most cracks were stopped at the triple points among the grain boundaries so that the minimum crack length is dependent on the grain sizes. Considering the ratio of the average grain size (70...110  $\mu\text{m}$ ) and the cross-section of the miniaturized specimens, the stress increase in the reduced cross-section due to cracks is more significant in the L200 specimens compared to the L400 specimens. Consequently, the L200 specimens showed more accelerated creep strain rates compared to the L400 specimens, especially at larger initial stress. Therefore the creep behavior of polycrystal Nimonic 75 is sensitive to the ratio of grain size and specimen sizes. According to test results, the primary fracture mechanism of the miniaturized specimens is the generation of cracks from the specimen surfaces resulting in strain localization and the intergranular propagation of cracks due to increased local stress.

The creep behavior of the miniaturized specimens is not only dependent on the ratio of the specimen size to the grain size but is also sensitive to the distribution of the grain boundaries along the specimen surfaces. Figure 3.12 (a) shows the creep curves of four L400 specimens tested at 850 °C and stress 80 MPa under constant load and constant stress test conditions, respectively. The creep strain rate curves of the four specimens are already obviously different at strain smaller than 0.02, where the stress increment on

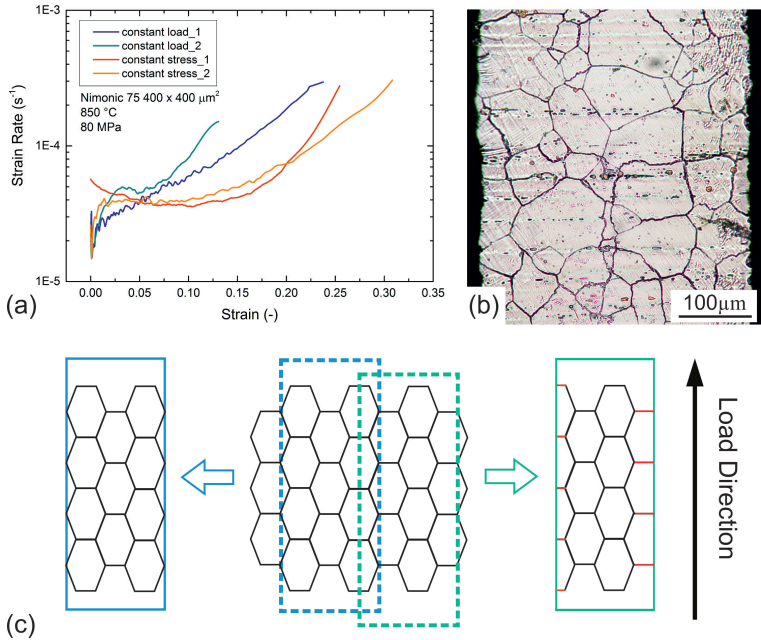


Figure 3.12: (a) Different creep behavior of the miniaturized specimens tested at 850  $^{\circ}C$  and 80 MPa were determined at the beginning of the creep tests. (b) Distribution of grain boundaries along the surfaces of one L400 specimen. (c) Schematic diagram to explain the influence of cut position on grain boundary distribution

the specimens due to the constant load condition could be ignored. A possible reason to explain the variation of the creep curves is the different grain boundary distribution along the specimen surfaces. Figure 3.12 (b) shows the electropolished surface of one L400 specimen, the grains with different sizes were observed near the specimen surface, and their grain boundaries showed also different direction to the specimen surface. Three factors of the grain boundary distribution on the specimen surfaces may affect the crack generation from the specimen surfaces and the creep behavior of the miniaturized specimens:

1. The density of the grain boundaries on the specimen surfaces: If there are more grain boundaries per area on the specimen surfaces, the probability of crack generation is naturally increased. The density of the grain boundaries on the specimen surfaces is also dependent on the average grain sizes, which is larger with smaller average grain sizes on the specimen surfaces.

2. The angle between the grain boundaries and the load direction. The propagation of cracks along grain boundaries with direction vertical to the load direction is optimal for energetic reasons [112, 113], therefore the direction of most of the cracks generated from surfaces was vertical to the load direction as shown in Figure 3.10 and Figure 3.11 regardless of temperature and stress. The majority of cracks grew until they reached triple points between grain boundaries and stopped because the direction of a new grain boundary is generally not vertical to the load direction and more energy is needed for the propagation of the cracks.

3. The length of cracks from specimen surfaces to the first triple point directly influences the magnitude of the cross-section reduction. The crack length is not only dependent on the average grain sizes but also sensitive to the cut position of the miniaturized specimens from the bulk material. If the cut surface is at the edge of the grains, the potential crack length could be the whole grain boundary, vice versa. Figure 3.12 (c) shows a schematic diagram as an example for two extreme cases, where two specimens are assumed to be cut from the same bulk material with identical grain size. The difference of the grain boundaries distribution along both specimen surfaces is dependent on the cut position. On the surfaces of the left specimen, there are no grain boundaries with direction vertical to the load direction, while on the surfaces of the right specimens, such grain boundaries are present, which could cause potential crack generation. Therefore the creep behavior of these two specimens could be different even with the same microstructure and specimen size.



According to these influencing factors, the creep behavior of each specimen at the same experimental condition is different due to their unique grain boundaries distribution on the specimen surfaces. Especially, if the miniaturized specimens are tested at larger initial stress, the increased creep strain rate provides less time for cracks generated on vertical grain boundaries by diffusional growth of voids. Hence, the crack initiation on the specimen surfaces has a dominating influence on the creep behavior. This assumption may, therefore, explain the different creep behavior and the increased scatter of the minimum creep strain rates of the L400 specimens at 850 °C and 80 MPa.

### 3.3.3 Influence of oxidation

Since all the miniaturized specimens were tested in air condition, the influence of oxidation on creep behavior needs to be studied. The oxide layer of the miniaturized specimens tested at temperature 850 °C and 1000 °C were analyzed with Scanning Electron Microscope (SEM) and Focused Ion Beam (FIB). The thickness of the oxide layer was measured and the corresponding influence on the creep behavior will be discussed.

Figure 3.13 shows the oxide layers of the miniaturized specimens tested at 850 °C until fracture. Figure 3.13 (a) shows one FIB cut section of one L400 specimen tested at 30MPa with a fracture time of 77 hours, the maximum thickness of the oxide layer is 1.97  $\mu\text{m}$ . Figure 3.13 (b) shows one L200 specimen tested at 45MPa with a fracture time of 17 hours, the maximum thickness of the oxide layer is 1.63  $\mu\text{m}$ . An oxide layer was formed along one crack, where voids between the oxide layer and inner material were observed. The thickness of this oxide layer is thicker than the oxide layer on the specimen surface. Figure 3.13 (c) shows one L200 specimen tested at 70MPa with a fracture time of 0.8 hours, the maximum thickness of the oxide layer in the FIB cut section is 1.34  $\mu\text{m}$ . Figure 3.13 (d) shows a crack

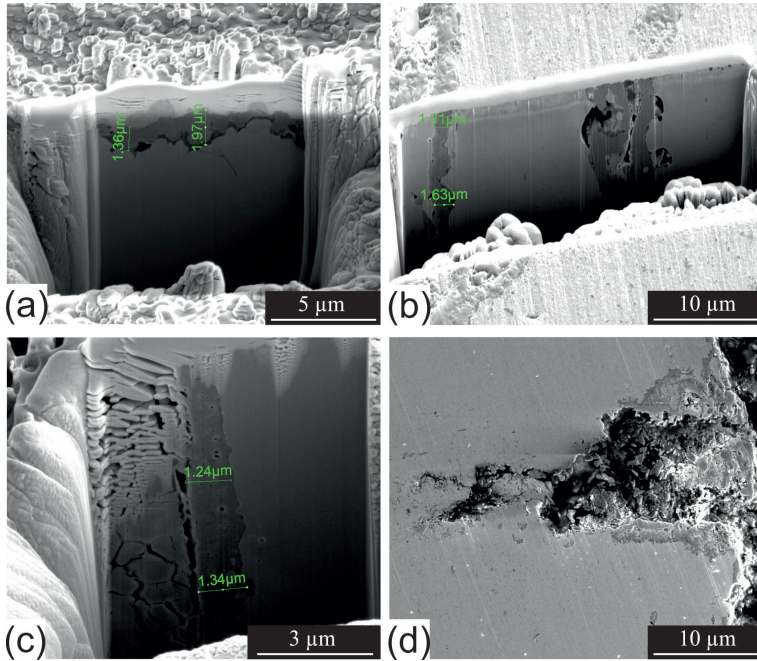


Figure 3.13: Analysis of the oxide layer at 850 °C from: (a) one L400 specimen tested at 30MPa, (b) one L200 specimen tested at 45MPa and (c) one L200 tested at 70MPa. (d) oxidation in the crack of the L200 specimen tested at 70MPa

generated from the surface of this L200 specimen, oxide layer was observed along the crack resulting in accelerated crack growth.

At temperature 1000 °C, the oxide layer of one L200 specimen tested at 20 MPa is shown in Figure 3.14 (a). The fractured time is 12 hours and the maximum thickness of the oxide layer is 2.25 μm in the FIB cut section. Figure 3.14 (b) shows the oxidation status of one crack generated from this specimen surface. An oxide layer is observed even at the tip of the crack, which may have increased the growth rate of the crack resulting in an increased creep strain rate. Figure 3.14 (c) shows the oxide layer of one L400 specimen tested at 20 MPa with a fracture time of 94 hours, the maximum

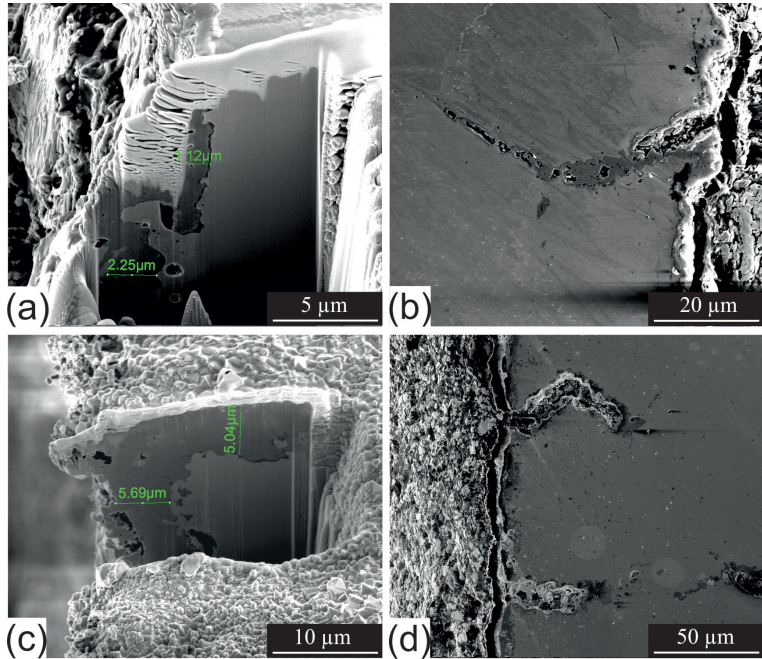


Figure 3.14: Analysis of the oxide layer at 1000 °C from: (a) one L200 specimen tested at 20MPa and (b) the oxidation status of one crack generated from this specimen surface, (c) one L400 specimen tested at 20MPa and (d) the oxidation status of cracks generated from this specimen surface.

thickness of the oxide layer in the FIB cut section is 5.69  $\mu\text{m}$ . Figure 3.14 (d) shows cracks generated from this specimen surface, where oxide layers along the cracks can be observed. The oxide layer thickness increased obviously with longer fracture time at temperature 1000 °C compared to the oxide layer thickness at 850 °C.

The thickness of the oxide layer of all the miniaturized specimens increased with larger fracture time and higher temperatures. Considering the oxide layer has no load-bearing capacity, the actual stress on the cross-section of the miniaturized specimens is underestimated. The corresponding stress

error  $\Delta\sigma$  caused by the oxide layer during constant stress tensile creep tests can be calculated as:

$$\begin{aligned}
 S' &= \frac{V}{L \cdot (1 + \varepsilon)} = S_0 \cdot \frac{1}{1 + \varepsilon} \\
 \sigma_{true} &= \frac{S' \cdot \sigma_0}{(S'^{\frac{1}{2}} - 2 \cdot t_{oxide})^2} \\
 \Delta\sigma &= \frac{\sigma_{true} - \sigma_0}{\sigma_0} = \frac{S'}{(S'^{\frac{1}{2}} - 2 \cdot t_{oxide})^2} - 1
 \end{aligned} \tag{3.1}$$

All the micro-tensile creep tests were carried out in air, hence the specimen grains volume as a result of oxidation. However, this effect is negligible compared to the reduction of the cross-section caused by the oxide layer. Therefore we assume that the volume of the miniaturized specimen remains constant in our case.  $S'$  here is the deformed cross-section, which can be calculated from the strain  $\varepsilon$ .  $t_{oxide}$  is the thickness of the oxide layer. Here the thickness of the oxide layer from 0 to 6  $\mu\text{m}$  and the strain  $\varepsilon$  from 0.01 to 0.3 are used in this formula to calculate the stress error  $\Delta\sigma$ . The result is shown in Figure 3.15.

At 850 °C, the maximum thickness of the oxide layer observed is 1.97  $\mu\text{m}$ , the stress error  $\Delta\sigma$  with the initial cross-section, i.e., without strain, under the influence of this oxide layer is 4.1% for the L200 specimen and 2% for the L400 specimen. At strain 0.3, generally the maximum strain observed in the miniaturized specimens, the stress error is 4.7% for the L200 specimen and 2.3% for the L400 specimen. At 1000 °C, the maximum thickness of the oxide layer observed is 5.69  $\mu\text{m}$ , The stress error is then 13.2% for the L200 specimen and 6.3% for the L400 specimen with the initial cross-section. At strain 0.3, the stress error is increased to 15.2% for the L200 specimen and 7.2% for the L400 specimen. This result implied that the L200 specimens contain larger stress errors than the L400 specimens with the identical strain and oxide layer thickness due to the smaller cross-section. Simultaneously,

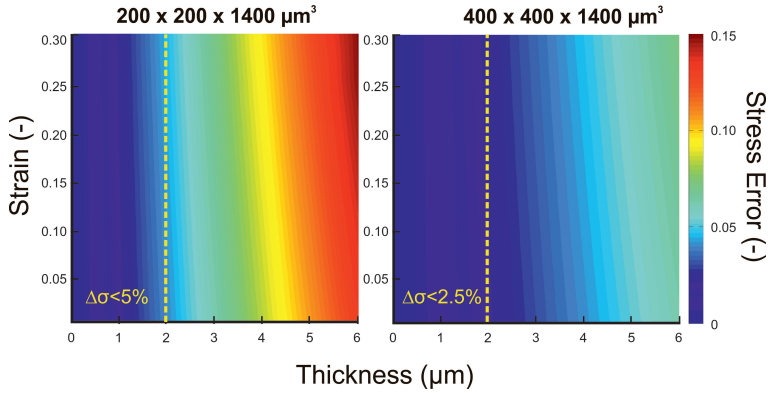


Figure 3.15: Analysis of stress error caused by the cross-section reduction due to strain and thickness of the oxide layer, the dash lines indicate the maximum stress error at minimum creep strain rate points.

the main influencing factor of the stress error is the magnitude of the oxide layer thickness, the stress error increment caused by the increasing strain is negligible compared to the influence of the increasing oxide layer thickness. The minimum or steady-state creep strain rates of most specimens were located at strain smaller than 0.05, where the thickness of the oxide layer is generally below 2  $\mu\text{m}$ . The corresponding stress error is then below 5% for the L200 specimens and below 2.5% for the L400 specimens, which means the stress error caused by the oxide layer has a negligible influence on the creep behavior of the miniaturized specimens. The main factor affecting the creep behavior is still the stress concentration due to cracks generated from the specimen surfaces.

### 3.4 Summary for Nimonic 75 miniaturized specimens

Tensile creep tests with the L200 and L400 miniaturized specimens were successfully carried out at temperatures 1000  $^{\circ}\text{C}$  and 850  $^{\circ}\text{C}$  under constant

load and stress conditions with the customized setup. A particular creep behavior of the miniaturized specimens was observed:

The L200 and L400 miniaturized specimens have reduced fracture strains compared to the conventional specimens. The L200 specimens have smaller fracture strains than the L400 specimens. Most miniaturized specimens have minimum creep strain rates located at strain around 0.02 under constant load or constant stress conditions, which are independent on the loading methods and specimen sizes, and their values showed a good agreement with the steady-state creep rates of the conventional specimens.

Strain distribution analysis with the DIC method showed that strain localization was observed in both L200 and L400 specimens at the beginning of creep tests (see Figure 3.7). The strain localization was caused by the intergranular cracks generated from the specimen surfaces resulting in increased creep strain rates, which is the main factor influencing the creep behavior of the miniaturized specimens. All the miniaturized specimens were tested in air, a dense and adherent oxide layer was observed on the surface of the miniaturized specimens. The stress error caused by the oxide layer is below 5% for the L200 specimens and below 2.5% for the L400 specimens, which has a negligible influence on the creep behavior.

In conclusion, by using Nimonic 75 polycrystal as reference material, the customized setup was proven to show adequate accuracy and stability to fulfill the requirement for tensile creep testing with the miniaturized specimens in sub-mm scale. Thickness debit effect was observed in the Nimonic 75 polycrystalline miniaturized specimens, the creep behavior showed a significant dependence on the ratio of the grain size to specimens size, where decreasing creep resistance was observed in specimens with smaller sizes due to cracks generated from specimen surfaces, which led to stress localization and increasing creep strain rates. In the next section, the creep properties of miniaturized NiAl single crystalline specimens will be presented and discussed.

## 4 Tensile creep testing of NiAl single crystals

The intermetallic alloy NiAl provides excellent oxidation resistance, reduced density compared to other Nickel-based superalloys and very high thermal conductivity [84–86], which makes NiAl alloy a promising candidate for the next generation of high-temperature materials. However, the low creep strength limited the application of NiAl at elevated temperatures, such as in gas turbine engines. Strengthening with oxide dispersion [87] or directional solidification technique to process NiAl-based composites with reinforcing second phases [88–90] were provided to be promising methods to improve the creep resistance by numerous studies. The miniaturized NiAl single crystalline specimens were tested for two purposes: First, NiAl single crystals are considered as matrix materials in the enhanced materials, the understanding of the creep behavior of NiAl single crystalline miniaturized specimens is the basis for subsequent research of the enhanced materials. The influence of specimen miniaturization on the creep behavior of NiAl single crystals was studied by comparing to the conventional specimen [91–93]. Second, the creep behavior of NiAl single crystals shows a strong dependence on the crystal orientations: In the [110] soft orientation, the creep deformation is dominated by the glide of  $\langle 001 \rangle$  dislocations [94–97]. In the [100] hard orientation, where no driving force exists for the  $\langle 001 \rangle$  dislocations, the motion of  $\langle 011 \rangle$  dislocation is considered to be important to the creep deformation at elevated temperatures [93,98–100]. In the work of Mills et al. [127] and Srinivasan et al. [128, 129], they have reported that  $\langle 011 \rangle$  dislocations decompose into two separate  $\langle 010 \rangle$  dis-

locations. After decomposition, the edge part of the  $\langle 011 \rangle$  dislocation is effectively sessile and can move only via  $\langle 010 \rangle$  dislocation climb. Hence, larger stress is required to obtain the same creep rates as in the soft orientation. Therefore, it is also scientifically interesting to study the influence of crystal orientations on the creep behavior of miniaturized specimens.

## 4.1 Specimen preparation

The bulk material was available as a cylindrical NiAl single crystal with diameter 20 mm and height 30 mm, which was provided by Max Planck Institut für Eisenforschung (MPIE) in Düsseldorf. The long axis of the cylinder is determined with XRD from Max Plank Institute for Intelligent Systems as  $[\bar{1}\bar{1}\bar{1}]$  oriented and one surface was cut perpendicularly to the  $[\bar{1}\bar{1}0]$  orientation as shown in Figure 4.1(a).

Figure 4.1 (b) shows the manufacturing methods of the miniaturized specimens in  $[110]$  soft and  $[100]$  hard orientations. For the  $[110]$  soft orientation, the miniaturized specimens with gauge length perpendicular to the cut surface were manufactured by EDM, these specimens are  $[\bar{1}\bar{1}0]$  oriented in the gauge length and  $[\bar{1}\bar{1}\bar{1}]$  oriented in one specimen surface. For the  $[100]$  hard orientation, the miniaturized specimens were cut with an angle of  $54.74^\circ$  tilted from the long axis of the cylindrical crystal, these specimens are  $[001]$  oriented in the gauge length and  $[\bar{1}\bar{1}0]$  oriented in one specimen surface. All the specimens were mechanically polished with 2000 and 4000 grit sandpapers to remove the recast layer caused by the EDM process and reduce the surface roughness to prevent early strain localization. Before micro-tensile creep tests, the thickness and width of the miniaturized specimens were measured for accurate stress calculation, and a surface roughness of  $\pm 1 \mu\text{m}$  was observed.



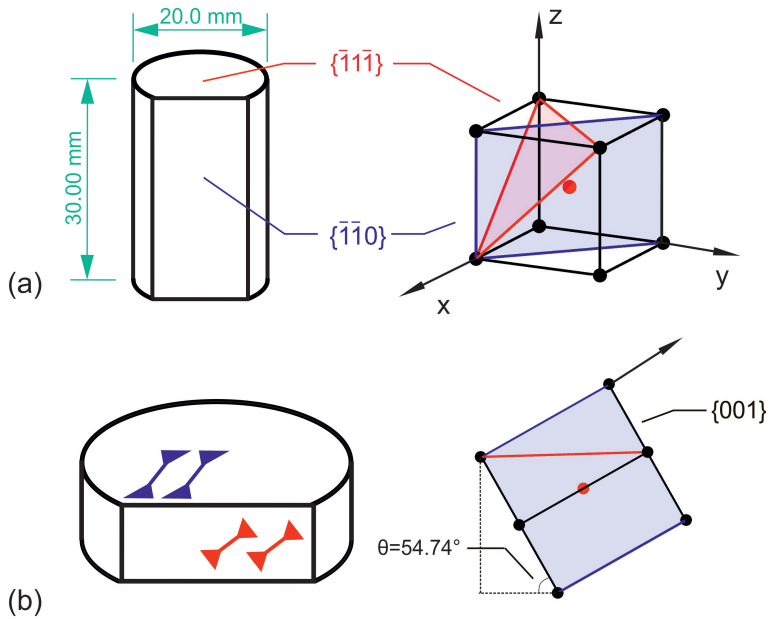


Figure 4.1: Schematic diagram of specimen preparation shows (a) orientation determination from the cylindrical NiAl single crystal and (b) the miniaturized specimens manufactured in [110] soft orientation (blue specimens) and [100] hard orientation (red specimens)

## 4.2 Tensile creep testing in [110] soft orientation

### 4.2.1 Experimental results

The miniaturized specimens of NiAl in [110] soft orientation were tested at 1000 °C in air under constant stress 20 MPa, 25 MPa and 30 MPa in different specimen sizes. Not only the miniaturized specimens in sizes of  $200 \times 200 \times 1400 \mu\text{m}^3$  and  $400 \times 400 \times 1400 \mu\text{m}^3$  were tested, an additional group of  $300 \times 300 \times 1400 \mu\text{m}^3$  specimens was designed so that the influence of different specimen's width and thickness on the creep behavior can

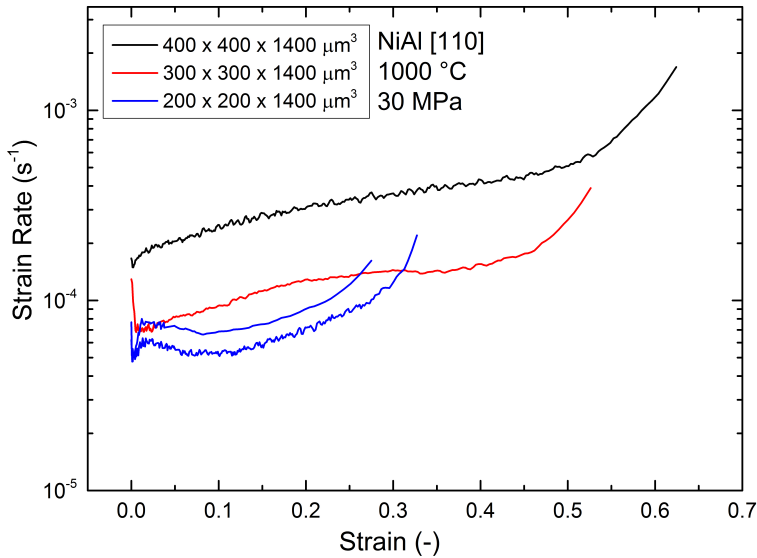


Figure 4.2: Creep curves of NiAl single crystalline miniaturized specimens tested at 1000 °C and 30 MPa in [110] soft orientation

be systematically studied. All three groups of the miniaturized specimens were abbreviated as L200, L400 and L300 for convenient identification.

Figure 4.2 shows the results of the specimens tested at 30 MPa with three different specimen sizes, the creep curves were plotted in the form of strain rates ( $\text{s}^{-1}$ ) vs. strain (-). Specimens with smaller sizes showed reduced fracture strains. This phenomenon is similar to the test results of the Nimonic 75 polycrystal miniaturized specimens. However, the minimum creep strain rates are surprisingly reduced with smaller specimen sizes. After the points of minimum creep strain rates, the L300 and L400 specimens showed continuously increasing creep strain rates until fracture, while the L200 specimens showed first increased strain rates with strain up to 0.02, subsequently work hardening effect was observed in both L200 specimens resulting in a second minimum creep strain rate points at strain around 0.1.

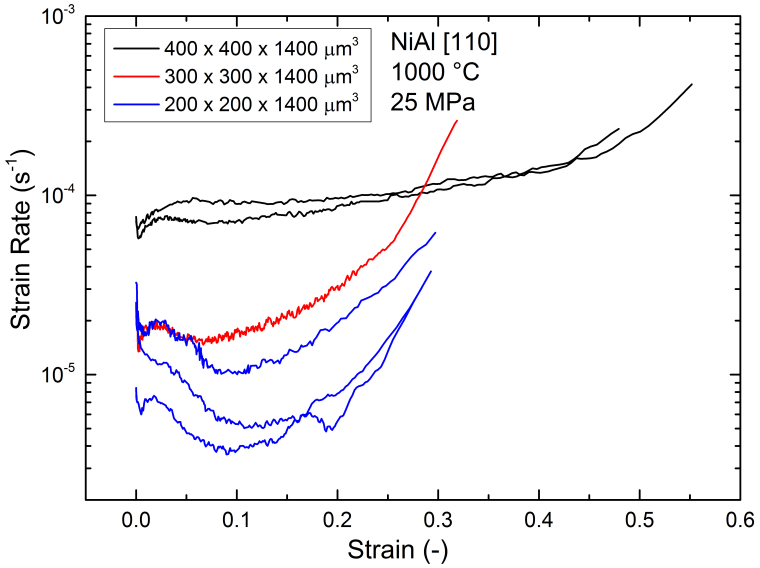


Figure 4.3: Creep curves of NiAl single crystalline miniaturized specimens tested at 1000 °C and 25 MPa in [110] soft orientation

The miniaturized specimens tested at 25 MPa (see Figure 4.3) showed similar creep behavior at 30 MPa: smaller fracture strains and minimum creep strain rates were observed with reduced specimen sizes. The creep curves of the L200 specimens displayed a different work hardening effect resulting in a larger scatter of the minimum creep strain rates compared to the L400 specimens, where better repeatability of the creep curves was observed.

Figure 4.4 shows the results of the specimens tested at 20 MPa. Still, the smaller creep strain rates were obtained with smaller specimen sizes. But the creep behavior of the L200 specimens is different compared to the results under other stress conditions, larger fracture strains of the two L200 specimens were observed and the creep strain rates kept decreasing. One specimen had a minimum creep strain rate at a strain of 0.35 and the other

specimen showed continuously decreasing creep strain rate in the  $10^{-8} \text{ s}^{-1}$  range, where the test was interrupted due to the heating wire was broken.

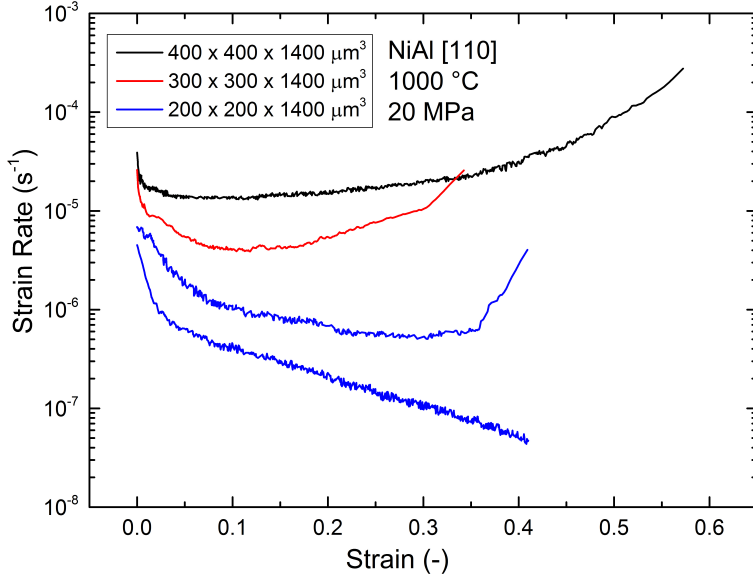


Figure 4.4: Creep curves of NiAl single crystalline miniaturized specimens tested at 1000 °C and 20 MPa in [110] soft orientation

The test results showed that the creep behavior of the miniaturized specimens is very sensitive to the specimen sizes. All the specimens have the same gauge length 1400  $\mu\text{m}$ , while the minimum creep strain rates decreased with reduced specimen's thickness and width from 400  $\mu\text{m}$ , 300  $\mu\text{m}$  to 200  $\mu\text{m}$ . Since all specimens are single crystalline and were tested under the same experimental conditions, there is no influence of the microstructure such as the ratio of grain sizes to specimens sizes in Nimonic 75 polycrystal on the creep behavior, so that the only factor that may influence the creep behavior is the geometric shape of the specimens, i.e., the length-to-width ratio ( $L/W$ ). For the L400 specimen, the  $L/W$  ratio is 3.5, with reduced specimen's thickness and width, the corresponding  $L/W$  ratios are 4.6 for L300

and 7 for L200 specimens. Considering the difference of the  $L/W$  ratios, an additional group of specimens with sizes  $200 \times 200 \times 700 \mu\text{m}^3$  with abbreviated name S200 were tested at the identical experimental conditions to study the influence of the  $L/W$  ratios on creep behavior, since the S200 specimen has the identical  $L/W$  ratio as the L400 specimens and simultaneously, the same thickness and width as the L200 specimens. The creep curves of the L400 and S200 specimens tested at  $1000^\circ\text{C}$  under stress 20MPa, 25 MPa and 30 MPa were shown in Figure 4.5.

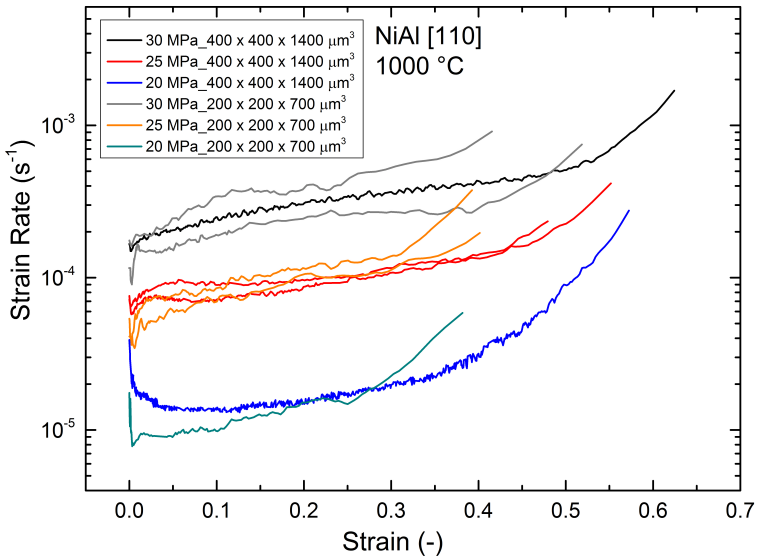


Figure 4.5: Creep curves of the L400 and S200 NiAl miniaturized specimens tested at  $1000^\circ\text{C}$  under stress 20MPa, 25 MPa and 30 MPa.

The creep behavior of the S200 specimens showed similar creep behavior as the L400 specimens under all three stress conditions, which implies the same  $L/W$  ratio of 3.5 may result in the similar creep behavior. For a better overview of the influence of specimen sizes on creep behavior, all the

minimum or steady-state creep strain rates of miniaturized specimens with different sizes were plotted in Figure 4.6 as the Norton plot.

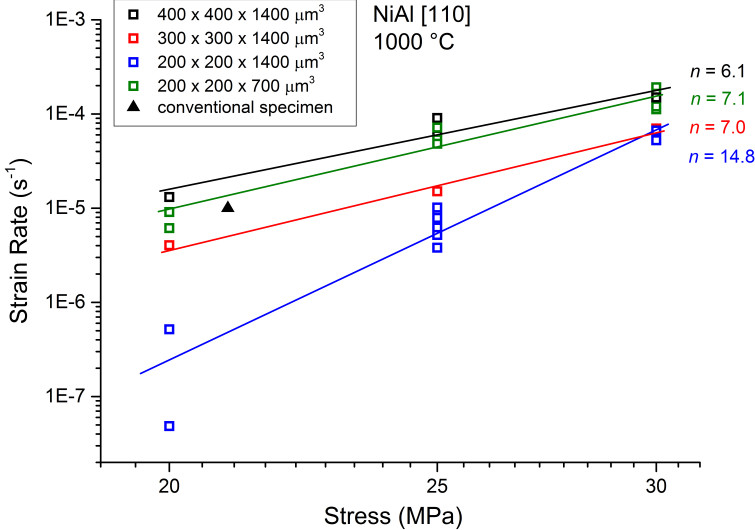


Figure 4.6: Norton-plot of NiAl in [110] soft orientation summarizing minimum/steady-state creep strain rates at 1000 °C with comparison of steady-state creep strain rates of conventional specimens ( $3.81 \times 3.81 \times 7.62 \text{ mm}^3$ ) from the literature [91]

For the miniaturized specimens with the same 1400  $\mu\text{m}$  gauge length, specimens with smaller cross-section showed decreased creep strain rates and increased stress exponents  $n$ . The creep strain rates of the L400 specimens showed a good agreement with the result of conventional specimens, and the corresponding stress exponent  $n=6.1$  is determined, which is similar to the value of the conventional specimens  $n=5.5 \pm 0.5$  [91]. This result suggests the L400 specimens have similar creep behavior as the conventional specimens, which has simultaneously proved the accuracy of the customized setup for micro-tensile creep testing again. For the other two specimen sizes, the corresponding stress exponents are  $n=7.0$  for the L300 and  $n=14.8$  for the L200 specimens, increased stress exponents were detected in specimens

with larger  $L/W$  ratios. With smaller stress, the difference of the creep strain rates is more significant, and an increased scatter of creep strain rates of the L200 specimens was observed. For the S200 specimens, the creep strain rates showed a good agreement with the results of the L400 specimens under all three stress conditions. A stress exponent  $n=7.1$  was determined, which is also similar to the value of the conventional specimens.

From the Norton Plot in Figure 4.6, the main factor resulting in different creep behaviors of the miniaturized specimens is the  $L/W$  ratio. This suggests that the  $L/W$  ratio has a more dominant influence on the creep behaviors of the miniaturized specimens compared to the magnitude of the cross-section, at least for specimens with cross-section equal or larger than  $200 \times 200 \mu\text{m}^2$  in this study.

#### 4.2.2 Fracture surface and slip systems

The fracture and the deformation mechanism of the miniaturized specimens were analyzed to study the influence of different specimen sizes on their creep behavior. Figure 4.7 shows the fracture surfaces of the L400, L300, L200 and S200 specimens tested at  $1000^\circ\text{C}$  and 25 MPa.

All the specimens have similar fracture surfaces regardless of the specimen sizes or the  $L/W$  ratios, similar shear deformations were observed around the necking area along the gauge length. On all specimen surfaces, slip traces with a similar angle to the loading axis were detected suggesting the creep deformation of the miniaturized specimens is related to dislocation glide as the conventional specimens [93] that the creep deformation is dominated by the glide of  $\langle 100 \rangle$  dislocations on  $\{110\}$  and  $\{100\}$  slip planes for NiAl single crystal in [110] soft orientation. The slip traces were compared to the projections of all the possible slip systems on the specimen surface to determine the primary slip systems in the miniaturized specimens. The miniaturized specimens in [110] soft orientation are  $[\bar{1}\bar{1}0]$  oriented in the gauge length and  $[\bar{1}\bar{1}\bar{1}]$  oriented in one specimen surface as shown in Fig-

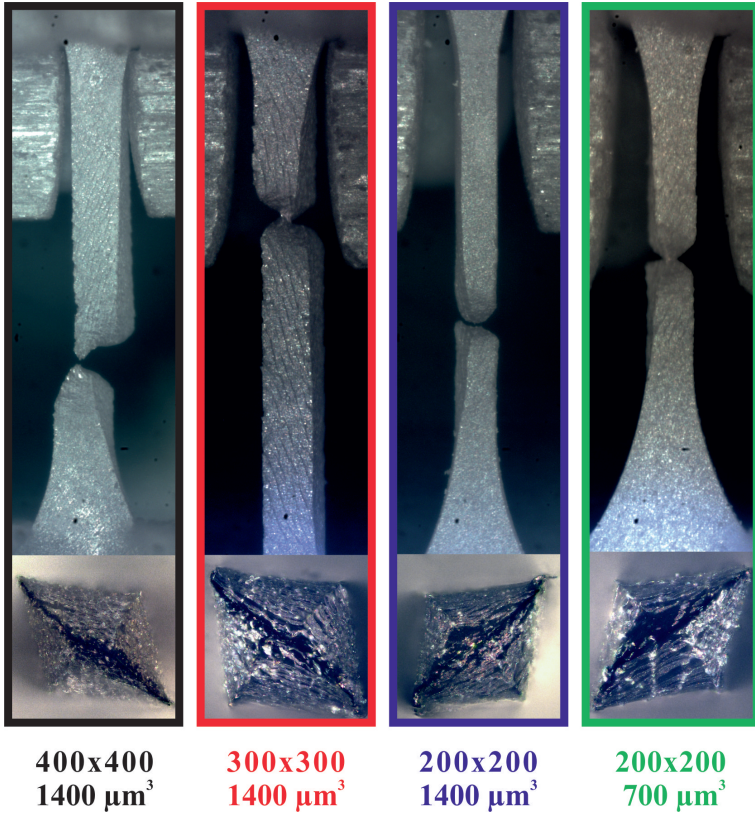


Figure 4.7: Fracture surface of NiAl miniaturized specimens tested in 1000 °C and 25 MPa in [110] soft orientation in sizes of L400, L300, L200 and S200, respectively.

ure 4.8. All angles between the [110] load axis and the projections of the possible  $\{110\}\langle 001\rangle$  and  $\{100\}\langle 010\rangle$  slip systems on  $\{\bar{1}1\bar{1}\}$  plane surface were calculated. These angles were compared with the angle between the slip traces observed on the specimen surfaces and the [110] load axis. Therefore the potential primary slip systems of the miniaturized specimens in [110] soft orientation can be determined. Table 4.1 lists all the results and the corresponding Schmid Factors ( $m$ ).



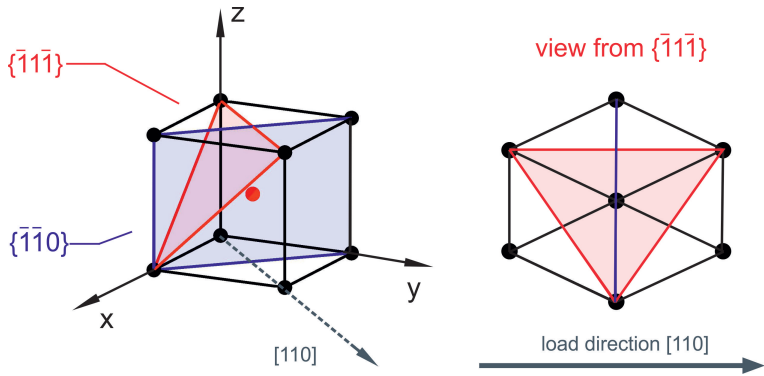


Figure 4.8: Crystal orientation of the NiAl miniaturized specimens in [110] soft orientation

Table 4.1: Angle ( $^{\circ}$ ) between the projection from possible slip systems on  $\{\bar{1}\bar{1}\bar{1}\}$  plane surface and [110] load direction, together with the corresponding schmid factor ( $m$ )

slip system	projection angle ( $^{\circ}$ )	schmid factor ( $m$ )
$\{100\}\langle 010\rangle$	$120^{\circ}$	0.5
$\{010\}\langle 100\rangle$	$60^{\circ}$	0.5
$\{011\}\langle 100\rangle$	$30^{\circ}$	0.35
$\{0\bar{1}1\}\langle 100\rangle$	$60^{\circ}$	0.35
$\{101\}\langle 010\rangle$	$60^{\circ}$	0.35
$\{\bar{1}01\}\langle 010\rangle$	$30^{\circ}$	0.35

To prevent the error of angle measurement from the fractured specimens due to the crystal rotation, one L400 specimen was tested at  $1000^{\circ}\text{C}$  and 25 MPa and interrupted at a strain of 0.1, where the steady-state creep stage was reached. The angle between the slip traces on the  $\{\bar{1}\bar{1}\bar{1}\}$  plane surfaces and the [110] load direction was analyzed with SEM, this angle is about  $30^{\circ}$ , which suggests that the possible slip systems here could be  $\{011\}\langle 100\rangle$  or  $\{\bar{1}01\}\langle 010\rangle$  with identical Schmid Factor 0.35 (see in Figure 4.9). The slip traces on the four specimen surfaces of one miniaturized specimen tested at

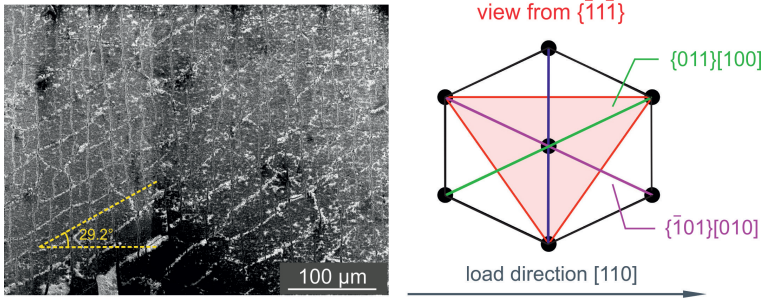


Figure 4.9: Slip traces on one L400 specimen tested at 1000 °C and 25 MPa and interrupted at a strain of 0.1 in comparison with the possible slip systems

1000 °C and 30 MPa were analyzed, the angles between the slip traces on each surface and the [110] load direction were measured and compared with the theoretical angles between the projection of the six slip systems on each specimen surface and the [110] load direction. Table 4.2 lists the results of the projection angles, which were then compared to the slip traces observed from the four specimen surfaces, as shown in Figure 4.10.

Table 4.2: Angle (°) between the projection from possible slip systems on each specimen surface and [110] load direction

slip planes \ angle	surface 1	surface 2	surface 3	surface 4
{011}	30°	90°	150°	90°
{0 $\bar{1}$ 1}	-60°	-31.5°	-120°	-148.5°
{ $\bar{1}$ 01}	-30°	-90°	-150°	-90°
{101}	60°	31.5°	120°	148.5°
{100}	120°	50.8°	60°	129.2°
{010}	60°	129.2°	120°	50.8°

Figure 4.10 shows that the dominating slip plane for the slip trace on each specimen surface is: {011} slip plane for surface 1 with angle 30°, {0 $\bar{1}$ 1}

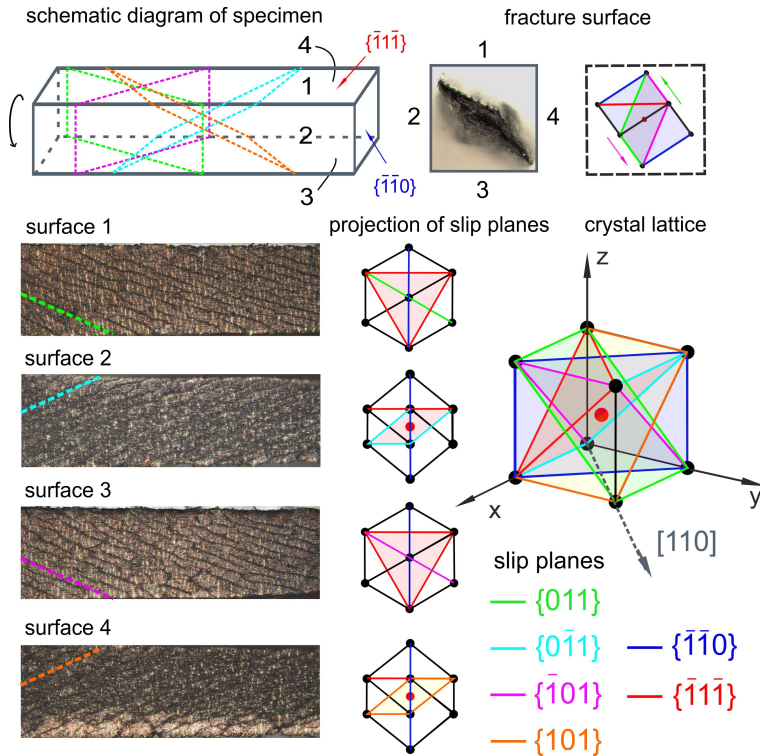


Figure 4.10: Determination of primary slip systems with analysis of slip traces on the four specimen surfaces of one L400 specimen tested at 1000 °C and 30 MPa in [110] soft orientation

slip plane for surface 2 with angle  $-31.48^\circ$ ,  $\{\bar{1}01\}$  slip plane for surface 3 with angle  $-150^\circ$  and  $\{101\}$  slip plane for surface 4 with angle  $148.51^\circ$ . No slip traces caused by  $\{100\}$  and  $\{010\}$  slip planes were detected, the dominating slip planes on all the four surfaces of the miniaturized specimen belong to the  $\{011\}$  slip planes, which indicated that the main slip systems in the NiAl [110] soft orientation are  $\{011\}\langle 100\rangle$ . This result is in good agreement with the work of Forbes et al. [91]; they concluded that creep deformation occurs on the  $\{011\}\langle 100\rangle$  slip systems for all soft orientations,

even though the Schmidt factor for  $\{100\}\langle 010\rangle$  slip systems is larger than the  $\{011\}\langle 100\rangle$  slip systems.

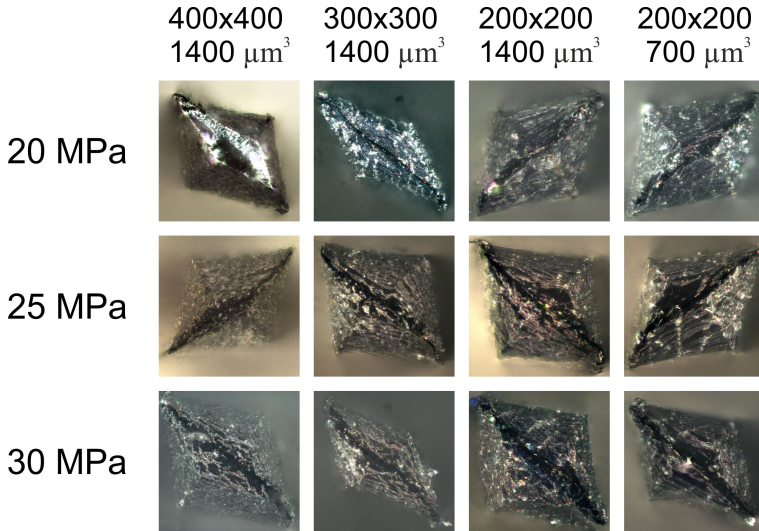


Figure 4.11: Similar fracture surfaces of the miniaturized specimens in tested at stress 20 MPa, 25 MPa and 30 MPa in four different specimen sizes

Additionally, all the fracture surfaces of the miniaturized specimens with different sizes tested at 20 MPa, 25 MPa and 30 MPa were analyzed to study if an influence of initial stress on the fracture mechanism exists, the images of these fracture surfaces are shown in Figure 4.11. It is confirmed once again, that the shape and mechanism of the fracture surfaces are independent on the specimen sizes,  $L/W$  ratios and initial stress in micro-tensile creep tests in this study. All the fracture surfaces are diagonally symmetric and contain the identical shear deformation.

In a short conclusion, the miniaturized specimens in  $[110]$  soft orientation have the identical deformation and fracture mechanism even tested at different experimental conditions, all the miniaturized specimens contained the primary  $\{011\}\langle 100\rangle$  slip systems suggesting the different creep behavior

of the miniaturized specimens should be more related to the influence of the specimen geometries. In the micro-tensile creep testing, both top and bottom adapters for the miniaturized specimens are constrained in one loading axis. The crystal rotation due to the shear deformation caused by the  $\{011\}\langle 100\rangle$  slip systems is expected, which may lead to different local work hardening based on the specimen sizes and  $L/W$  ratios to influence the creep behavior. With the DIC method in this study, the strain distribution on the miniaturized specimen surface can be analyzed at arbitrary strain or time to research the cause of the different creep behavior.

### 4.2.3 Analysis of strain distribution

The strain distributions of the miniaturized specimens tested at 1000 °C and 30 MPa just before fracture in four different specimen sizes were analyzed with the DIC method, which are shown in Figure 4.12 for L400, Figure 4.13 for L300, Figure 4.14 for L200 and Figure 4.15 for S200 specimens, respectively. In each Figure, the following elements were analyzed:

1. The strain distributions with direction parallel to loading direction ( $\epsilon_y$ )
2. The strain distribution with direction perpendicular to the loading direction ( $\epsilon_x$ )
3. The shear strain distribution ( $\epsilon_{xy}$ )

The strain distributions in  $\epsilon_y$  of all four specimens before fracture are similar: Inhomogeneous strain distributions along the gauge length were observed. Strain localization around necking area was detected, where fracture occurred. Both ends of the miniaturized specimens have less strain compared to the global strain. The strain distributions in  $\epsilon_x$  of all four specimens are also similar: Strong strain localization could only be observed at the necking area, while the remaining area of the gauge length showed similar strain distribution. However, the shear strain distributions ( $\epsilon_{xy}$ ) showed

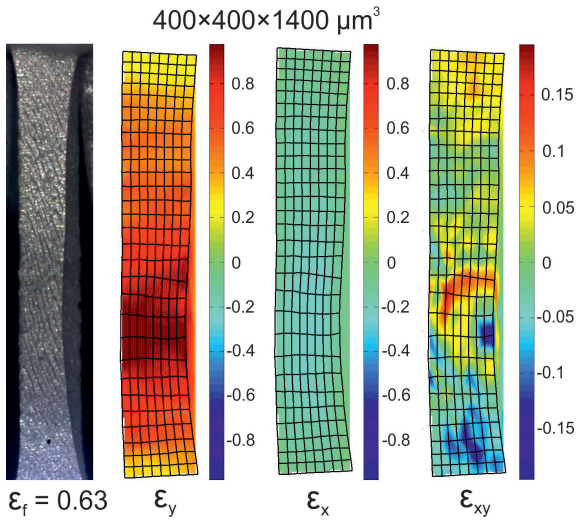


Figure 4.12: Strain distribution analysis of one L400 specimen tested at 1000 °C and 30 MPa before fracture

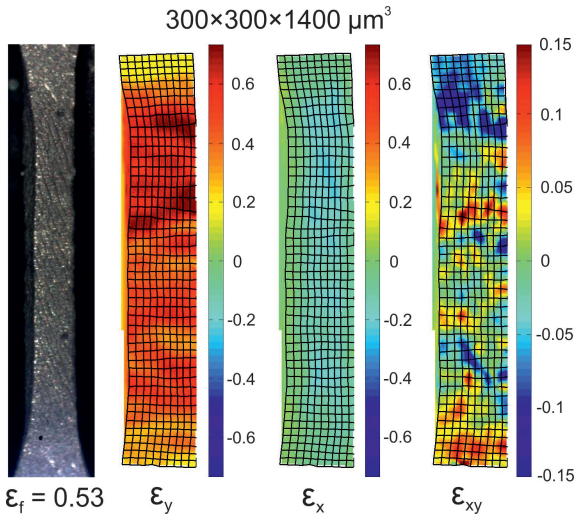


Figure 4.13: Strain distribution analysis of one L300 specimen tested at 1000 °C and 30 MPa before fracture

different results. First, the strain distribution of specimens with the identical gauge length 1400  $\mu\text{m}$  and different thickness will be analyzed:

For the L400 specimen, positive and negative shear strain localizations were observed at the two constrained specimen ends, where dislocation glides were restricted. Around the necking area, i.e., the potential fracture area, another shear strain localization was detected. The remaining area in the gauge length of the L400 specimen showed a continuous shear strain distribution and grid deformation.

For the L300 specimen, the shear strain distribution is similar to the L400 specimen in that positive and negative shear strain localizations were observed at the two constrained specimen ends, another shear strain localization was located in the necking area. But the remaining area in the gauge length of the L300 specimen contained a more inhomogeneous shear strain distribution; a slight shear strain localization was observed close to the bottom specimen end, where larger deformation of the grids can be detected indicating multiple necking areas along the gauge length.

For the L200 specimens, similar positive and negative shear strain localization can be observed at both specimen ends as for the other two specimens. However, an apparent pair of positive and negative shear strain localization was detected at the necking area, where a strong shear deformation of the grids was also determined. The L200 showed a totally different shear strain distribution compared to the other two specimens.

The three specimens have the same gauge length, and their  $L/W$  ratios are increased with reduced thickness. The L200 specimen with the largest  $L/W$  ratio 7 has more evident and multiple shear strain localizations compared to the L400 specimen with the  $L/W$  ratio 3.5. Figure 4.15 shows the shear strain distribution of the S200 specimen with the  $L/W$  ratio 3.5, which is similar to the L400 specimen. This phenomenon indicates the different shear strain distributions based on different  $L/W$  ratios are possibly the key factor that influences the creep behavior of the miniaturized specimen. For

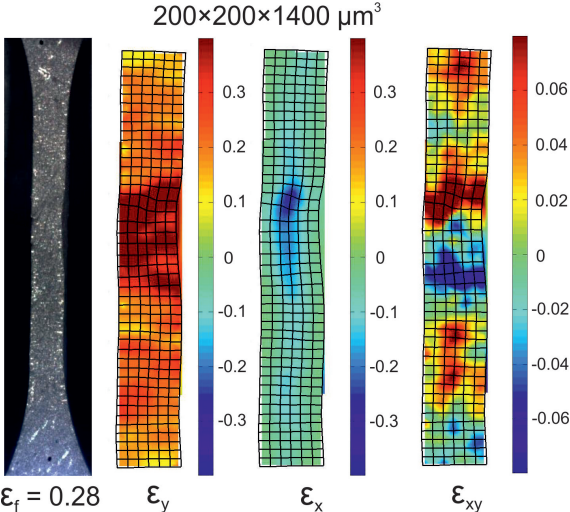


Figure 4.14: Strain distribution analysis of one L200 specimen tested at 1000 °C and 30 MPa before fracture

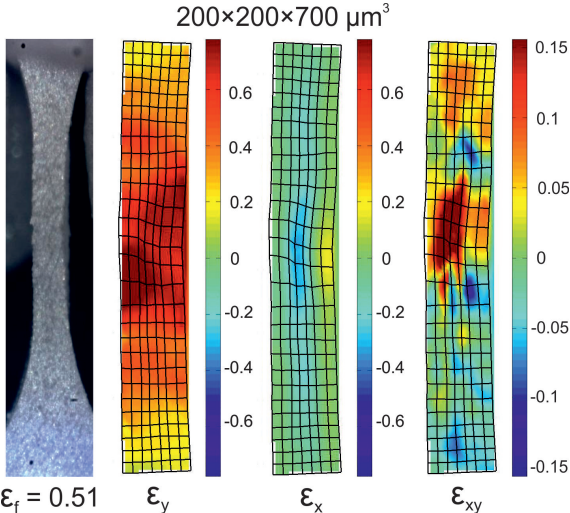


Figure 4.15: Strain distribution analysis of one S200 specimen tested at 1000 °C and 30 MPa before fracture



more detailed and quantitative research, the strain distributions of the four specimens were analyzed at a strain of 0.1, where all the four specimens have the minimum or steady-state creep strain rates. The results were plotted in Figure 4.16 for L400, Figure 4.17 for L300, Figure 4.18 for L200 and Figure 4.19 for S200 specimens, respectively.

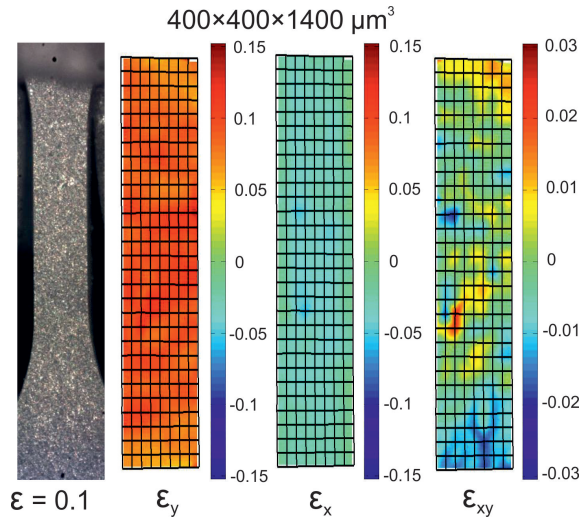


Figure 4.16: Strain distribution analysis of one L400 specimen tested at 1000 °C and 30 MPa and interrupted at a strain of 0.1

The strain distributions in  $\epsilon_y$  and  $\epsilon_x$  in all the specimens are similar, even though some areas with slight strain localization can be observed, but the overall strain distributions along the gauge length are homogeneous. The shear strain distributions are again sensitive to the  $L/W$  ratios of the specimens. For specimens with the same 1400  $\mu\text{m}$  gauge length, enhanced shear strain localization is observed with reduced specimen thickness. The L200 specimen showed an extra pair of shear strain localization again even at a strain of 0.1, where the specimen reached the minimum creep strain rate.

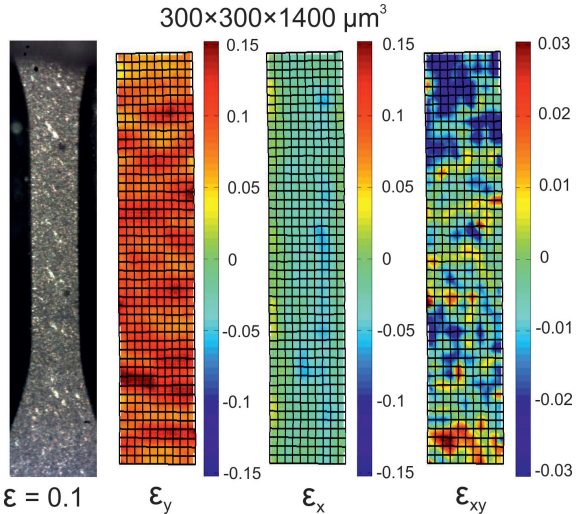


Figure 4.17: Strain distribution analysis of one L300 specimen tested at 1000 °C and 30 MPa and interrupted at a strain of 0.1

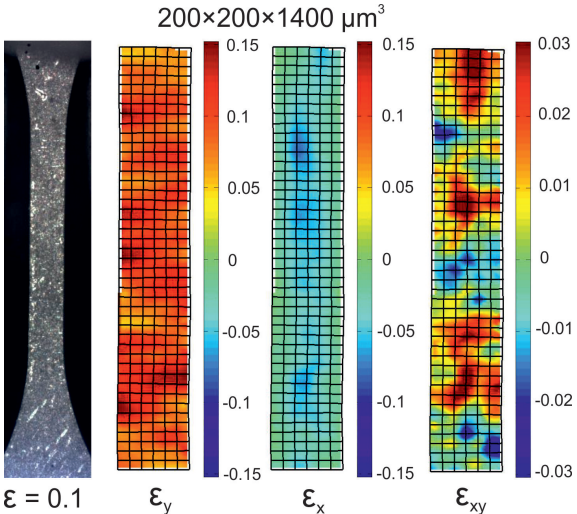


Figure 4.18: Strain distribution analysis of one L200 specimen tested 1000 °C and 30 MPa and interrupted at a strain of 0.1

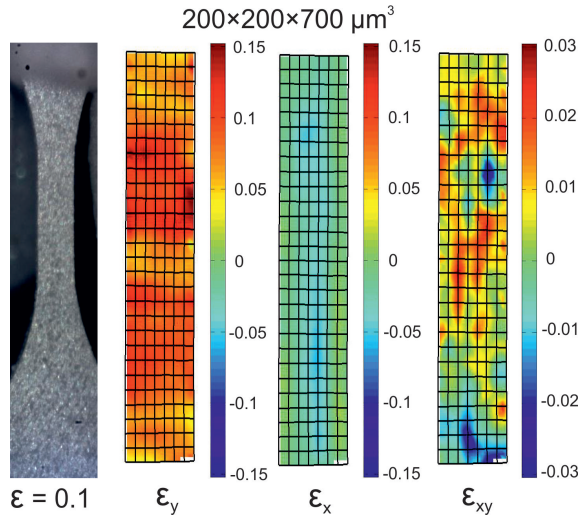


Figure 4.19: Strain distribution analysis of one S200 specimen tested 1000 °C and 30 MPa and interrupted at a strain of 0.1

Meanwhile, the S200 specimen exhibits a shear strain distribution similar to the L400 specimen, since both specimens have the same  $L/W$  ratios.

In a short conclusion, the analysis of strain distribution of the four miniaturized specimens showed inhomogeneous strain distribution in  $\epsilon_y$  and an evident difference in the shear strain distribution, which were already observed at a strain of 0.1, where the miniaturized specimens were in steady-state or minimum creep stage. Therefore two influencing factors, which may be responsible to the different creep behaviors of the miniaturized specimens, will be discussed in the following sections: first is the stress error caused by the strain localization and oxidation on the miniaturized specimens under constant stress testing condition, second is the different shear strain distribution based on different  $L/W$  ratios.

#### 4.2.4 Influence of stress localization

The miniaturized specimens were tested under constant stress so that the corresponding load on the specimens was adjusted according to the measured global strain to maintain constant stress by assuming the volume of the specimen is constant during the test. The strain distribution was inhomogeneous in the gauge length resulting in uneven stress distribution. Increased stress occurred at the strain localization area, and oppositely, the stress in the remaining gauge length area may be smaller than the initial stress. This different stress distribution in the gauge length results in different creep strain rates, which influence the global creep strain rate. The strain vs. strain rate curves of one L200 and one L400 specimen tested at 1000 °C and 30 MPa are displayed in Figure 4.20. For the L200 specimen, a new strain vs. strain

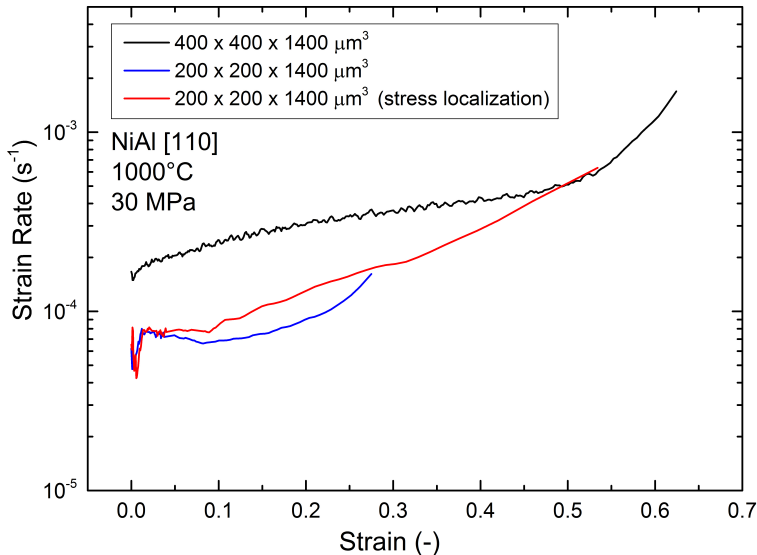


Figure 4.20: Creep curves of one L200 specimen analyzed with the DIC method in strain localization area (red curve) and the whole gauge length area (blue curve) in comparison with one L400 specimen tested at 1000 °C and 30 MPa.

rate curve (red curve) was analyzed with the DIC method by selecting only the strain localization area. The new creep curve (red curve) showed an increased creep strain rate compared to the original curve (blue curve), but the increment of the creep strain rate is still negligible compared to the creep strain rate of the L400 specimen. The minimum creep strain rate of the new creep curve (red curve) is still smaller than the one of the L400 specimen at a global strain of 0.02. With increased strain, the creep strain rate of the red curve is approaching the L400 specimen, which is due to the necking in the miniaturized specimen resulting in increased stress. Still, the strain localization can not explain the different creep behavior of the miniaturized specimens with different specimen sizes and  $L/W$  ratios.

#### 4.2.5 Influence of oxidation

The influence of the surface oxidation on the creep behavior has to be considered due to the miniaturized specimen sizes. Figure 4.21 shows the oxidized surface of one L400 specimen tested at 1000 °C and 25 MPa until fracture, the image was taken from the area away from the fracture surface. From the specimen surface, two features of the oxide layer can be detected: First is the slip traces, which have the 30 ° angle to the load direction, these slip traces are caused by the glide of  $\langle 100 \rangle$  dislocations on  $\{011\}$  slip planes. Second are the cracks on the oxide layer, which are caused by the elongation of the miniaturized specimens. Hence the cracks are vertical to the load direction.

Cross-Sections close to the specimen surface were made by FIB cutting in one L200 and L400 specimen to measure the oxide layer thickness. Both specimens were tested at 1000 °C and 25 MPa until fracture. Figure 4.22 (a) shows one cross-section of the L200 specimen, which is vertical to the load direction and contains one slip trace. The magnified image of the cross-section is shown in Figure 4.22 (b), where a dense oxide layer on the specimen surface was observed, and the maximum thickness of the oxide layer

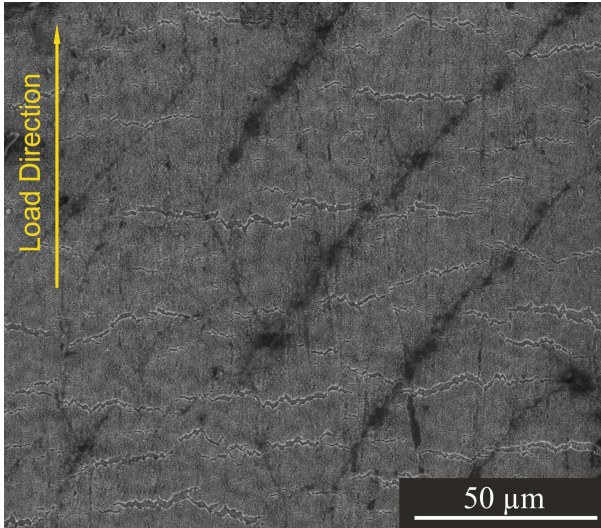


Figure 4.21: The oxidized surface of one L400 specimen tested at 1000 °C and 25 MPa until fracture

was under 800 nm so that the stress error caused by the oxide layer is under 1.6 %. For the L400 specimen (see Figure 4.22 (c) and (d) ), another cross-section was analyzed around the slip traces. The oxide layer thickness was also under 800 nm resulting in a corresponding stress error under 1%. But both specimens have cracks in the slip traces and the length of these cracks was longer than 5 μm. There exists no evident difference in the thickness and structure of the oxide layer in the L200 and L400 specimens after fracture.

One additional L400 specimen was tested at 1000 °C and 25 MPa and interrupted at a strain of 0.1, where the specimen was in the steady-state creep stage. Figure 4.23 (a) shows the surface in the middle of the miniaturized specimen, slip traces with a 30 ° angle to the load direction and the cracks of oxide layer due to the elongation of the miniaturized specimens were again observed. A cross-section containing one oxide layer crack and one slip

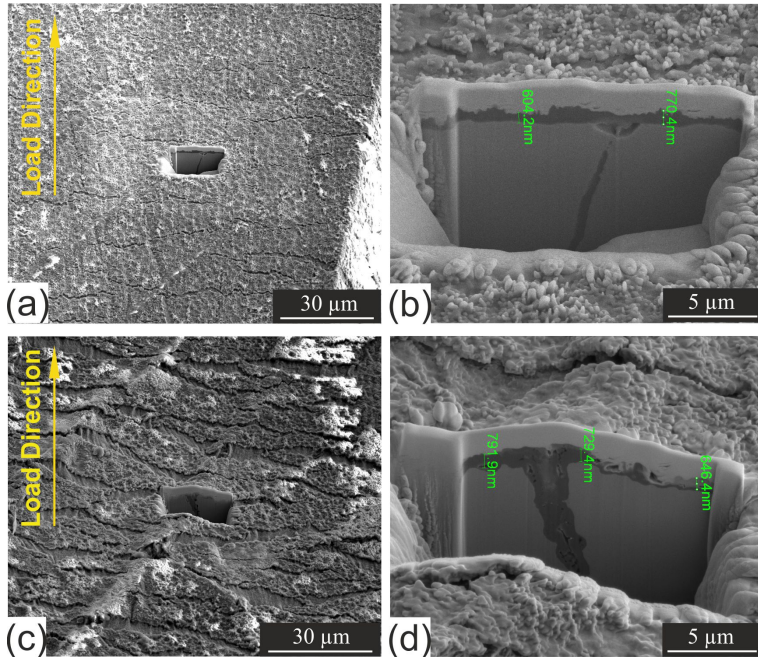


Figure 4.22: The oxide layer thickness of one L200 specimen (a, b) and one L400 specimen (c, d) tested at 1000 °C and 25 MPa until fracture, the maximum oxide layer thickness in both specimens is under 800 nm.

trace was cut (see Figure 4.23 (b)) parallel to the load direction. Figure 4.23 (c) and (d) show the magnified image of the cross-section: Figure 4.23 (c) shows that the thickness of the oxide layer is around 500 nm, hence the corresponding stress error to the L400 specimen can be ignored, and the specimen elongation simply causes the crack of the oxide layer without extra damage into the metallic material. The formation of a new oxide layer was observed at the crack of the oxide layer. Figure 4.23 (d) shows the right part of the cross-section, one crack was generated from the slip trace with length over 5  $\mu\text{m}$  and oxidation was observed along the crack. This crack should lead to a strong stress localization in the miniaturized specimens. For

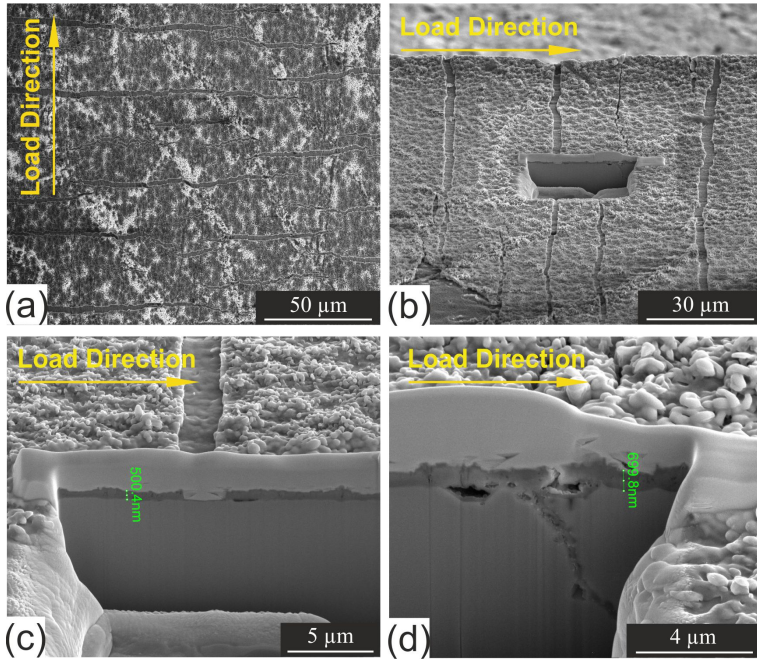


Figure 4.23: The oxide layer thickness of one L400 specimen tested at 1000 °C and 25 MPa, stopped at a strain of 0.1: (a) slip traces with 30 ° to the load direction and cracks of the oxide layer due to specimen elongation, (b,c,d) analysis of one cross-section along the load direction with oxide layer thickness under 700 nm and one crack detected along the slip trace.

the L200 specimen with a smaller cross-section compared to the L400 specimens, increased creep strain rates should be observed due to such cracks. However, the creep strain rates of the L200 specimens were always smaller compared to the L400 specimens under identical experimental conditions. By contrast, the S200 specimens, which contain the same cross-section as the L200 specimens, showed the similar creep behavior as the L400 specimens, which suggests that the oxide layer and the cracks in the slip traces have a negligible influence on the creep behavior of the miniaturized specimens with different sizes.



### 4.2.6 Geometrically Necessary Dislocations (GND) determination with EBSD

In descriptions of dislocations in crystals, dislocations can be separated into two different categories, the Geometrically Necessary Dislocations (GND), which accommodate a lattice curvature from a deformation gradient, and the Statistically Stored Dislocations (SSD), which accumulate due to statistical entanglements. The framework of GND was first introduced by Nye [59] and further detailed by Ashby [114] and Fleck et al. [43]. A simplest possible dimensionally correct relationship between the flow stress  $\tau$  and the total dislocation density can be given by a Taylor-type relation:

$$\tau \approx \alpha \cdot G \cdot b \cdot \sqrt{\rho_G + \rho_S} \quad (4.1)$$

Where  $\alpha$  is a constant coefficient taken to be around 0.3 by Ashby [114],  $G$  is the shear modulus,  $b$  is the magnitude of the Burger's vector,  $\rho_G$  is the GND density and  $\rho_S$  is the SSD density. At the initial stage of creep testing, the condition  $\rho_G \gg \rho_S$  can be assumed since there are few SSDs generated before the work hardening process so that the flow stress  $\tau$  can be approximated as:

$$\tau \approx \alpha \cdot G \cdot b \cdot \sqrt{\rho_G} \quad (4.2)$$

Where only the contribution of the GNDs is included in the flow stress. In the creep test, the flow stress is one key parameter that influences the creep strain rate. Therefore the corresponding GND density is one non-negligible factor. Several experiments such as micro-torsion [43], micro-bending [115] and micro-indentation hardness tests [116–118] have proven the GNDs have increased influence on the mechanical properties of specimens with reduced sizes in micrometer scale, i.e., the smaller the size, the harder the material. In our case, different shear strain distributions were observed in the miniaturized specimens with different  $L/W$  ratios with the

DIC method. The inhomogeneous deformation caused by the shear strain results in strain gradients in the miniaturized specimens, which require corresponding GNDs for the shear deformation. Hence, it may be expected that the GND density or distribution is influenced by the different  $L/W$  ratios of the miniaturized specimens resulting in the observed different creep behavior. The GND density can be calculated based on the work of Kubin et.al [53] and the strain gradient model by Gao [51] as:

$$\rho_G = \frac{2\kappa}{b} \quad (4.3)$$

Where  $\kappa$  is the curvature calculated from the plastic shear strain gradient,  $b$  is the magnitude of the Burger's vector. With the EBSD measurement, the variation of the crystal orientation of the miniaturized specimens due to the creep deformation can be detected. Hence, the equation can be reconstructed as:

$$\rho_G = \frac{2\theta}{u \cdot b} \quad (4.4)$$

Where  $\theta$  is the Kernel Average Misorientation (KAM) and  $u$  is the step size defined by the EBSD measurement. For the analysis of the EBSD data and calculation of the GND density, an open-source Matlab toolbox MTEX is used [119].

One L200 and one L400 specimen tested at 1000 °C and 25 MPa were interrupted at a strain of 0.1, then the specimens were mechanically polished (ATM SAPHIR 520) until a surface roughness of 0.1  $\mu\text{m}$  for the EBSD analysis. The misorientation and GND distribution were analyzed and compared with the shear strain distribution calculated with the DIC method. The results are shown in Figure 4.24 and Figure 4.25.

Figure 4.24 shows the analysis results of the L400 specimen, the Inverse Pole Figure (IPF) shows that the crystal orientation along the specimen gauge length is [011] and vertical to the polished specimen surface is [111],

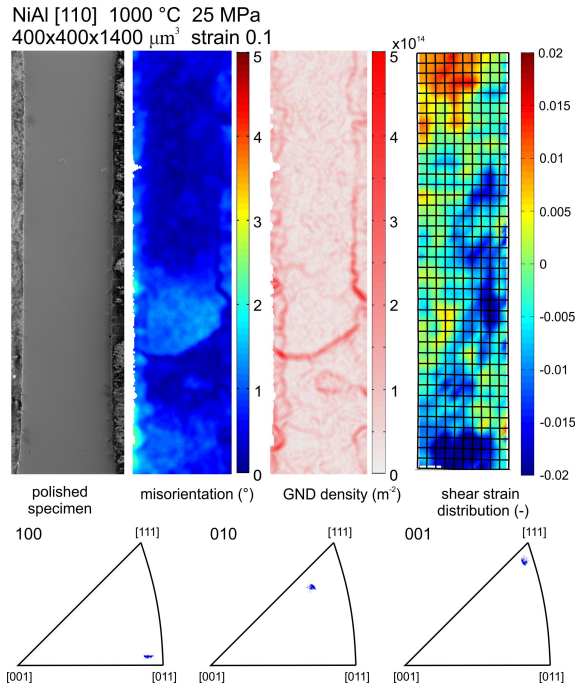


Figure 4.24: Misorientation and GND distribution with EBSD in comparison with the strain distribution with the DIC method in one L400 specimen tested at 1000 °C and 25 MPa interrupted at a strain of 0.1

which is in good agreement with the designated orientation by specimen manufacture as shown in Figure 4.1. The small offset in the measured orientation was caused by two possible factors: First, during the mechanical polishing, the specimen surface may have been slightly tilted. Second, by specimen mounting for EBSD measurement, the specimen surface was not perfectly vertical to the EBSD detector. But this offset has negligible effects to the test results because the most important information related to the microstructural changes are the misorientation and the corresponding calculated GND density, which are insensitive to the orientation offset. For the L400 specimen, few GNDs were observed on the specimen surface and

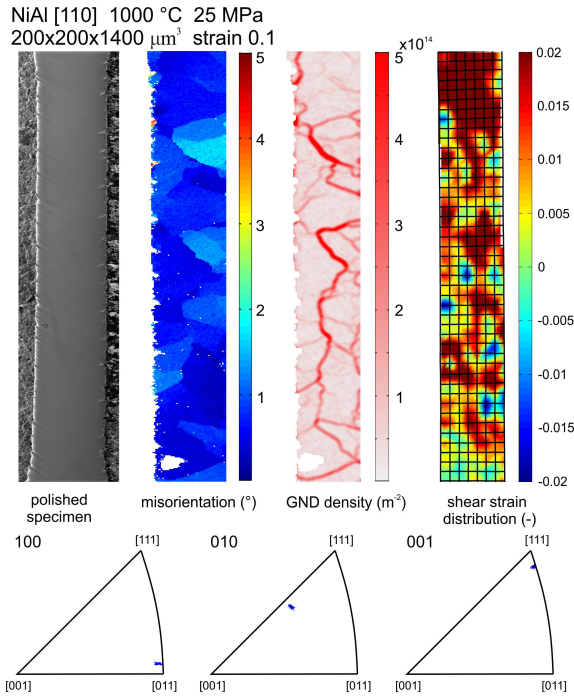


Figure 4.25: Misorientation and GND distribution with EBSD in comparison with the strain distribution with the DIC method in one L200 specimen tested at 1000 °C and 25 MPa interrupted at a strain of 0.1

the shear strain calculated by the DIC method was evenly distributed. Compared to the results of the L200 specimen shown in Figure 4.25, increased misorientation and denser GND distribution were detected, the shear strain distribution correspondingly revealed stronger localization. The increased GND density suggests more obstacles for the dislocation glide and results in a reduced creep strain rate of the L200 specimens as compared to the L400 specimens.

For a more detailed understanding of the influence of the specimen  $L/W$  ratios on the GND density, another pair of L400 and L200 specimens were

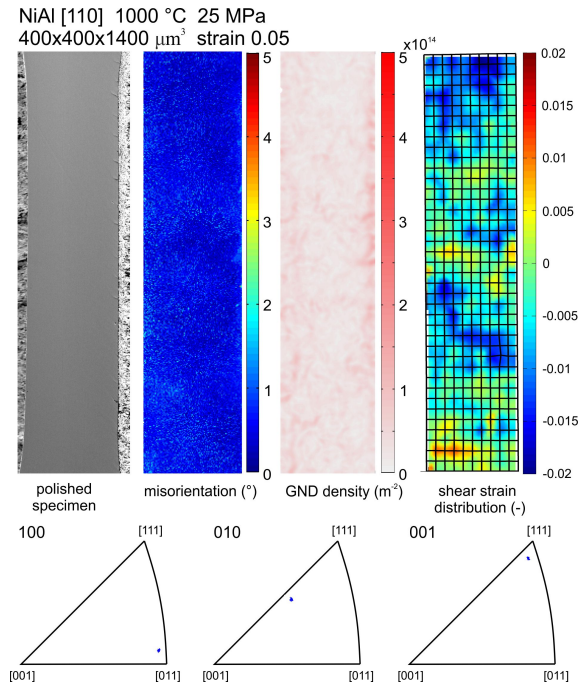


Figure 4.26: Misorientation and GND distribution with EBSD in comparison with the strain distribution with the DIC method in one L400 specimen tested at 1000 °C and 25 MPa interrupted at a strain of 0.05

tested at 1000 °C and 25 MPa, this time both specimens were interrupted at a strain of 0.05 for the EBSD analysis. Figure 4.26 shows the analysis results of the L400 specimen interrupted at a strain of 0.05. Almost no GND and misorientation was observed compared to the L400 specimen interrupted at a strain of 0.1. The L200 specimen showed an identical tendency in that the reduced GND density at a strain of 0.05 was observed as shown in Figure 4.27. But the L200 specimens contained a denser GND distribution and a larger GND density than the L400 specimens at both strain of 0.05 and 0.1. This phenomenon indicated the GND distribution and density are

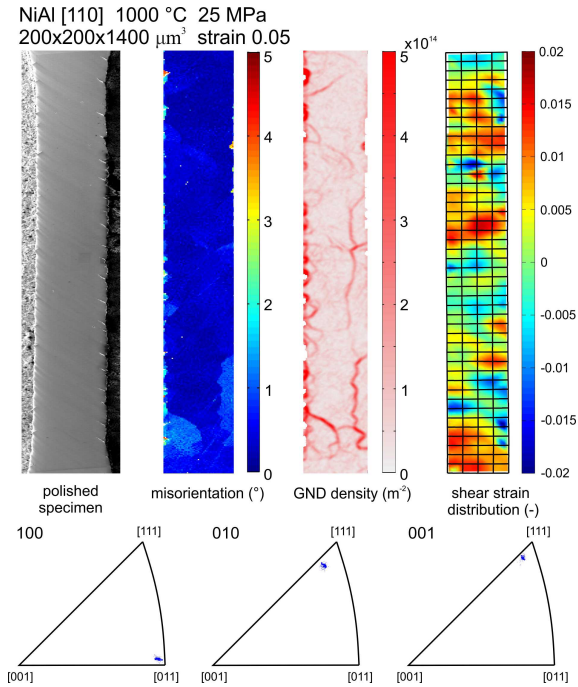


Figure 4.27: Misorientation and GND distribution with EBSD in comparison with the strain distribution with the DIC method in one L200 specimen tested at 1000 °C and 25 MPa interrupted at a strain of 0.05

strongly influenced by the specimen  $L/W$  ratios, even at the very early stage in the creep tests.

One S200 and one L200 specimen tested at 1000 °C and 20 MPa interrupted at the steady-state creep stage were then compared for a more detailed study of the GND distribution under smaller initial stress and larger strain. Figure 4.28 shows the result of the L200 specimen at a strain of 0.43 and Figure 4.29 shows the result of the S200 at a strain of 0.27. The GND distribution showed again the dependence on the specimen  $L/W$  ratios, a higher density of GND was observed at the specimen with larger  $L/W$  ratios, here

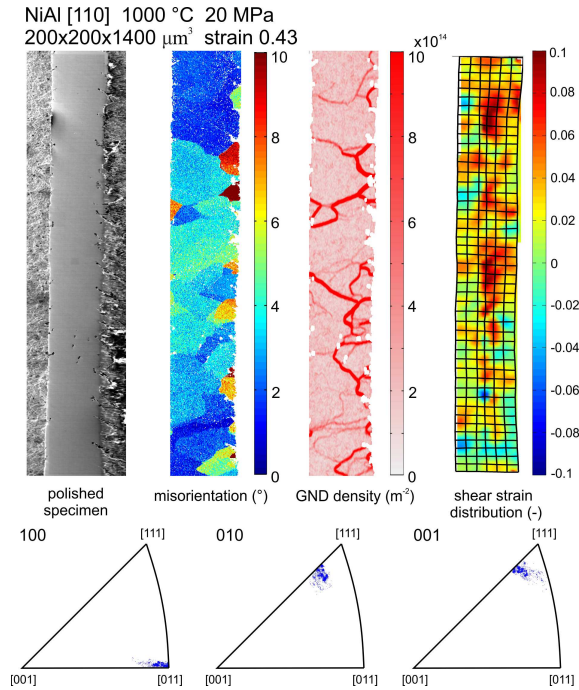


Figure 4.28: Misorientation and GND distribution with EBSD in comparison with the strain distribution with the DIC method in one L200 specimens tested at 1000 °C and 20 MPa interrupted at a strain of 0.43

the L200 specimen. A significantly higher variation in the IPF was observed in both specimens because the tensile axis in the customized setup is constrained such that the larger strains in these two specimens lead to increased crystal misorientations.

The GND densities in all the specimens were listed in table 4.3 and plotted as a bar chart in Figure 4.30. For the specimens tested at 25 MPa, the GND density showed a dependence on the  $L/W$  ratios of the miniaturized specimens, the L200 specimens always contained larger GND density than the L400 specimens, but the difference of the GND density between these

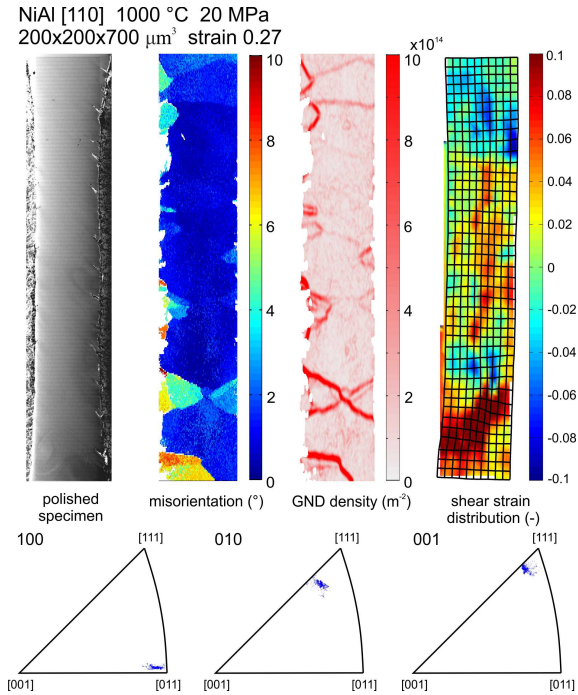


Figure 4.29: Misorientation and GND distribution with EBSD in comparison with the strain distribution with the DIC method in one S200 specimens tested at 1000 °C and 20 MPa interrupted at a strain of 0.27

two types of specimens is reduced with increased strain from 0.05 to 0.1, where both specimens were in the steady-state/min creep stage. It is also noteworthy that the GND densities of the L200 specimens are similar at strains of 0.05 and 0.1. All these results indicate that the GNDs were already generated at the initial stage of creep testing. These GNDs were probably caused by plastic deformation due to the constrained experimental condition or even a possible setup misalignment. A minimum GND density is therefore required for this plastic deformation, and the magnitude of the GND density may be sensitive to the  $L/W$  ratios of the miniaturized specimens.



Table 4.3: GND density of the miniaturized specimens calculated from the EBSD measurement.

GND density ( $m^{-2}$ )	mean	median	min	max
20 MPa S200 ( $\epsilon = 0.27$ )	$1.88 \times 10^{14}$	$1.19 \times 10^{14}$	$2.40 \times 10^{13}$	$2.20 \times 10^{15}$
20 MPa L200 ( $\epsilon = 0.43$ )	$3.15 \times 10^{14}$	$2.07 \times 10^{14}$	$3.13 \times 10^{13}$	$4.26 \times 10^{15}$
25 MPa L400 ( $\epsilon = 0.05$ )	$3.37 \times 10^{13}$	$3.05 \times 10^{13}$	$4.47 \times 10^{12}$	$1.73 \times 10^{14}$
25 MPa L200 ( $\epsilon = 0.05$ )	$8.38 \times 10^{13}$	$5.57 \times 10^{13}$	$1.43 \times 10^{13}$	$1.15 \times 10^{15}$
25 MPa L400 ( $\epsilon = 0.10$ )	$6.85 \times 10^{13}$	$5.43 \times 10^{13}$	$1.08 \times 10^{13}$	$4.25 \times 10^{14}$
25 MPa L200 ( $\epsilon = 0.10$ )	$9.03 \times 10^{13}$	$5.38 \times 10^{13}$	$1.14 \times 10^{13}$	$7.84 \times 10^{14}$

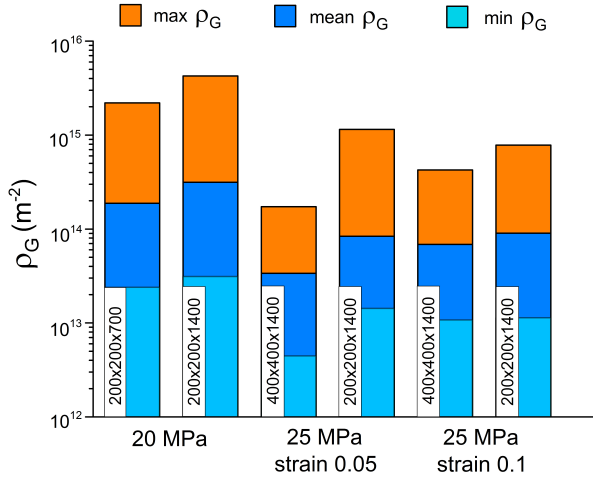


Figure 4.30: GND density of the miniaturized specimens calculated from the EBSD measurement plotted in bar diagram

These initial generated GNDs are obstacles for the dislocation glides resulting in increased SSD density, which leads to a reduced creep strain rate. With larger strain, the GND formation is more related to the creep deformation, where the specimen sizes have less influence. Since all the miniaturized specimens showed the identical plastic deformation mechanism, the magnitude of the GND density in different specimen types is possibly only

related to the global strain. This is exemplified with the specimens tested at 20 MPa; both specimens have reached steady-state creep stage, and the L200 specimen contained a higher GND density at a strain of 0.43 than the S200 specimen at a strain of 0.27. The specimens tested at 20 MPa also have larger GND density than the specimens tested at 25 MPa interrupted at a strain of 0.1 due to larger global strain.

According to the analysis of GNDs in the miniaturized specimens, the most important discovery is that a significant difference of the GND density was detected at the initial stage of creep testing: Increased GND density existed in the specimens with larger  $L/W$  ratios. The source of the GNDs generated at the beginning of the micro-tensile creep tests and its relationship with the specimen geometry need to be determined.

#### 4.2.7 Influence of GNDs on creep behavior

In order to determine the source of the GNDs generated at the beginning of the micro-tensile creep tests, the point positions in the gauge length of one L400 specimen tested at 1000 °C and 25 MPa were analyzed with the DIC method from the test beginning to a strain of 0.005 as shown in Figure 4.31. Each red point in the gauge length area (see Figure 4.31 (a)) contains the position information in the y-direction, which is along the gauge length, and the vertical x-direction. We have converted the 2D position information on the specimen surface into 1D information by calculating the mean positions in x- and y-direction in each row along the gauge length. Figure 4.31 (b) shows the results of the 1D position information with strain increasing from 0.001 to 0.005. With increasing strain, an increasing misalignment of the position line in the x-direction is observed. Figure 4.31 (c) shows the misalignment in the x-direction (vertical to load direction) in comparison with the gauge length in the y-direction (parallel to load direction). The increasing misalignment at a strain of 0.005 results in a misalignment angle around 0.16 °. For the L400 specimen tested at 25 MPa, the initial load on the

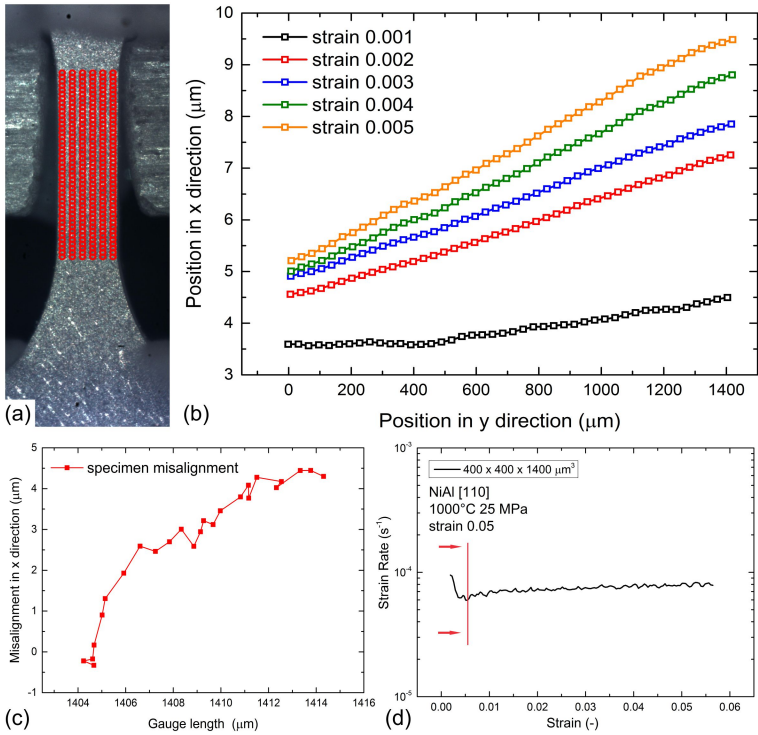


Figure 4.31: Analysis of the specimen misalignment in one L400 specimen tested at 1000 °C and 25 MPa: (a) analysis area in the gauge length, (b) 1D converted point position information with strain from 0.001 to 0.005, (c) the misalignment curve from the test beginning to a strain of 0.005 and (d) creep curve of the miniaturized specimen

specimen is around 4~4.5 N, which is dependent on the actual specimen cross-section after mechanical polishing. This misalignment could cause a bending load of around 0.011~0.013 N in the x-direction, which results in a load error below 0.3%. Even though the load error is negligible, considering the miniaturized specimen size, the detailed influence of this load error on the creep behavior will be analyzed.

The influence of the misalignment can be analyzed with a simplified cantilever model based on the following preconditions: The setup misalignment causes a bending load at the initial stage of creep test; The initial stress on the specimen is smaller than the yield stress in creep tests so that the mechanical analysis of the whole miniaturized specimen is in the elastic range; The bending load caused by the misalignment of the setup is assumed to be mainly located at the bottom area of the miniaturized specimen. A schematic diagram for this simplified cantilever model is shown in Figure 4.32.

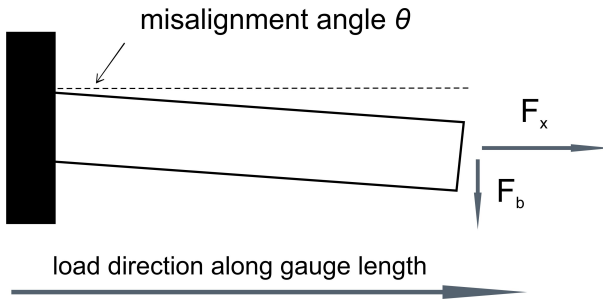


Figure 4.32: The schematic diagram for the simplified cantilever model, a bending load  $F_b$  was caused by the misalignment angle  $\theta$ .

$F_x$  is the load on the miniaturized specimen with the direction along the gauge length, which is set as initial stress for the micro-tensile creep test.  $F_b$  is the bending load caused by the misalignment angle  $\theta$ , which is vertical to the load direction  $F_x$ . The cantilever represents the gauge length area of the specimen so that it has a cuboid geometry with length  $L_0$  in the values of 700  $\mu\text{m}$  and 1400  $\mu\text{m}$  equal to the gauge lengths, the thickness and width are equal to 200  $\mu\text{m}$  and 400  $\mu\text{m}$ , respectively. The left side of the cantilever is considered as the top part of the specimen, which is fixed, the right side represents the bottom part of the specimen, which is in contact with the lower adapter and the shifter, where the bending load acts. With the simpli-

fied cantilever model, the curvature  $\kappa$  caused by the bending load  $F_b$  can be calculated as [120]:

$$\kappa = \frac{M}{E \cdot I} \quad (4.5)$$

Where  $E$  is the Young's modulus,  $M$  is the bending moment and  $I$  is the moment of inertia, which are calculated as:

$$\begin{aligned} M_{max} &= F_b \cdot L = \sigma_x \cdot w \cdot h \cdot \tan(\theta) \cdot L \\ I &= \frac{w \cdot h^3}{12} \end{aligned} \quad (4.6)$$

Where  $\sigma_x$  is the initial stress on the miniaturized specimens,  $\theta$  is the misaligned angle,  $w$  is the specimen width and  $h$  is the specimen thickness. The maximum curvature and GND density can be calculated as:

$$\begin{aligned} \kappa &= 12 \cdot \tan(\theta) \cdot \frac{\sigma_x}{E} \cdot \frac{L}{h^2} \\ \rho_G &= 24 \cdot \tan(\theta) \cdot \frac{\sigma_x}{E \cdot b} \cdot \frac{L}{h^2} \end{aligned} \quad (4.7)$$

Based on this equation, the GND density  $\rho_G$  is related to  $L/h^2$  ratios of the miniaturized specimens. Therefore the GND density of the L200 specimens is two times higher than the S200 specimens and four times as much as those of the L400 specimens at the same experimental conditions. The magnitude of the GND density calculated from the cantilever model is dependent on not only the specimen length to width ( $L/W$ ) ratio but also on the absolute magnitude of the specimens' thickness. Compared to the conventional specimens with similar geometry, the curvature of the miniaturized specimens due to the reduced thickness or width is larger under the same bending effect so that a correspondingly increased GND density is expected. From the EBSD analysis in the previous section, the difference of GND density in specimens with different  $L/W$  ratios was already observed at the early

stage of the creep tests resulting in different creep strain rates. Additionally, the equation 4.7 based on the simplified cantilever model showed the relationship between the GND density and the specimen geometry, in particular the  $L/h^2$  ratio. Based on these two aspects, a correlation between the creep strain rate and the specimen geometry ( $L/h^2$ ) is expected. A diagram of the steady-state/min creep strain rates  $\dot{\epsilon}$  vs.  $L/h^2$  ratios is plotted in Figure 4.33 to verify the correlation between the two parameters.

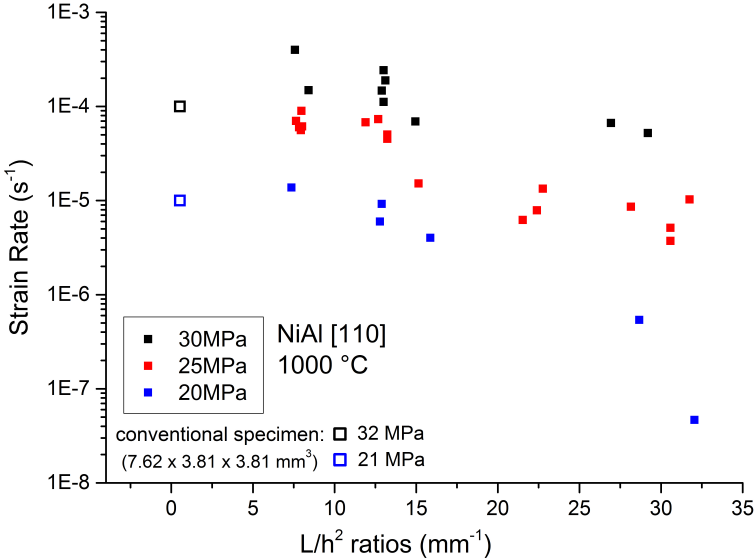


Figure 4.33: Diagram of steady-state/min creep strain rates  $\dot{\epsilon}$  vs. the ratio of gauge length to the square of thickness ( $L/h^2$ ) of the miniaturized specimens and the conventional specimens in size of  $7.62 \times 3.81 \times 3.81 \text{ mm}^3$  from Literature [91] in [110] soft orientation

In this diagram, the creep strain rate showed a dependence on the  $L/h^2$  ratio. Specimens with larger  $L/h^2$  ratios have reduced creep strain rates. Two conventional specimens with size  $7.62 \times 3.81 \times 3.81 \text{ mm}^3$  [91] were plotted in this diagram for comparison; their creep strain rates showed a good agreement with the L400 specimens, which have the smallest  $L/h^2$  ratios

of the miniaturized specimens. The L400 specimens may be considered as the lower limit for specimen miniaturization for which the influence of the GNDs generated due to the setup misalignment on the creep behavior can be ignored, at least under the experimental conditions in this study.

From the simplified cantilever model, the maximum and minimum surface bending stress caused by the setup misalignment can be calculated as:

$$\sigma_b = \pm 6 \cdot \sigma_x \cdot \tan(\theta) \cdot \frac{L}{h} \quad (4.8)$$

By assuming stress 25 MPa and a misalignment angle  $0.2^\circ$ , the max/min bending stress for the L200 specimens is  $\pm 3.66$  MPa, for the L400 and S200 specimens it is  $\pm 1.83$  MPa. Transferred to the creep tests, the additional max/min bending stress in the specimen will lead to an increased or reduced creep strain rate. For the L200 specimens, a stress variation from 21.34 MPa to 28.66 MPa can be caused along the cross-section, this stress error can evidently influence the creep strain rate so that a local strain gradient forms along the specimen cross-section. This strain gradient is not only dependent on the magnitude of the bending stress but also relevant to the specimen thickness [43]. Thus the L200 specimens contain the most significant strain gradient due to the largest bending stress and smallest specimen thickness. The S200 and L400 specimens have identical max/min surface bending stress, but the thickness of the S200 specimens is smaller resulting in an increased strain gradient. A FEM simulation was carried out with Abaqus CAE for a more detailed analysis of the stress and strain distribution on the L400, L200 and S200 miniaturized specimens under the influence of the bending load. The simulation results will be compared with the simplified cantilever model. Dog-bone-shaped specimens were modeled to simulate the experimental conditions as similar as possible. The Young's modulus of NiAl single crystal in [110] soft orientation at  $1000^\circ\text{C}$  is set as 150 GPa according to the work from Rusovic [121] and Wasilewski [122]. The top ends of all the specimens are fixed and constant tensile stress of

25 MPa is set with the direction along the gauge length in each specimen. By assuming all the specimens enduring the same misalignment angle, here  $0.2^\circ$  was used again as in the simplified cantilever model. The corresponding bending loads are calculated from the misalignment angle multiplying the loads converted from the constant tensile stress, which are 4 N for the L400 specimen and 1 N for the L200 and S200 specimens, thence the bending loads are 0.0035 N for L200 and S200 specimens and 0.014 N for L400 specimen. We set the bending loads at the lower shoulder part of the specimens, where the specimen and the lower adapter are contacted resulting in the bending load. The direction of all the bending loads is vertical to the gauge length. The stress and strain distribution of the miniaturized specimens will be analyzed under the influence of the constant tensile stress and the bending load. Figure 4.34 shows the stress distribution of all the three miniaturized specimens.

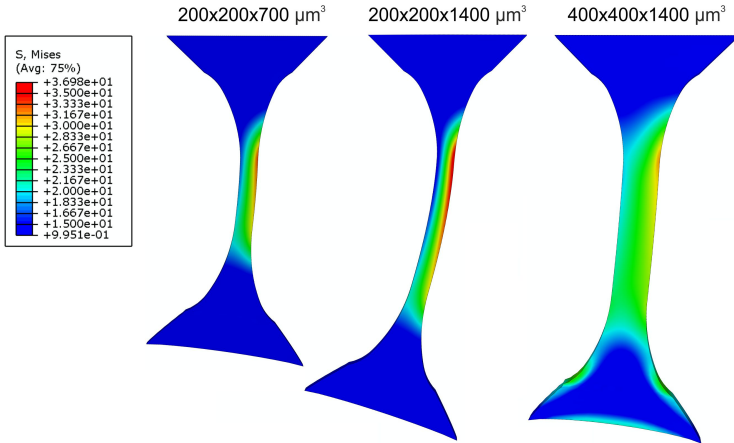


Figure 4.34: Stress distribution of the S200, L200 and L400 under 25 MPa and  $0.2^\circ$  misalignment angle with FEM simulation.

As expected, the L200 specimen contains the largest bending stress around 35 MP located at one side around the top shoulder of the specimen, the min-



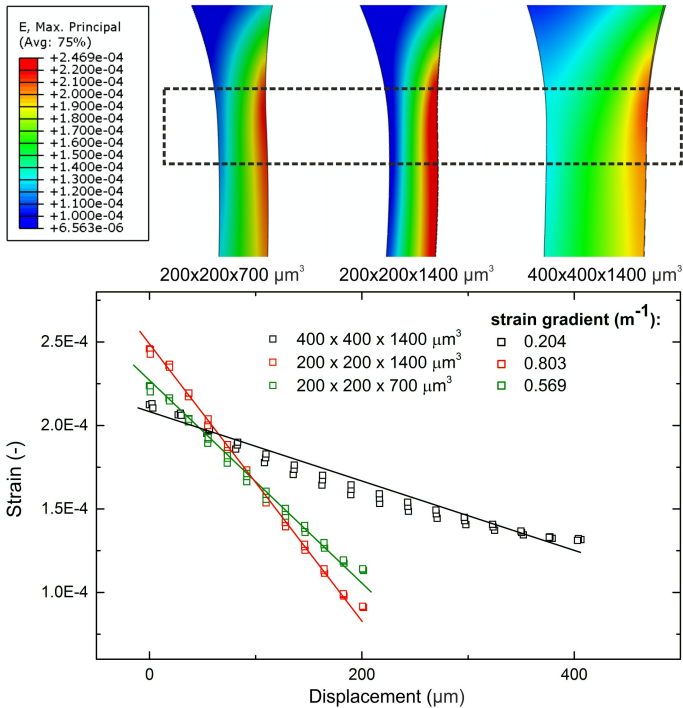


Figure 4.35: Strain gradient analysis of the S200, L200 and L400 specimens in FEM simulation, the magnitude of the strain gradients showed a dependence on the  $L/h^2$  ratios

imum surface bending stress on the opposite side is around 15 MPa, a stress difference of 20 MPa was formed, which leads to different creep strain rates in this area. Therefore generation of GNDs and even sub-boundaries for stress relaxation in the specimen is inevitable, which act as obstacles for the dislocation motion resulting in reduced creep strain rates. The S200 specimen and L400 specimens showed reduced stress localization due to smaller  $L/W$  ratios. Figure 4.35 shows the strain distribution at the top areas of the three specimens in the FEM simulation, where strain localization due to the bending effect was observed. Strain gradients along the specimen thickness

Table 4.4: curvature calculation based on FEM simulation and the simplified cantilever model from equation 4.7

specimen sizes	from FEM simulation		from cantilever model	
	curvature ( $m^{-1}$ )	multiple	curvature ( $m^{-1}$ )	multiple
L200	0.803	3.94	0.245	4
S200	0.569	2.78	0.1225	2
L400	0.204	1	0.06125	1

near these areas were calculated with linear regression. Thus, the corresponding curvatures can be determined and compared with those calculated from the simplified cantilever model in Table 4.4. The curvatures calculated from the cantilever model showed a relation of 4: 2: 1, which is related to the  $L/h^2$  ratios of the miniaturized specimens. The curvatures from the FEM simulation contained larger values and yielded 3.94: 2.78: 1. The reason for the observed differences is due to the different locations of the bending load. In the cantilever model, the bending load is applied at the end of the gauge length in the miniaturized specimens. In the FEM simulation, the bending load is applied at the lower shoulder part of the specimens, therefore the load arms of the bending load are larger than the gauge lengths resulting in increased curvatures. Still, the curvatures calculated from both methods showed the same tendency that increasing curvatures were observed in specimens with larger  $L/h^2$  ratios. Additionally, the FEM simulation suggested that the curvature caused by the setup misalignment is not only dependent on the  $L/h^2$  ratios but also is sensitive to the location of the bending load on the miniaturized specimens.

The FEM simulation verified the reliability of the simplified cantilever model that strain gradients due to specimen alignment uncertainties will lead to the formation of a corresponding GND pattern in the initial stage of creep testing. The GND density is mainly affected by the specimen geometry, i.e.,  $L/h^2$  ratio.

## 4.2.8 Accuracy of the GND determination

Based on the simplified cantilever model, the initial GND densities caused by the setup misalignment are  $9.72 \times 10^{10} \text{ m}^{-2}$  for the L200 specimen and  $2.43 \times 10^{10} \text{ m}^{-2}$  for the L400 specimen tested at  $1000 \text{ }^\circ\text{C}$  and  $25 \text{ MPa}$ . The GND densities with the smallest strain of 0.05 based on the misorientation results from the EBSD data were  $5.56 \times 10^{13} \text{ m}^{-2}$  for L200 specimen and  $3.05 \times 10^{13} \text{ m}^{-2}$  for L400 specimen under the same experimental conditions. A difference of factor 3 was determined. Even though the GND density calculated by the simplified cantilever model will be increased when the miniaturized specimens were strained to 0.05, the apparent difference of the GND density calculated from the two methods needs to be discussed. In the first step, the accuracy of the GND density measured by EBSD will be discussed. Jiang et al. [123] have studied that the separation of dislocations between GND and SSD depends on the step size in EBSD. They found that dislocations with opposite directions such as dipoles and multipoles can not result in curvature between the measured points with increased step size in the EBSD measurement. Hence, these dislocations are not recognized as GNDs. To study the influence of the step size on GND density in our case, the L200 specimen tested under  $25 \text{ MPa}$ ,  $1000 \text{ }^\circ\text{C}$  and strained to 0.05 were measured by EBSD with step sizes of  $3 \text{ }\mu\text{m}$ ,  $4 \text{ }\mu\text{m}$  and  $8 \text{ }\mu\text{m}$ .

Table 4.5: Influence of the step sizes on the GND density

GND density ( $\text{m}^{-2}$ )	mean	median	min	max
step size $3 \text{ }\mu\text{m}$	$1.68 \times 10^{14}$	$1.31 \times 10^{14}$	$2.41 \times 10^{13}$	$1.75 \times 10^{15}$
step size $4 \text{ }\mu\text{m}$	$8.38 \times 10^{13}$	$5.57 \times 10^{13}$	$1.43 \times 10^{13}$	$1.15 \times 10^{15}$
step size $8 \text{ }\mu\text{m}$	$4.66 \times 10^{13}$	$3.39 \times 10^{13}$	$7.64 \times 10^{12}$	$2.46 \times 10^{14}$

Figure 4.36 shows the GND density maps with the three step sizes. The initial step size is  $4 \text{ }\mu\text{m}$  for the miniaturized specimens, which could be considered as a reference value. With smaller step size  $3 \text{ }\mu\text{m}$ , the mean

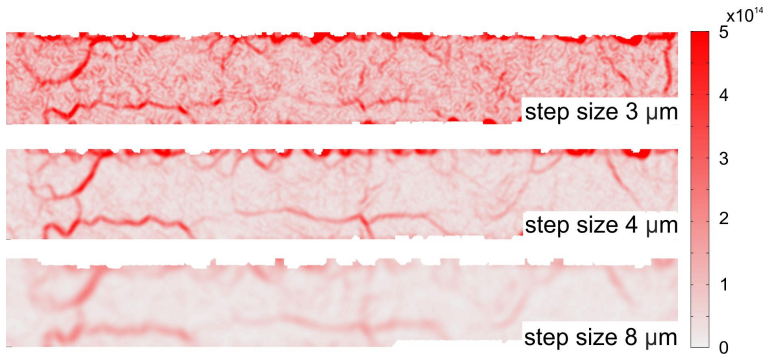


Figure 4.36: GND calculation of one L200 specimen tested at 1000 °C, 25 MPa and a strain of 0.05 with the step sizes of 3  $\mu\text{m}$ , 4  $\mu\text{m}$  and 8  $\mu\text{m}$

GND density increased from  $8.38 \times 10^{13} \text{ m}^{-2}$  to  $1.68 \times 10^{14} \text{ m}^{-2}$ , the min GND density increased from  $1.42 \times 10^{13} \text{ m}^{-2}$  to  $2.41 \times 10^{13} \text{ m}^{-2}$ , which is due to the increased influence of the noise in the EBSD measurement [116]. The noise is due to the limited accuracy of orientation measurement, which is related to the specimen quality and accuracy limitation of the EBSD instrument. Therefore the noise signal for the same specimen is identical and the corresponding background noise is increased with smaller step size in the GND calculation. The increased background noise leads to a reduced contrast in the GND density map, some areas with GND localization can no longer be detected and the detailed information about the GND distribution is lost. With larger step size 8  $\mu\text{m}$ , the mean GND density decreased from  $8.38 \times 10^{13} \text{ m}^{-2}$  to  $4.66 \times 10^{13} \text{ m}^{-2}$ , the GND density map showed also reduced contrast, because the misorientation calculated between neighbor points contained fewer details due to the increased step sizes.

The GND density maps with different step sizes suggest that the quantitative determination of the GND density and the quality of the GND density maps suffers multiple influencing factors in the EBSD measurement. The comparison of GND density is only meaningful when all the miniaturized

specimens were prepared with the same polishing process and measured with the identical step sizes: 4  $\mu\text{m}$  was used in this study. For the simplified cantilever model, a pure bending effect due to the setup misalignment is assumed in this model, which implies the GNDs in the bending area are most homogeneous and evenly distributed along the gauge length of the miniaturized specimens. This means that the corresponding GND density represents the theoretical lower boundary of the dislocation density. Therefore the apparent difference between the GND density calculated from the simplified cantilever model and from the EBSD measurement can be explained by the different conditions for quantitatively determining GND density, i.e., different step sizes and assumption of GND distribution. Even though the quantitative comparison of GND density is not suitable, the GND density shows a dependence on the  $L/h^2$  ratio of the miniaturized specimens. The simplified cantilever model is a reliable explanation for the geometrically related creep behavior of the miniaturized specimens.

#### **4.2.9 Equivalent GND determination with the DIC method**

Still, more detailed information about the GND density and distribution of the miniaturized specimens with a strain smaller than 0.05 is necessary for a more detailed understanding of the GND evolution method in the miniaturized specimens. Unfortunately, GND analysis for the miniaturized specimens with a strain smaller than 0.05 is not possible with EBSD measurement under the experimental conditions in this study, because the GND density is overcast by the noise in the EBSD measurement so that the actual dislocation structure can't be detected. One possible way to obtain the GND evolution is to convert the strain distribution data analyzed with the DIC method into a GND or curvature value. From the works of Gioacchino et al. [124], Jiang et al. [125] and Yan et al. [126], this method was proven to be a promising alternative to study the deformation in materials. Because EBSD measures the crystal misorientation on the specimen surface after de-

formation, the GND density can be calculated from the misorientation and a GND distribution map on the specimen surface is available. Similarly, the DIC method measures changes in the surface displacements through tracking of surface features. A shear strain distribution can be calculated from the surface displacement field so that an equivalent GND distribution map is available with the DIC method. In this study, the 2D mesh grid analyzed on the miniaturized specimen surface was converted to a 1D line by calculating mean displacements in each column along the gauge length. A schematic diagram in Figure 4.37 shows the conversion method. Based on

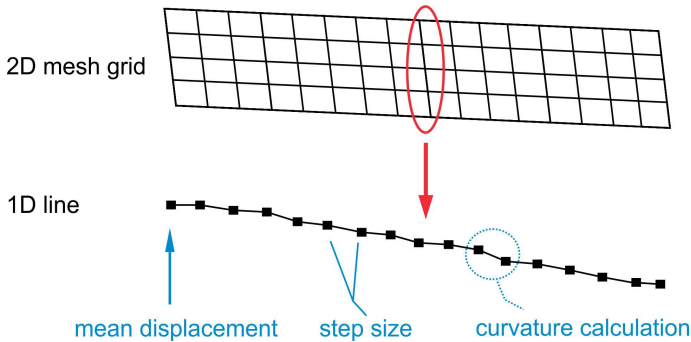


Figure 4.37: The schematic diagram of the determination of the equivalent GND density with the DIC method by calculating the curvature values of the miniaturized specimen in a simplified 1D line model

the simplified 1D line model, the curvature values between each data point can be calculated from the mean shear strain and step size, then the corresponding GND density is available. The reason to use the simplified 1D line model is to first reduce the noise level by using the mean value of shear strains because of the limited accuracy of the DIC measurement compared to EBSD. Second, a better approximation to the simplified cantilever model can be achieved with the 1D line model. A quantitative determination of the GND density calculated from the DIC method is not the main goal since the GND density is definitely influenced by the limited accuracy and reduced

resolution of the DIC measurement compared to the EBSD measurement in this study. The critical point is to analyze the evolution of the GND density of the miniaturized specimens in the initial stage of creep testing and verify the simplified cantilever model. Therefore, the miniaturized specimens were analyzed at strains from the first data point up to a strain of 0.05. The step sizes of each miniaturized specimen analyzed with the DIC method are converted from the size of the mesh grid. The conversion unit ( $\mu\text{m}/\text{pixel}$ ) is calculated using the initial gauge length ( $\mu\text{m}$ ) divided by the whole length of the mesh grid (pixel), which is usually around  $0.7 \sim 1.3 \mu\text{m}/\text{pixel}$ . Suitable step size is also necessary to be determined since the step size has an identical effect to the equivalent GND density calculated by the DIC method as the EBSD method. With smaller step size, the accuracy limitation of the DIC method results in an increased background noise, which causes a so-called spurious GND density [58]. This spurious GND density can be approximated by equation 4.9:

$$\rho_{sp} = \frac{2 \cdot \theta_n}{b \cdot k \cdot d} \quad (4.9)$$

Where  $\rho_{sp}$  is the spurious GND density,  $\theta_n$  is the equivalent misorientation noise angle caused by the accuracy limit of the DIC method,  $b$  is the Burgers vector,  $d$  is the mesh grid size (pixel) and  $k$  is the conversion unit ( $\mu\text{m}/\text{pixel}$ ). The actual accuracy of the DIC method is  $\pm 0.02$  pixels resulting in a maximum difference of 0.04 pixels between two neighbor points in this study. Therefore the maximal misorientation can be calculated as:

$$\theta_n = \arctan\left(\frac{0.04}{d}\right) \quad (4.10)$$

Now the spurious GND density can be presented as:

$$\rho_{sp} = \frac{2 \cdot \arctan\left(\frac{0.04}{d}\right)}{b \cdot k \cdot d} \quad (4.11)$$

One S200 miniaturized specimen tested at 1000 °C and 25 MPa was analyzed with mesh grid sizes in  $20 \times 20$ ,  $30 \times 30$ ,  $40 \times 40$  and  $70 \times 70$  pixels, the conversion unit is  $0.78 \mu\text{m}/\text{pixel}$ . The equivalent GND densities from the first data point up to a strain of 0.05 are plotted in Figure 4.38 together with the lower limit for the step size, which is determined by the maximum background noise calculated from the maximum spurious GND density, and the upper limit for the step size as proposed by Kysar et al. [116], they suggested that one reasonable length scale for the upper limit is the inverse of the principle curvature of the crystal lattice,  $\kappa$ , which scales as  $\rho_{\text{gnd}} \cdot b$ .

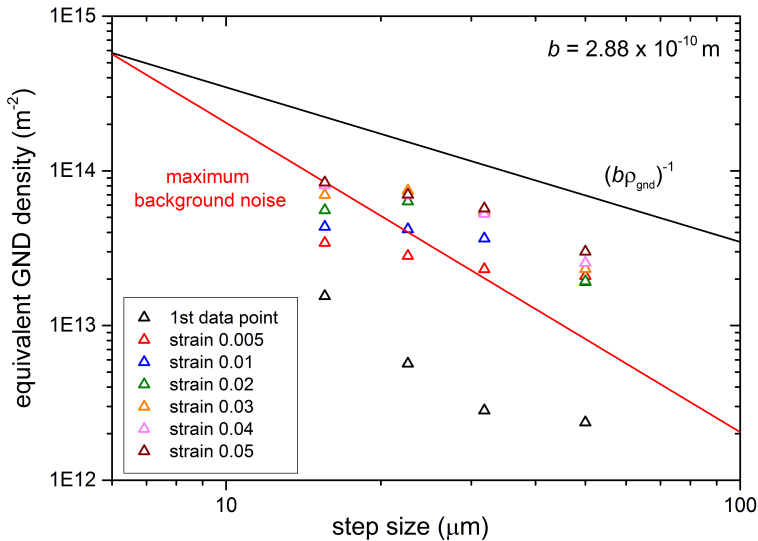


Figure 4.38: Influence of step sizes on the equivalent GND density with the DIC method, together with the lower limit and top limits for the step size based on  $\rho_{sp}$  and calculation by Kysar et al. [116]

The equivalent GND density calculated by the DIC method also showed an evident dependence on the step size in that the GND density reduced with a larger step size. With strain increased from the first data point to 0.05, the GND density is increased due to the bending effect and creep deforma-



tion. At equivalent step size  $50\ \mu\text{m}$  (mesh grid of  $70 \times 70$  pixels), the GND density showed the least contrast compared to other step sizes, which is due to the loss of detailed curvature information with larger step sizes. With the reduction of step sizes from  $32\ \mu\text{m}$  (mesh grid of  $40 \times 40$  pixels),  $23\ \mu\text{m}$  (mesh grid of  $30 \times 30$  pixels) to  $15\ \mu\text{m}$  (mesh grid of  $20 \times 20$  pixels), increased GND density was observed and more data points are below the maximum background noise floor. A suitable step size of  $30\ \mu\text{m}$  is chosen for the DIC method since the corresponding equivalent GND densities in most strain values are located in the reasonable area between the maximum background noise floor and the upper limit for the step size. After confirmation of the suitable step size for the DIC method, all the miniaturized specimens of NiAl in [110] soft orientation were analyzed to study the GND evolution from the first data point to a strain of 0.05 at 20 MPa, 25 MPa and 30 MPa.

Figure 4.39 (a) shows a diagram of the equivalent GND density vs.  $L/h^2$  ratio of the specimens tested at 20 MPa. The equivalent GND density shows a linear dependence on the  $L/h^2$  ratio. Increased GND density was observed with a larger  $L/h^2$  ratio in strain from the first data point to 0.05. Linear regression was carried out to have a better observation of the linear dependence between equivalent GND density and the  $L/h^2$  ratio. Figure 4.39 (b) shows the equivalent GND density vs. strain from the first data point to 0.05 of the L400, S200 and L200 specimens. The equivalent GND density of the three specimens yielded an apparent increase with strain from the first data point to 0.01. Afterward, a reduced increasing rate was observed in the strain from 0.02 to 0.05. This suggests that the GND density caused by the bending effect due to the setup misalignment was nearly saturated after a strain of 0.02, the subsequent increase of the GND density would then be mainly caused by the creep deformation.

Figure 4.40 and 4.41 show the result of the specimens tested at 25 MPa and 30 MPa. The equivalent GND density also showed an apparent dependence

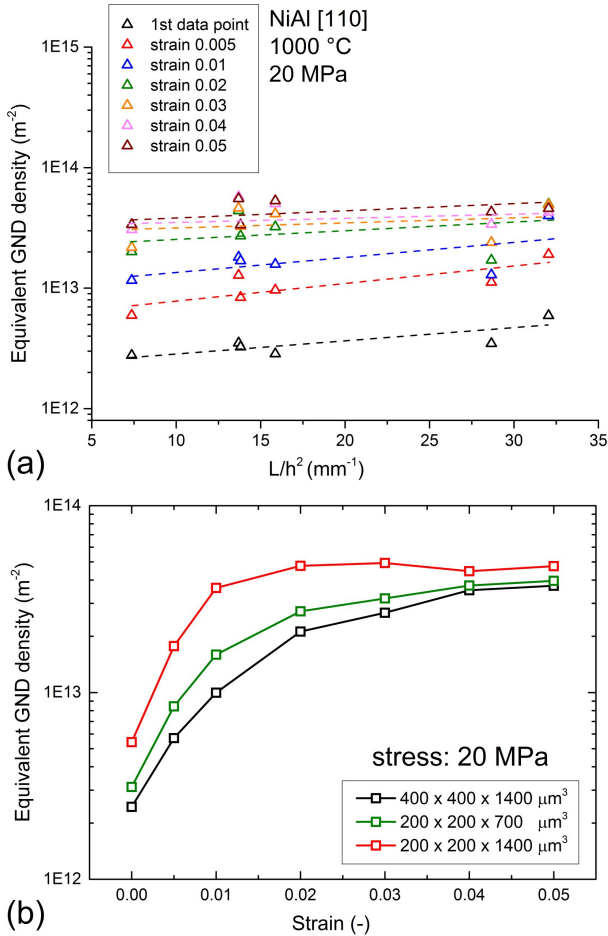


Figure 4.39: Diagram of the equivalent GND density ( $m^{-2}$ ) vs.  $L/h^2$  ratio ( $mm^{-1}$ ) (a) and vs. strain (-) (b) of the miniaturized NiAl single crystalline specimens in [110] soft orientation tested at 1000 °C and 20 MPa with strain from 1st data point to 0.05

on the  $L/h^2$  ratios that increased GND density was observed in specimens with larger  $L/h^2$  ratios. From strain 0.01 to 0.05, we have observed again that the increasing rate of the equivalent GND density is reduced compared

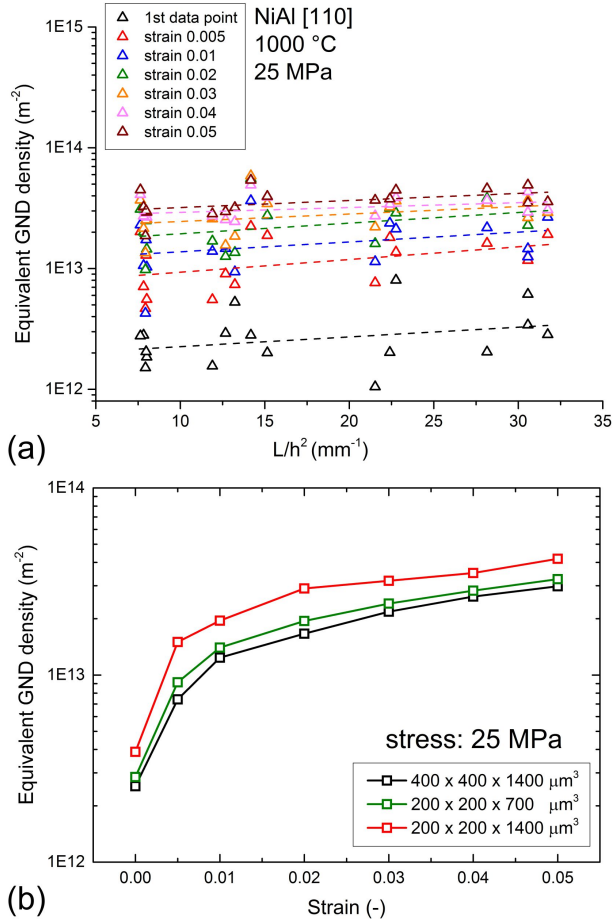


Figure 4.40: Diagram of the equivalent GND density ( $\text{m}^{-2}$ ) vs.  $L/h^2$  ratio ( $\text{mm}^{-1}$ ) (a) and vs. strain (-) (b) of the miniaturized NiAl single crystalline specimens in [110] soft orientation tested at  $1000\text{ }^{\circ}\text{C}$  and  $25\text{ MPa}$  with strain from 1st data point to 0.05

to the value at strain from the first data point to 0.01. It is noteworthy that the difference of the equivalent GND density in the specimens is smaller with increasing stress, especially in the range of strain from the first data point to 0.01. According to the simplified cantilever model and the FEM simu-

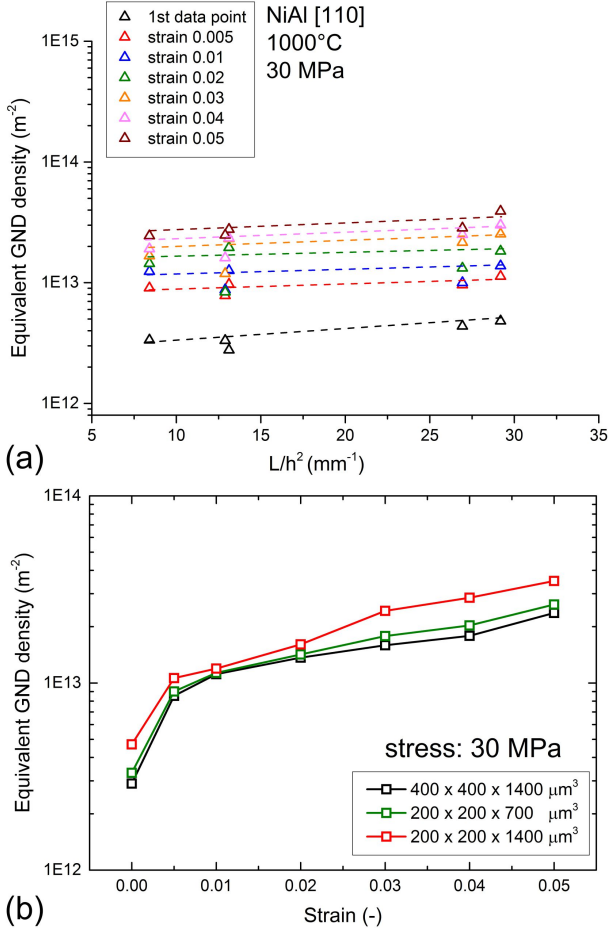


Figure 4.41: Diagram of the equivalent GND density ( $m^{-2}$ ) vs.  $L/h^2$  ratio ( $mm^{-1}$ ) (a) and vs. strain (-) (b) of the miniaturized NiAl single crystalline specimens in [110] soft orientation tested at 1000 °C and 30 MPa with strain from 1st data point to 0.05

lation, GNDs are generated by the setup misalignment and inhomogeneous stress distribution is formed due to the bending effect. If the initial stress is not large enough, i.e., 20 MPa here, for dislocation glides to overcome the

GNDs, the different creep strain rates due to the inhomogeneous stress distribution will result in an increased strain gradient in the specimen, thence a larger strain gradient can be measured with the DIC method resulting in an increased equivalent GND density. If the initial stress is large, i.e., 30 MPa, dislocations will have enough driving force to overcome the GND obstacle with dislocation glides so that the GNDs generated by the bending effect have less influence on the creep strain rates of the miniaturized specimens. With the analysis of the equivalent GND density, we have found that the GND density is not only dependent on the  $L/h^2$  ratio of the miniaturized specimens but also on the magnitude of the initial stress, which influences the driving force for dislocation glides to overcome the GND obstacles.

#### **4.2.10 Summary for NiAl miniaturized specimens in [110] soft orientation**

NiAl single crystalline miniaturized specimens in [110] soft orientation were tested at 1000 °C with stress 20 MPa, 25 MPa and 30 MPa in size of L400, L300, L200 and S200, the creep behavior of the miniaturized specimens can be concluded as:

Decreasing creep strain rates were observed in specimens with larger  $L/h$  ratios. But the creep mechanism for specimens with different sizes is identical, which is dislocation glide on  $\{011\}\langle 100\rangle$  slip systems.

For the miniaturized specimens with larger  $L/h$  ratios, an increasing shear strain localization was observed in the strain distribution analysis with the DIC method and, correspondingly, a larger GND density was detected with EBSD measurement.

The setup misalignment, which is the source of the GND generation, was determined at the beginning of the micro-tensile creep tests with the DIC method. A simplified cantilever model demonstrated that the GND density is dependent on the  $L/h^2$  ratio of the specimens under the influence of setup

misalignment. The minimum/steady-state creep strain rates show dependence on the  $L/h^2$  ratio of the miniaturized specimens.

Based on the shear strain analysis with the DIC method, equivalent GND density was calculated to study the evolution of the GND density. Specimens with larger  $L/h^2$  ratios have increased equivalent GND density. An apparent increase of equivalent GND was observed at strains from the first data point to 0.01 due to the bending effect caused by the setup misalignment. The evolution of the equivalent GND density shows a dependence on the  $L/h^2$  ratio and on the initial stress of the specimens.

Factors such as oxidation and stress localization have a negligible influence on the creep behavior of the miniaturized specimens.

### **4.3 Tensile creep testing in [100] hard orientation**

For NiAl single crystal in [100] hard orientation, there exists no driving force for  $\langle 100 \rangle$  dislocation glides as in [110] soft orientation. The plastic deformation in creep is dominated by the motion of  $\langle 110 \rangle$  dislocations and dislocation climb. Therefore, different influence of specimen miniaturization and misalignment of the customized setup on the creep behavior of the miniaturized specimens of NiAl single crystal in [100] hard orientation is to be expected.

#### **4.3.1 Experimental results**

The miniaturized specimens of NiAl single crystal in [100] hard orientation were tested at 1000 °C with stresses of 40 MPa, 50 MPa and 60 MPa in air under constant stress condition until fracture. Miniaturized specimens with sizes of L400 ( $400 \times 400 \times 1400 \mu\text{m}^3$ ), L200 ( $200 \times 200 \times 1400 \mu\text{m}^3$ ) and S200 ( $200 \times 200 \times 700 \mu\text{m}^3$ ) were used to study the influence of different specimen sizes on the creep behavior.

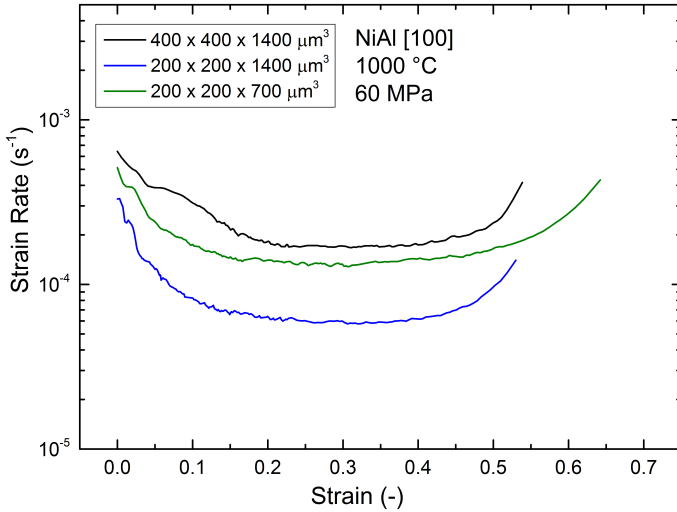


Figure 4.42: Creep curves of NiAl single crystalline miniaturized specimens tested in 1000 °C and 60 MPa in [100] hard orientation.

Figures 4.42 to 4.44 show the test results for stress of 60 MPa, 50 MPa and 40 MPa, respectively: The fracture strains of all the three specimens were over 0.5 and all the creep curves contained a normal primary creep stage and an evident steady-state creep stage under all three stresses. Specimens with larger  $L/h^2$  ratios showed reduced creep strain rates. The Norton plot in Figure 4.45 compiles the steady-state creep strain rates vs. stress for the miniaturized specimens in different sizes. A smaller difference of the creep strain rates was observed at lower stress. This phenomenon is opposite to the results of the miniaturized specimens of NiAl single crystal in [110] soft orientation, where the difference of the creep strain rates is increased at lower stress. At stress 40 MPa, the creep strain rates of the L400 and S200 specimens were in good agreement with the result of the conventional specimen in size of  $3.81 \times 3.81 \times 20.3 \text{ mm}^3$  in the work of Forbes et.al [91]. The stress exponents  $n$  of all the miniaturized specimens exhibit values from 5.8 to 7.6, which is also in good agreement with literature [91]. The influence of speci-

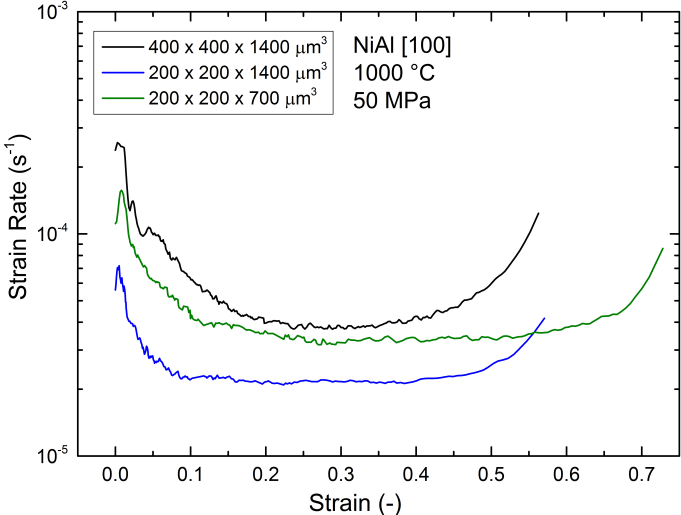


Figure 4.43: Creep curves of NiAl single crystalline miniaturized specimens tested in  $1000^\circ C$  and  $50 MPa$  in  $[100]$  hard orientation.

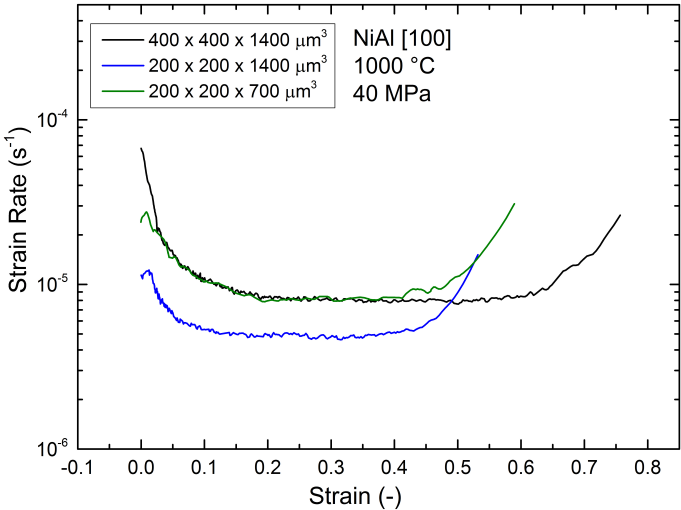


Figure 4.44: Creep curves of NiAl single crystalline miniaturized specimens tested in  $1000^\circ C$  and  $40 MPa$  in  $[100]$  hard orientation.



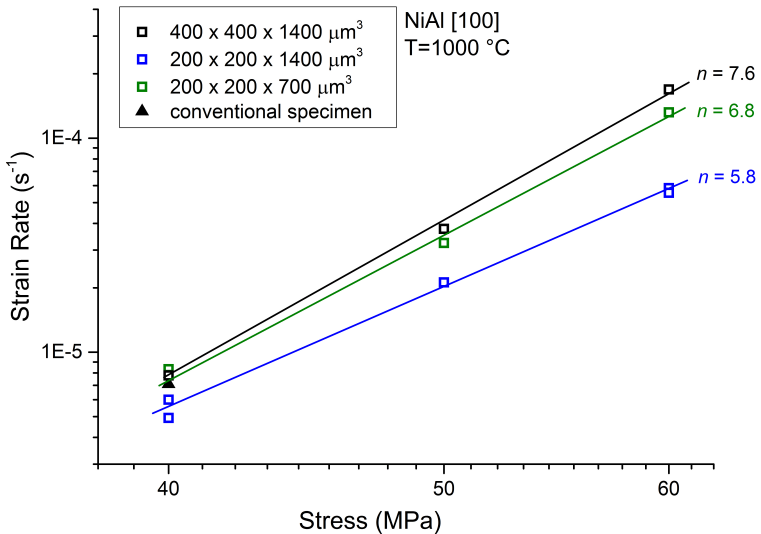


Figure 4.45: Norton-plot of NiAl miniaturized specimens in [100] hard orientation summarizing minimum/steady-state creep strain rates at 1000 °C with the comparison of steady-state creep strain rates for conventional specimens from the literature.

men miniaturization was also detected in [100] hard orientation: Specimens with larger  $L/h^2$  ratios have reduced creep strain rates.

### 4.3.2 Fracture surface and slip systems

The fracture surfaces of the L400, L200 and S200 specimens tested at 1000 °C and 40 MPa in [100] hard orientation were observed with an optical microscope as shown in Figure 4.46.

All the specimens showed a fourfold symmetric fracture surface. No evident slip traces on the specimen surface with a specific angle to the load direction were observed as for the specimens tested in [110] soft orientation. White stripes with direction vertical to load direction on the specimen surfaces (see Figure 4.46) were caused by the broken oxide layers due to the elongation of the specimens.

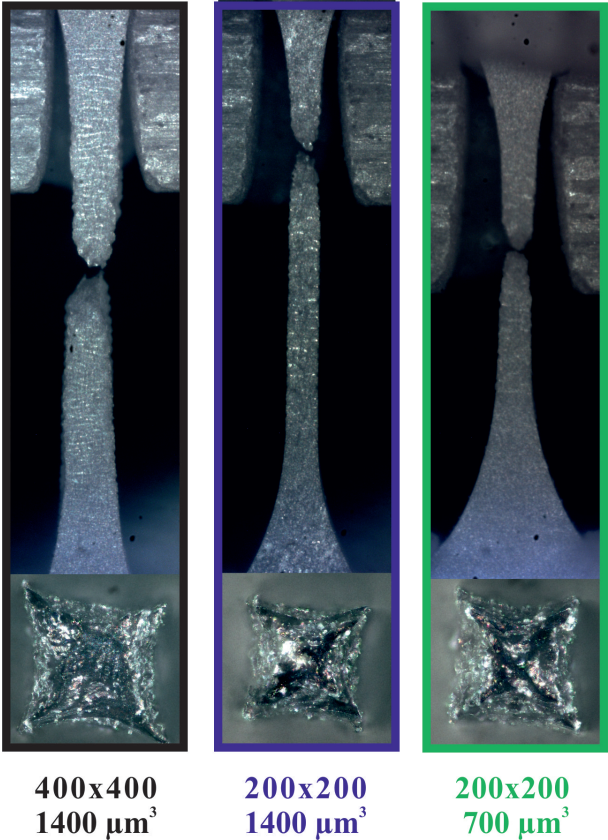


Figure 4.46: Fracture surfaces of the L400, L200 and S200 NiAl miniaturized specimens tested in 1000 °C and 40 MPa in [100] hard orientation.

Figure 4.47 shows the crystal orientation of the miniaturized specimens tested in [100] hard orientation, the load direction is [001] and the four specimen surfaces are parallel to the  $\{\bar{1}10\}$  and  $\{\bar{1}\bar{1}0\}$  planes. In the hard orientation, the resolved shear stress on the  $\{110\}\langle 100\rangle$  and  $\{100\}\langle 100\rangle$  slip systems approach zero, plastic deformation should occur by the glide of  $\langle 110\rangle$  dislocations and dislocation climb [98–100]. For a more detailed

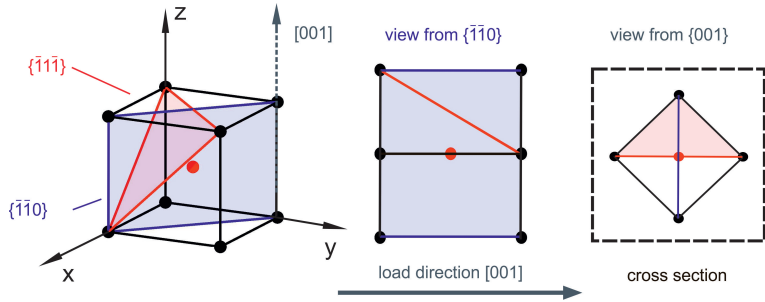


Figure 4.47: Crystal orientation of the NiAl miniaturized specimens in [100] hard orientation

study of the surface morphology, one L400 specimen tested at 1000 °C and 60 MPa was analyzed with an optical microscope. The angles between the load direction [001] and the projections of the four slip planes {011}, {0 $\bar{1}$ 1}, { $\bar{1}$ 01} and {101} on the four specimen surfaces were calculated (see table 4.6) and compared to the slip traces on the specimen surfaces (see Figure 4.48).

Table 4.6: Angle (°) between the projection from possible slip systems on each specimen surface and [001] load direction

slip planes \ angle	surface 1	surface 2	surface 3	surface 4
{011}	54.7°	125.3°	125.3°	54.7°
{0 $\bar{1}$ 1}	125.3°	54.7°	54.7°	125.3°
{ $\bar{1}$ 01}	54.7°	54.7°	125.3°	125.3°
{101}	125.3°	125.3°	54.7°	54.73°

The angles between the projections of each slip planes on the four surfaces and the load direction [001] were calculated; the results are 54.7° and 125.3° on all the four surfaces, which shows rotational symmetry to the [001] load direction. On the four surfaces, the identical slip traces with an angle close to 54.7° and 125.3° were observed, which confirmed the {110}<110> slip systems contributing to the creep deformation. Also, some slip traces par-

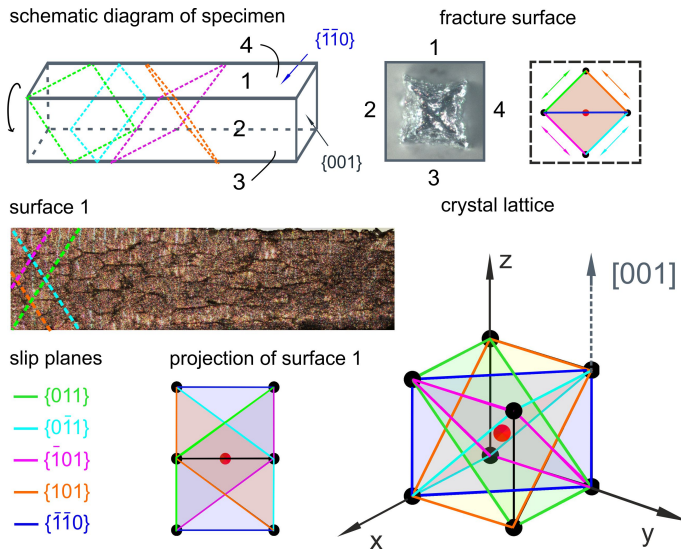


Figure 4.48: Determination of primary slip systems with analysis of slip traces on the four specimen surfaces of one L400 specimen tested at 1000 °C and 60 MPa in  $[100]$  hard orientation

allel to the  $[001]$  loading direction were detected on the surfaces. To study the influence of the initial stress on the slip traces, the surfaces of the other two L400 specimens tested at 1000 °C 50 MPa and 40 MPa were observed with an optical microscope, and their surface morphologies are compared in Figure 4.49.

The shape of the slip traces on the three surfaces viewed in Figure 4.49 showed a dependence on the stress. At 60 MPa, most of the slip traces are close to the  $54.7^\circ$  and  $125.3^\circ$  angles, and some slip traces are parallel to the  $[001]$  load direction. At 50 MPa, the slip traces showed similar distribution as the slip traces at 60 MPa, but the slip traces parallel to the load direction have increased proportion. At 40 MPa, almost only slip traces parallel to the  $[001]$  load direction were observed. This phenomenon can be explained by the work of Mills et al. [127]. They have reported that the  $\langle 110 \rangle$  dislo-

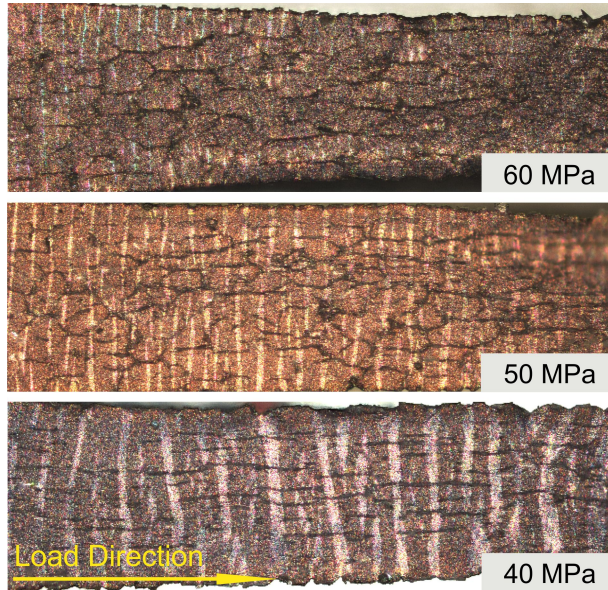


Figure 4.49: Slip traces of three L400 specimens tested at 1000 °C under stress 60 MPa, 50 MPa and 40 MPa

cations decompose into two separated  $\langle 100 \rangle$  dislocations with orthogonal Burgers' vectors in NiAl single crystal by plastic deformation in the [100] hard orientation. Based on their embedded atom method (EAM) calculations, they found that the perfect  $\langle 110 \rangle$  dislocation core is a metastable structure and readily decomposes upon the application of either stress or temperature to reduce the core energy of the dislocation. After decomposition, the  $\langle 100 \rangle$  dislocations do not have a common glide plane and there is not applied shear stress for their motion in the [100] hard orientation. Hence the edge part of these dislocations is effectively sessile and can move only via  $\langle 100 \rangle$  dislocations climb. For the L400 specimen tested at 40 MPa, more  $\langle 110 \rangle$  dislocations decomposed into  $\langle 100 \rangle$  dislocations with smaller creep strain rate, i.e., more creep lifetime until fracture, compared to the one

tested at 60 MPa. Therefore almost only slip traces parallel to the [001] load direction were observed on the specimen surface, which is possibly related to the climb of <100> dislocations.

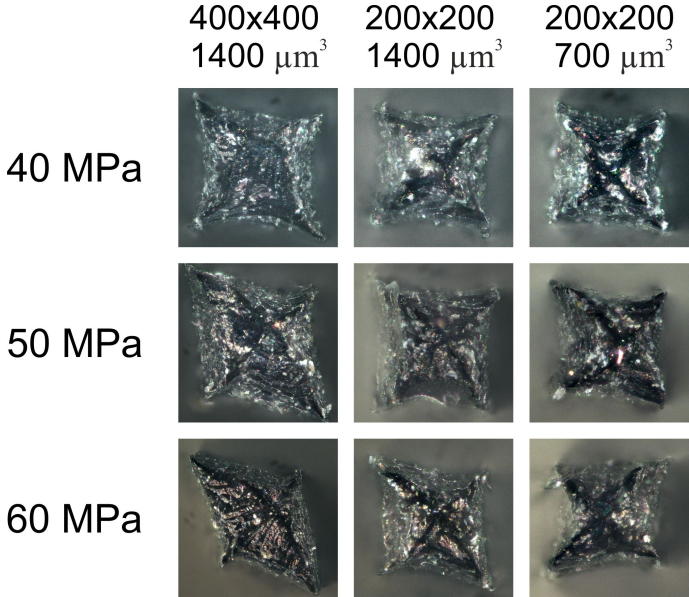


Figure 4.50: Fracture surfaces of the miniaturized specimens tested at stress 40 MPa, 50 MPa and 60 MPa in three different specimen sizes, similar fracture surfaces were observed.

The fracture surfaces of the L400, L200 and S200 specimens tested at stress 40MPa, 50MPa and 60MPa were plotted at Figure 4.50. The symmetry of the fracture surfaces is dependent on the stress: The fracture surfaces at stress 40 MPa were fourfold centrally symmetric. With increased stress to 60 MPa, the symmetric center point has moved along one diagonal and the shape of the fracture surface is no longer perfectly symmetric. This phenomenon is possibly caused by the rotation of the crystal lattice in the necking area.

### 4.3.3 Analysis of strain distribution

The strain distributions of the L400, L200 and S200 specimens tested at 1000 °C and 60 MPa in [100] hard orientation were analyzed just before the specimen fracture and at the steady-state creep stage, where the strain is 0.3. Figure 4.51 to 4.53 show the strain distribution of these three miniaturized specimens just before fracture. For the L400 specimen, the strain distributions in  $\epsilon_y$  and  $\epsilon_x$  before fracture were similar to the miniaturized specimens tested in [110] soft orientation, strain localization was observed at the necking area in the gauge length resulting in increased local stress until fracture. The shear strain showed different distribution compared to specimens in [110] soft orientation, no shear strain localization was detected at both ends of the [100] oriented miniaturized specimens, the most shear strain localization was observed at the necking area.

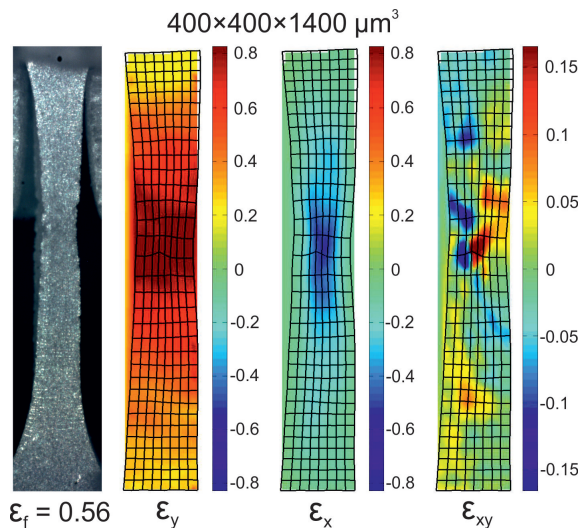


Figure 4.51: Strain distribution analysis of one L400 specimen tested at 1000 °C and 60 MPa before fracture

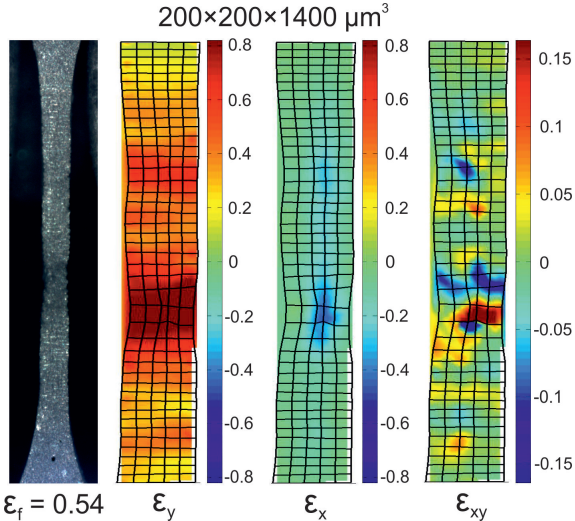


Figure 4.52: Strain distribution analysis of one L200 specimen tested at 1000 °C and 60 MPa before fracture

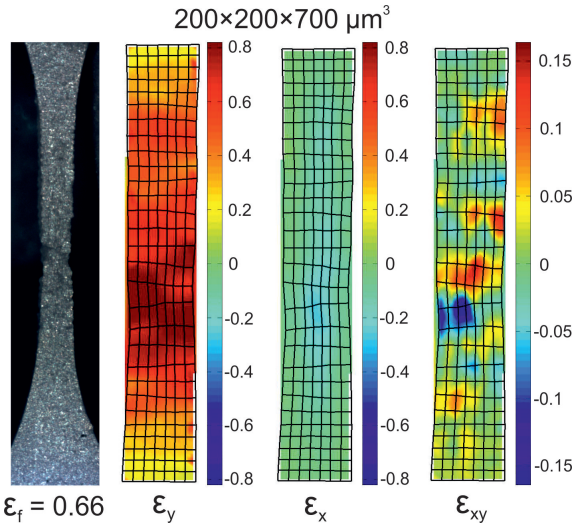


Figure 4.53: Strain distribution analysis of one S200 specimen tested at 1000 °C and 60 MPa before fracture



For the L200 specimen, two necking areas with strain localization were observed along the gauge length. The necking area at the lower part of the gauge length, which is also the fracture position, showed the most strain localization in  $\epsilon_y$ ,  $\epsilon_x$  and  $\epsilon_{xy}$ . The other necking area at the top part of the gauge length showed similar strain distribution but with a reduced magnitude of strain localization. This additional necking area was caused possibly by the increased  $L/W$  ratio of the L200 specimen compared to the L400 specimen and resulted in inhomogeneous stress distribution at the same global strain. For the S200 specimen, similar strain distributions in  $\epsilon_y$ ,  $\epsilon_x$  and  $\epsilon_{xy}$  were observed as the L400 specimen, no shear strain localization was observed at both specimen ends, the largest shear strain localization was detected at the necking area, where the fracture occurred.

Figures 4.54 to 4.56 show the strain distributions of the three specimens with a global strain of 0.3, where all the miniaturized specimens reached the

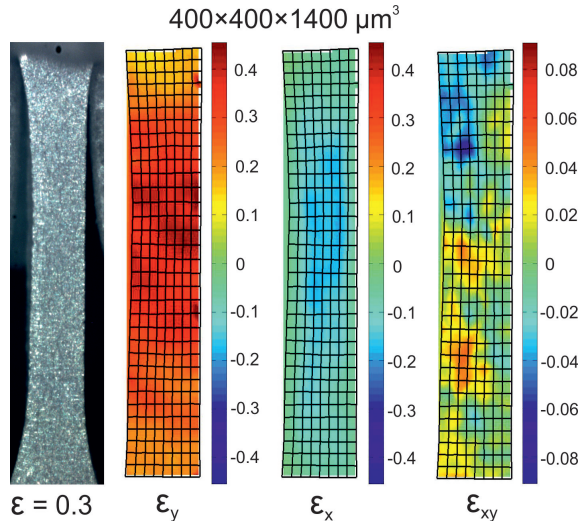


Figure 4.54: Strain distribution analysis of one L400 specimen tested at 1000 °C and 60 MPa at a strain of 0.3

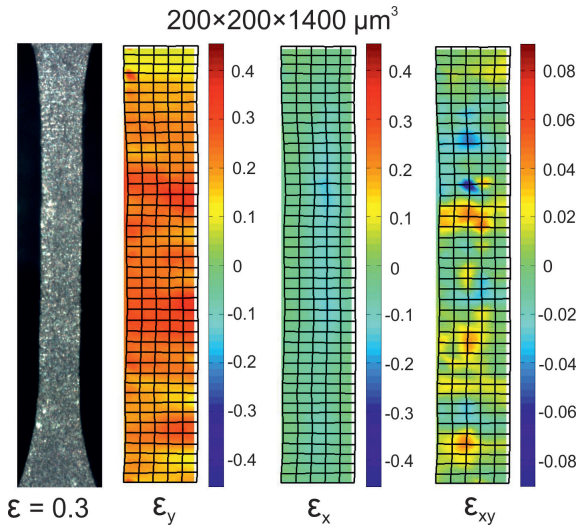


Figure 4.55: Strain distribution analysis of one L200 specimen tested at 1000 °C and 60 MPa at a strain of 0.3

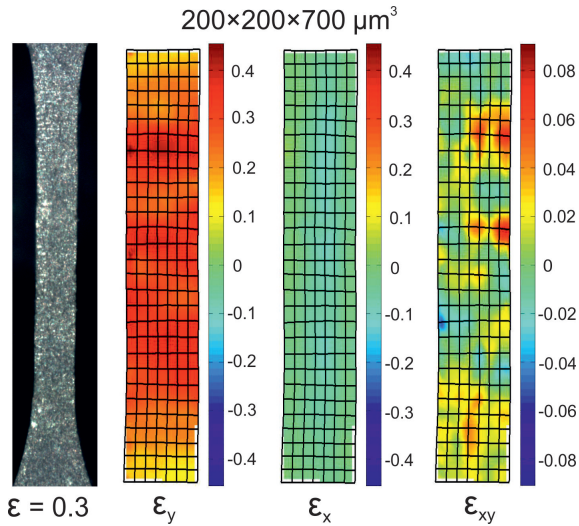


Figure 4.56: Strain distribution analysis of one S200 specimen tested at 1000 °C and 60 MPa at a strain of 0.3

steady-state creep stage. The strain distributions in  $\epsilon_y$ ,  $\epsilon_x$  and  $\epsilon_{xy}$  in the three specimens were homogeneous and not dependent on the specimen sizes. For the specimens in [100] hard orientation, similar strain distribution was observed regardless of specimen sizes. Therefore the difference of creep strain rates of specimens with different sizes was smaller compared to the results from the specimens in [110] soft orientation.

#### 4.3.4 Influence of oxidation

To study the oxidation influence on the miniaturized specimens tested in [100] hard orientation, the oxide layer of one L200 tested at 1000 °C and 40

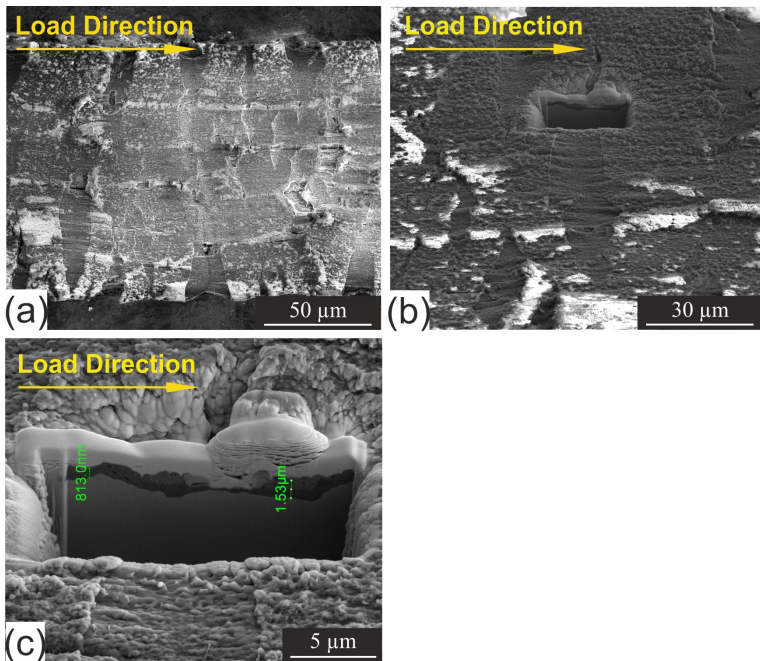


Figure 4.57: Analysis of the oxide layer thickness of one L200 specimen tested at 1000 °C and 40 MPa: (a) the morphology of the oxide layer away from the fracture surface, (b,c) a cross-section along the load direction with the oxide layer thickness under 2  $\mu\text{m}$ .

MPa was analyzed after fracture, the fracture time is 25.9 hours, which is largest among all the specimens tested in [100] hard orientation.

Figure 4.57 (a) shows the morphology of the oxide layer away from the fracture surface, fractured oxide layer was observed due to the elongation of the miniaturized specimen, the edges of the fractured oxide layer were not perfectly vertical to the load direction, but somehow rotated due to the creep deformation of the material. A cross-section was cut by FIB to measure the thickness of the oxide layer, the maximum thickness is 1.53  $\mu\text{m}$  resulting in a maximum stress error under 3% for the L200 and under 1.5% for the L400 specimens, which is similar to the stress error of specimens tested in [110] soft orientation. Thus, the stress error caused by the oxide layer has also a negligible influence on the creep behavior of the miniaturized specimens tested in [100] hard orientation. Fracture of the oxide layer was also observed suggesting the oxide layer does not contribute to mechanical strength.

### **4.3.5 Geometrically Necessary Dislocations (GND) determination with EBSD**

One L400 and one L200 specimen tested at 1000 °C under 40 MPa were mechanically polished for the EBSD analysis. Their misorientation and GNDs were analyzed in Figure 4.58 and Figure 4.59.

Figure 4.58 shows the EBSD analysis of the L400 specimen, the Inverse Pole Figure (IPF) showed that the crystal orientation along the specimen gauge length is [001] and vertical to the polished specimen surface is [011], which is in good agreement with the designated orientation by specimen manufacturing as explained in Figure 4.1. Strong crystal misorientation was observed in the specimen with a maximum angle of 12° resulting in dense mesh-shaped GND distribution and even grain boundaries. Close to the fracture surface, one grain was observed with orientation close to  $\langle\bar{1}22\rangle$ , which is possibly caused by the rotation of the crystal lattice due to the increased

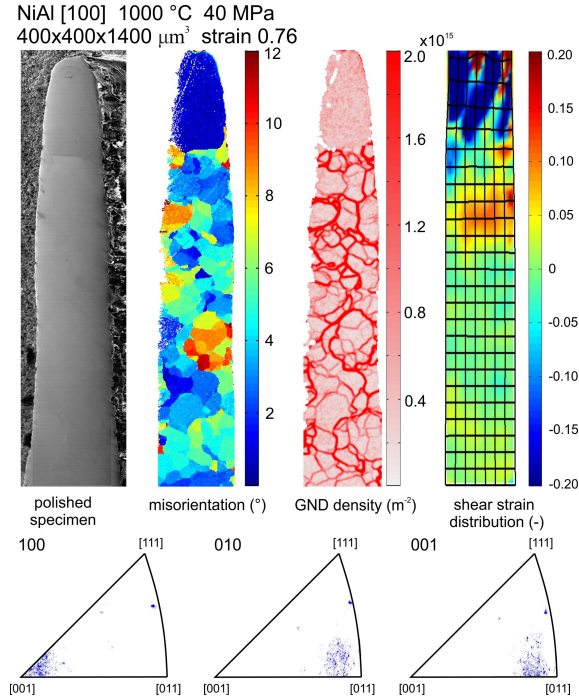


Figure 4.58: Misorientation and GND distribution with EBSD in comparison with the strain distribution with the DIC method in one L400 specimen tested at 1000 °C and 40 MPa with a fracture strain of 0.76

stress localization in the necking area. The crystal orientation in this grain related to the load direction is no longer [100] orientation, therefore  $\langle 001 \rangle$  dislocation glides can be stimulated.

Figure 4.59 shows the EBSD analysis of the L200 specimen, similar strong misorientation and mesh-shaped GND distribution were observed as the results in the L400 specimen. The similar GND distribution suggests that the specimen size of the miniaturized specimens tested in [100] orientation has only a weak influence on the creep behavior. Figure 4.60 shows the diagram plotted as steady-state creep strain rates ( $\dot{\epsilon}$ ) vs.  $L/h^2$  ratio of the mini-

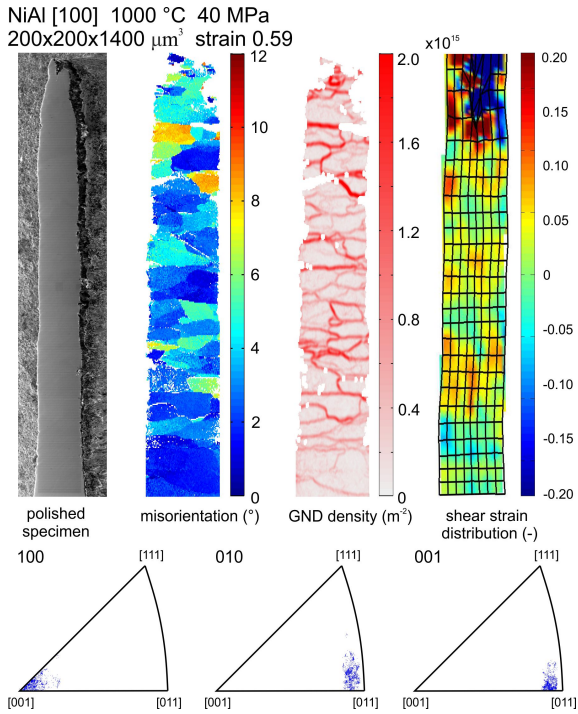


Figure 4.59: Misorientation and GND distribution with EBSD in comparison with the strain distribution with the DIC method in one L200 specimens tested at 1000 °C and 40 MPa with a fracture strain of 0.59

aturized specimens. The miniaturized specimens in [100] hard orientation showed less correlation between the creep strain rates and the  $L/h^2$  ratios compared to the specimens in [110] soft orientation, especially under lower stress, the creep strain rates are almost identical and very weakly related to the  $L/h^2$  ratios. The main reason for such a phenomenon is that the glides of the  $\langle 110 \rangle$  dislocations are obstructed because of their decomposition into two separated  $\langle 100 \rangle$  dislocations. Hence, the edge part of these dislocations is sessile and they can only move via dislocation climb. With lower stress, the creep strain rate in the [100] hard orientation is therefore controlled by

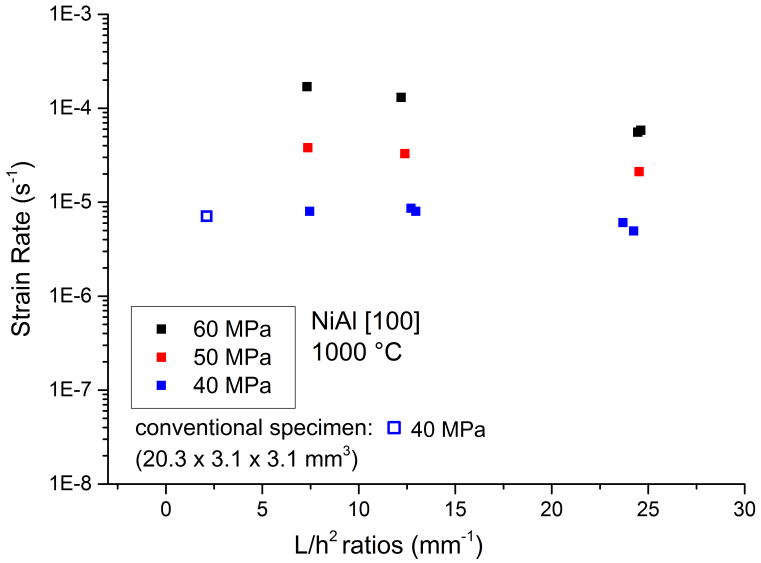


Figure 4.60: Diagram of steady-state/min creep strain rates  $\dot{\epsilon}$  vs. the ratio of gauge length to the square of thickness ( $L/h^2$ ) of the miniaturized specimens and the conventional specimens in size of  $20.3 \times 3.1 \times 3.1 \text{ mm}^3$  from Literature [91] in [100] hard orientation

dislocation climb. The GNDs have a much lesser effect on the creep deformation. With increased stress, the influence of the  $L/h^2$  ratios on the creep strain rates is stronger due to the increased contribution of the  $\langle 110 \rangle$  dislocation glides to the creep deformation and, simultaneously, there is also less time for dislocation climb available.

### 4.3.6 Tensile creep testing at different temperatures

The NiAl miniaturized specimens in [100] hard orientation were also tested at 60 MPa under different temperatures from  $1000 \text{ }^\circ\text{C}$  to  $850 \text{ }^\circ\text{C}$  to analyze the influence of the specimen miniaturization on activation energy, the result is shown in Figure 4.61.

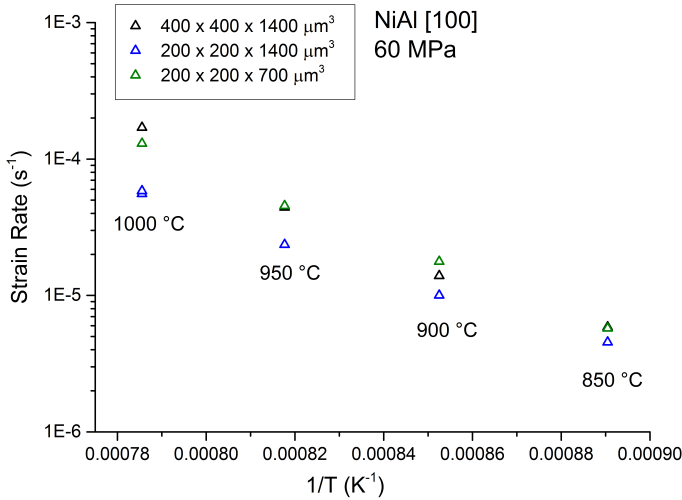


Figure 4.61: Arrhenius plot of the miniaturized specimens in [100] hard orientation for an initial stress level of 60 MPa for four temperatures of 850, 900, 950, and 1000 °C, respectively.

The activation energy ( $Q$ ) of the miniaturized specimens is  $266.5 \pm 25$  kJ/mol for the L400 specimens,  $244.8 \pm 6.1$  kJ/mol for the S200 specimens and  $202.8 \pm 6.9$  kJ/mol for the L200 specimens. Decreasing activation energy is observed in specimens with increasing  $L/h^2$  ratios. The activation energy of the L400 specimens,  $266.5 \pm 25$  kJ/mol, showed a good agreement with the results from Yang et. al [130] in the value of  $282.6 \pm 22$  kJ/mol, but smaller than the results from Forbes et. al [91] in the value of  $321 \pm 28$  kJ/mol. The different results of the activation energy are due to multiple factors, as Miracle [85] suggested that the activation energy of NiAl is related to stress, temperature and composition. In this work, the different specimen sizes and the setup misalignment due to the accuracy limitation of the customized setup are the additional influence factors to be considered. In our study, we do not have enough database for a more detailed explanation of the different activation energy of the miniaturized specimens in different sizes.



### 4.3.7 Summary for NiAl miniaturized specimens in [100] hard orientation

NiAl miniaturized specimens in [100] hard orientation were tested at 1000 °C with stresses 40 MPa, 50 MPa and 60 MPa in sizes of L400, L200 and S200, the creep behavior of the miniaturized specimens can be summarized as:

Decreasing creep strain rates were observed in specimens with larger  $L/h^2$  ratios due to the setup misalignment. The difference in creep strain rates in specimens with different sizes is smaller at lower stresses.

The strain distribution of the miniaturized specimens was analyzed with the DIC method. No influence of specimen sizes on the strain distribution was observed. The EBSD measurements showed that both L400 and L200 specimens contained similar strong misorientation and mesh-shaped GND distribution.

The  $\langle 110 \rangle$  dislocations decompose into two  $\langle 100 \rangle$  dislocations resulting in that the edge part of these dislocations is sessile and can only move via dislocation climb [127]. The creep strain rate of the miniaturized specimens in [100] hard orientation is controlled then by dislocation climb, especially at lower stresses, which is proven by the analysis of slip traces on the specimen surfaces. Therefore the GNDs generated by the setup misalignment have a very weak influence on the creep strain rates of the miniaturized specimens in [100] hard orientation as shown in Figure 4.60 compared to the ones in [110] soft orientation.

At stress 60 MPa, decreasing activation energy was observed in specimens with larger  $L/h^2$  ratios. The activation energy of the L400 specimens,  $266.5 \pm 25$  kJ/mol, showed a good agreement with the results from Literature. More database is needed for a detailed study of the activation energy of the miniaturized specimens.

Stress error caused by the oxide layer has a negligible influence on the creep behavior of the miniaturized specimens.



## 5 Summary

In this thesis, we have studied the influence of specimen miniaturization on creep behavior. Micro-tensile creep tests were carried out with Nimonic 75 polycrystalline and NiAl single crystalline miniaturized specimens in sub-mm scale up to temperature 1000 °C. A contactless strain measurement based on the DIC method was used in the customized setup, which provides a strain accuracy better than  $10^{-4}$  at 1000 °C and simultaneously enables the analysis of the strain distribution evolution on the miniaturized specimens. From the analysis of the test results of the miniaturized specimens, we have concluded the following:

The creep behavior of the Nimonic 75 polycrystalline miniaturized specimens showed a “thickness debit effect”. All the miniaturized specimens have reduced fracture strains compared to the conventional specimens, which is due to the growth of the intergranular cracks from the specimen surface resulting in strain localization in the early creep stage and stress increase. Still, the minimum creep strain rates of most of the miniaturized specimens showed a good agreement with the steady-state creep strain rates of the conventional specimens.

The NiAl single crystalline miniaturized specimens were tested in [110] soft and [100] hard orientation with different specimen sizes. The creep behavior of the miniaturized specimens in both orientations showed a “size effect” that decreasing creep strain rates were observed in specimens with larger  $L/h^2$  ratios. For these specimens, shear strain localization and increased GND density were detected using DIC and EBSD analysis. A simplified cantilever model was introduced and demonstrated that the GND density is

strongly dependent on the  $L/h^2$  ratio under the influence of setup misalignment. A qualitative Finite Element analysis confirmed the simplified cantilever model and revealed a considerable influence of setup misalignments on the GND formation. The influence of the GNDs on the creep behavior showed a dependence on the crystal orientation. For specimens in [110] soft orientation, the GNDs obstruct the  $\langle 100 \rangle$  dislocation glides resulting in decreased creep strain rates. Meanwhile, for specimens in [100] hard orientation, the  $\langle 110 \rangle$  dislocations decompose into two  $\langle 100 \rangle$  dislocations. The edge part of these dislocations is effectively sessile and can move only via  $\langle 100 \rangle$  dislocation climb. Therefore a weaker influence of the GNDs on the creep strain rates was detected compared to the specimens tested in [110] soft orientation.

A limit size of specimen miniaturization was observed in the thesis, i.e., the L400 miniaturized specimens. For a specimen size above the limit size, the creep behavior of the miniaturized specimens should be similar to the conventional specimens. Otherwise, increased influence of the specimen miniaturization on the creep behavior is expected, and such influence is dependent on the material property and simultaneously on the experimental conditions.

## 6 Outlook

The customized setup showed good accuracy and reproducibility in the micro-tensile creep testing. Still, setup misalignment due to the limited accuracy was detected. A corresponding bending effect is therefore unavoidable, which can influence the creep behavior of the miniaturized specimens. The following principal types of the misalignment in the customized setup are identified (see in Figure 6.1):

- (a). Lateral misalignment: the central axis of the top and bottom adapters is not in the same line when the miniaturized specimen is loaded. A bending effect is expected when the specimen is stretched, even though the top adapter can rotate to reduce some bending effect.
- (b). Rotatory misalignment: the central axis of the bottom adapter is not vertical when the miniaturized specimen is loaded. The top adapter rotates somehow to reduce the bending effect on the miniaturized specimen. However, the friction force in the ceramic rod prevents completely free rotation of the top adapter. Therefore the bending effect caused by rotatory misalignment is still unavoidable.
- (c). Camera misalignment: this is caused by the angular misalignment of the camera installation. No real bending effect exists in this condition, and the measured misalignment is an artificial error of the optical image analysis due to the fact that the elongation direction of the miniaturized specimen is not perfectly vertical in the images.
- (d). Top rod misalignment: the top rod is not vertically mounted. During the creep test, the top rod is also loaded under high temperature so that

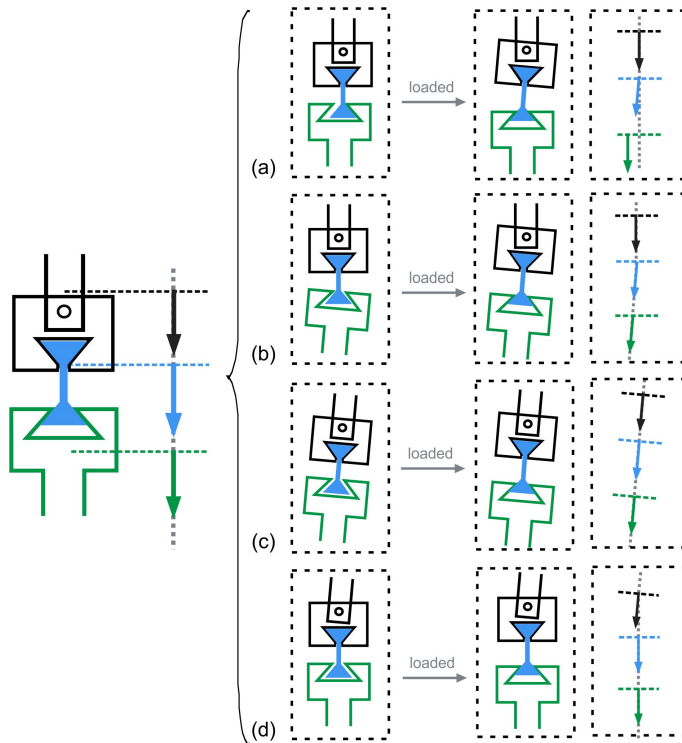


Figure 6.1: The schematic diagram showed the four possible types of the misalignment in the customized setup, left: ideal configuration, right: various configuration introducing specimen misalignment.

creep deformation is unavoidable in the top rod. The elongation of the top rod could also cause the rotation of the top adapter resulting in a similar rotatory misalignment as in case (b).

All these misalignments can occur simultaneously in the micro-tensile creep tests. From experience with the customized setup, some recommendations can be considered to reduce the influence of setup misalignment:

1. Prevent creep of supporting adapter to increase the stability of the customized setup.

- 
2. Prevent misalignment by design of new adapters or correct the position of the miniaturized specimen and adapter via DIC.
  3. Test with miniaturized specimens larger than a limit size so that the influence of setup misalignment is negligible on the creep behavior.

Oxidation was not a serious issue in this work. Still, testing under inert gas or vacuum atmosphere would be an option for creep tests over extended times, especially for materials with weak oxidation resistance or miniaturized specimens with even smaller cross-sections.

For the optimization of the miniaturized specimens, the most important influencing factor needed to be considered is the surface quality. All the specimens tested in this study were EDM manufactured and mechanically polished to reduce the surface roughness to  $\pm 1 \mu\text{m}$ , which causes a stress error below 3% for the L200 specimens. However, this surface quality is obviously not enough for specimens with even smaller cross-section due to the increased stress error. Hence, a better surface quality is necessary.





# A Appendix

## Specimen geometry and creep test results

The following tables show the test results of the Nimonic 75 polycrystalline and NiAl single crystalline miniaturized specimens under various experimental conditions in this study with different specimen sizes of:

**L400** :  $400 \times 400 \times 1400 \mu\text{m}^3$

**L300** :  $300 \times 300 \times 1400 \mu\text{m}^3$

**L200** :  $200 \times 200 \times 1400 \mu\text{m}^3$

**S200** :  $200 \times 200 \times 700 \mu\text{m}^3$

**Table A1: Nimonic 75 polycrystal at 850 °C under constant stress**

specimen	$\sigma$ (MPa)	$\dot{\epsilon}_{min}$ (s <sup>-1</sup> )	$\dot{\epsilon}_{plateau}$ (s <sup>-1</sup> )	$\epsilon_{fracture}$ (-)
L200	45	$1.56 \times 10^{-6}$	-	0.108
L200	80	$1.29 \times 10^{-5}$	-	0.125
L200	80	$1.24 \times 10^{-5}$	-	-
L400	45	$1.47 \times 10^{-6}$	-	0.139
L400	66	$7.00 \times 10^{-6}$	$9.61 \times 10^{-6}$	0.223
L400	80	$3.59 \times 10^{-5}$	-	0.257
L400	80	$2.66 \times 10^{-5}$	$3.93 \times 10^{-5}$	0.338
L400	80	$2.45 \times 10^{-5}$	-	-

**Table A2: Nimonic 75 polycrystal at 850 °C under constant load**

specimen	$\sigma$ (MPa)	$\dot{\epsilon}_{min}$ (s <sup>-1</sup> )	$\dot{\epsilon}_{plateau}$ (s <sup>-1</sup> )	$\epsilon_{fracture}$ (-)
L200	20	$1.69 \times 10^{-7}$	-	-
L200	30	$3.27 \times 10^{-7}$	-	-
L200	45	$9.77 \times 10^{-7}$	-	0.069
L200	50	$2.10 \times 10^{-6}$	-	-
L200	60	$2.75 \times 10^{-6}$	$3.54 \times 10^{-6}$	0.058
L200	66	$6.02 \times 10^{-6}$	-	0.057
L200	66	$8.19 \times 10^{-6}$	$2.21 \times 10^{-5}$	0.135
L200	70	$7.55 \times 10^{-6}$	-	-
L200	80	$1.45 \times 10^{-5}$	-	0.058
L200	80	$1.29 \times 10^{-5}$	-	0.163
L200	80	$1.94 \times 10^{-5}$	-	0.096
L200	90	$2.05 \times 10^{-5}$	-	0.084
L200	100	$6.95 \times 10^{-5}$	-	0.142
L200	120	$2.95 \times 10^{-4}$	-	0.138
L200	150	$9.60 \times 10^{-4}$	-	0.096
L400	30	$3.86 \times 10^{-7}$	$8.13 \times 10^{-6}$	0.105
L400	80	$1.52 \times 10^{-5}$	$4.53 \times 10^{-5}$	0.134
L400	80	$1.89 \times 10^{-5}$	-	0.239

**Table A3: Nimonic 75 polycrystal at 1000 °C under constant stress**

specimen	$\sigma$ (MPa)	$\dot{\epsilon}_{min}$ (s <sup>-1</sup> )	$\dot{\epsilon}_{plateau}$ (s <sup>-1</sup> )	$\epsilon_{fracture}$ (-)
L200	20	$7.03 \times 10^{-6}$	-	0.140
L200	40	$2.89 \times 10^{-5}$	-	0.131
L400	20	$3.79 \times 10^{-6}$	-	-
L400	40	$2.96 \times 10^{-5}$	$4.82 \times 10^{-5}$	0.189
L400	40	$5.30 \times 10^{-5}$	$6.29 \times 10^{-5}$	0.278
L400	40	$4.89 \times 10^{-5}$	$6.34 \times 10^{-5}$	0.226

**Table A4: Nimonic 75 polycrystal at 1000 °C under constant load**

specimen	$\sigma$ (MPa)	$\dot{\epsilon}_{min}$ (s <sup>-1</sup> )	$\dot{\epsilon}_{plateau}$ (s <sup>-1</sup> )	$\epsilon_{fracture}$ (-)
L200	10	$3.03 \times 10^{-7}$	-	-
L200	20	$4.11 \times 10^{-6}$	-	-
L200	30	$1.96 \times 10^{-5}$	-	0.111
L200	40	$2.04 \times 10^{-5}$	-	0.089
L200	40	$3.43 \times 10^{-5}$	-	0.072
L200	50	$1.12 \times 10^{-4}$	-	0.063
L200	60	$2.76 \times 10^{-4}$	-	0.102
L200	80	$1.02 \times 10^{-3}$	-	0.138
L400	40	$2.92 \times 10^{-5}$	$5.19 \times 10^{-5}$	0.212

**Table A5: Nimonic 75 polycrystal at 30 MPa under constant load**

specimen	T (°C)	$\dot{\epsilon}_{min}$ (s <sup>-1</sup> )	$\dot{\epsilon}_{plateau}$ (s <sup>-1</sup> )	$\epsilon_{fracture}$ (-)
L200	850	$3.27 \times 10^{-7}$	-	-
L200	900	$1.11 \times 10^{-6}$	-	-
L200	950	$4.27 \times 10^{-6}$	-	-
L200	1000	$1.96 \times 10^{-5}$	$4.82 \times 10^{-5}$	0.111

**Table A6: NiAl single crystal at 1000 °C under constant stress in [110] soft orientation**

specimen	$\sigma$ (MPa)	$\dot{\epsilon}_{min}$ (s <sup>-1</sup> )	$\epsilon_{fracture}$ (-)
L200	20	$5.38 \times 10^{-7}$	0.42
L200	20	$5.11 \times 10^{-8}$	-
L200	25	$1.01 \times 10^{-5}$	0.30
L200	25	$3.74 \times 10^{-6}$	0.29
L200	25	$5.13 \times 10^{-6}$	0.28
L200	25	$8.60 \times 10^{-6}$	-
L200	25	$7.88 \times 10^{-6}$	-
L200	25	$6.22 \times 10^{-6}$	-
L200	30	$4.77 \times 10^{-5}$	0.33
L200	30	$5.03 \times 10^{-5}$	0.28
L300	20	$4.01 \times 10^{-6}$	0.34
L300	25	$1.52 \times 10^{-5}$	0.32
L300	30	$6.92 \times 10^{-5}$	0.53
L400	20	$1.37 \times 10^{-5}$	0.57
L400	25	$5.79 \times 10^{-5}$	0.48
L400	25	$6.63 \times 10^{-5}$	0.55
L400	25	$5.61 \times 10^{-5}$	-
L400	25	$6.14 \times 10^{-5}$	-
L400	30	$1.49 \times 10^{-4}$	0.63
S200	20	$8.08 \times 10^{-6}$	0.38
S200	20	$6.17 \times 10^{-6}$	0.38
S200	25	$4.04 \times 10^{-5}$	0.39
S200	25	$5.21 \times 10^{-5}$	0.47
S200	25	$4.83 \times 10^{-5}$	0.40
S200	30	$1.47 \times 10^{-4}$	0.52
S200	30	$1.94 \times 10^{-4}$	0.44
S200	30	$1.89 \times 10^{-4}$	0.42
S200	30	$1.13 \times 10^{-4}$	0.38
S200	30	$1.17 \times 10^{-4}$	0.48

**Table A7: NiAl single crystal at 1000 °C under constant stress in [100] hard orientation**

specimen	$\sigma$ (MPa)	$\dot{\epsilon}_{min}$ (s <sup>-1</sup> )	$\epsilon_{fracture}$ (-)
L200	40	$4.93 \times 10^{-6}$	0.54
L200	40	$6.07 \times 10^{-6}$	0.59
L200	50	$2.12 \times 10^{-5}$	0.57
L200	60	$5.84 \times 10^{-5}$	0.54
L200	60	$5.56 \times 10^{-5}$	0.67
L400	40	$7.98 \times 10^{-6}$	0.76
L400	50	$3.81 \times 10^{-5}$	0.58
L400	60	$1.70 \times 10^{-4}$	0.56
S200	40	$7.99 \times 10^{-6}$	0.59
S200	40	$8.60 \times 10^{-6}$	-
S200	50	$3.24 \times 10^{-5}$	0.73
S200	60	$1.30 \times 10^{-4}$	0.66

**Table A8: NiAl single crystal at 60 MPa under constant stress in [100] hard orientation**

specimen	T (°C)	$\dot{\epsilon}_{min}$ (s <sup>-1</sup> )	$\epsilon_{fracture}$ (-)
L200	1000	$5.84 \times 10^{-5}$	0.54
L200	1000	$5.56 \times 10^{-5}$	0.67
L400	1000	$1.70 \times 10^{-4}$	0.56
S200	1000	$1.30 \times 10^{-4}$	0.66
L200	950	$2.36 \times 10^{-5}$	0.51
S200	950	$4.55 \times 10^{-5}$	0.63
L400	950	$4.42 \times 10^{-5}$	0.62
L200	900	$1.00 \times 10^{-5}$	0.47
L400	900	$1.39 \times 10^{-5}$	0.62
S200	900	$1.77 \times 10^{-5}$	0.56
L200	850	$4.55 \times 10^{-6}$	0.59
L400	850	$5.85 \times 10^{-6}$	0.51
S200	850	$5.75 \times 10^{-6}$	0.62



## References

- [1] R. P. Feynman, “There’s plenty of room at the bottom,” *Resonance*, vol. 16, no. 9, pp. 890–905, 2011.
- [2] D. G. Bogard and K. A. Thole, “Gas turbine film cooling,” *Journal of Propulsion and Power*, vol. 22, no. 2, pp. 249–270, 2006.
- [3] K. Takeishi, S. Aoki, T. Sato, and K. Tsukagoshi, “Film cooling on a gas turbine rotor blade,” *ASME 1991 International Gas Turbine and Aeroengine Congress and Exposition, June 3-6, 1991, Orlando, Florida, USA*. New York: American Society of Mechanical Engineers, 1991, p. V004T09A020.
- [4] A. H. Epstein, “Millimeter-scale, micro-electro-mechanical systems gas turbine engines,” *Journal of Engineering for Gas Turbines and Power*, vol. 126, no. 2, pp. 205–226, 2004.
- [5] J. H. Perepezko, “The hotter the engine, the better,” *Science*, vol. 326, no. 5956, pp. 1068–1069, 2009.
- [6] L. Hu, W. Hu, G. Gottstein, S. Bogner, S. Hollad, and A. Bührig-Polaczek, “Investigation into microstructure and mechanical properties of NiAl-Mo composites produced by directional solidification,” *Materials Science and Engineering: A*, vol. 539, pp. 211–222, 2012.
- [7] J. Bevk, R. Dodd, and P. Strutt, “The orientation dependence of deformation mode and structure in stoichiometric NiAl single crystals deformed by high temperature steady-state creep,” *Metallurgical Transactions*, vol. 4, no. 1, pp. 159–166, 1973.

- [8] S. S. Brenner, "Tensile strength of whiskers," *Journal of Applied Physics*, vol. 27, no. 12, pp. 1484–1491, 1956.
- [9] S. S. Brenner, "Plastic deformation of copper and silver whiskers," *Journal of Applied Physics*, vol. 28, no. 9, pp. 1023–1026, 1957.
- [10] M. D. Uchic, D. M. Dimiduk, J. N. Florando, and W. D. Nix, "Sample dimensions influence strength and crystal plasticity," *Science*, vol. 305, no. 5686, pp. 986–989, 2004.
- [11] V. Seetharaman and A. Cetel, "Thickness debit in creep properties of PWA 1484," *Superalloys 2004*, pp. 207–214, 2004.
- [12] R. W. Evans and B. Wilshire, *Creep of metals and alloys*. VT: IMM North American Pub. Center, Brookfield, 1985.
- [13] W. N. Sharpe, "Tensile testing of MEMS materials at high temperatures," *Applied Mechanics and Materials*, vol. 3, pp. 59–64, 2005.
- [14] W. C. Ang, P. Kropelnicki, O. Soe, J. H. Ling, A. Randles, A. Hum, J. Tsai, A. A. Tay, K. Leong, and C. S. Tan, "Novel development of the micro-tensile test at elevated temperature using a test structure with integrated micro-heater," *Journal of Micromechanics and Microengineering*, vol. 22, no. 8, p. 085015, 2012.
- [15] N. Karanjgaokar, C.-S. Oh, and I. Chasiotis, "Microscale experiments at elevated temperatures evaluated with digital image correlation," *Experimental Mechanics*, vol. 51, no. 4, pp. 609–618, 2011.
- [16] M. Zupan and K. Hemker, "High temperature microsample tensile testing of  $\gamma$ -TiAl," *Materials Science and Engineering: A*, vol. 319, pp. 810–814, 2001.
- [17] D. Leisen, R. Rusanov, F. Rohlfing, T. Fuchs, C. Eberl, H. Riesch-Oppermann, and O. Kraft, "Mechanical characterization between room temperature and 1000 °C of SiC free-standing thin films by



- a novel high-temperature micro-tensile setup,” *Review of Scientific Instruments*, vol. 86, no. 5, p. 055104, 2015.
- [18] Y. Zhao, Y. Guo, Q. Wei, T. Topping, A. Dangelewicz, Y. Zhu, T. Langdon, and E. Lavernia, “Influence of specimen dimensions and strain measurement methods on tensile stress–strain curves,” *Materials Science and Engineering: A*, vol. 525, no. 1-2, pp. 68–77, 2009.
- [19] W. Sharpe, B. Yuan, and R. Edwards, “A new technique for measuring the mechanical properties of thin films,” *Journal of Microelectromechanical Systems*, vol. 6, no. 3, pp. 193–199, 1997.
- [20] B. Pan, K. Qian, H. Xie, and A. Asundi, “Two-dimensional digital image correlation for in-plane displacement and strain measurement: a review,” *Measurement Science and Technology*, vol. 20, no. 6, p. 062001, 2009.
- [21] W. Peters and W. Ranson, “Digital imaging techniques in experimental stress analysis,” *Optical Engineering*, vol. 21, no. 3, p. 213427, 1982.
- [22] T. Chu, W. Ranson, and M. A. Sutton, “Applications of digital-image-correlation techniques to experimental mechanics,” *Experimental Mechanics*, vol. 25, no. 3, pp. 232–244, 1985.
- [23] M. Sutton, C. Mingqi, W. Peters, Y. Chao, and S. McNeill, “Application of an optimized digital correlation method to planar deformation analysis,” *Image and Vision Computing*, vol. 4, no. 3, pp. 143–150, 1986.
- [24] W. Peters, W. Ranson, M. Sutton, T. Chu, and J. Anderson, “Application of digital correlation methods to rigid body mechanics,” *Optical Engineering*, vol. 22, no. 6, p. 226738, 1983.
- [25] M. A. Sutton, S. R. McNeill, J. D. Helm, and Y. J. Chao, “Advances in two-dimensional and three-dimensional computer vision,” in *Pho-*

- tomechanics*, P. K. Rastogi, Eds. Topics in Applied Physics, vol 77. Berlin, Heidelberg: Springer, 2000, pp. 323–372.
- [26] B. Pan, D. Wu, and J. Gao, “High-temperature strain measurement using active imaging digital image correlation and infrared radiation heating,” *The Journal of Strain Analysis for Engineering Design*, vol. 49, no. 4, pp. 224–232, 2014.
- [27] R. B. Berke and J. Lambros, “Ultraviolet digital image correlation (UV-DIC) for high temperature applications,” *Review of Scientific Instruments*, vol. 85, no. 4, p. 045121, 2014.
- [28] J. Blaber, B. S. Adair, and A. Antoniou, “A methodology for high resolution digital image correlation in high temperature experiments,” *Review of Scientific Instruments*, vol. 86, no. 3, p. 035111, 2015.
- [29] Y. Q. Su, X. F. Yao, S. Wang, and Y. J. Ma, “Improvement on measurement accuracy of high-temperature DIC by grayscale-average technique,” *Optics and Lasers in Engineering*, vol. 75, pp. 10–16, 2015.
- [30] P. Sztetek, M. Vanleene, R. Olsson, R. Collinson, A. A. Pitsillides, and S. Shefelbine, “Using digital image correlation to determine bone surface strains during loading and after adaptation of the mouse tibia,” *Journal of Biomechanics*, vol. 43, no. 4, pp. 599–605, 2010.
- [31] J. Kang, Y. Ososkov, J. D. Embury, and D. S. Wilkinson, “Digital image correlation studies for microscopic strain distribution and damage in dual phase steels,” *Scripta Materialia*, vol. 56, no. 11, pp. 999–1002, 2007.
- [32] B. Wattrisse, A. Chrysochoos, J.-M. Muracciole, and M. Némoz-Gaillard, “Analysis of strain localization during tensile tests by digital image correlation,” *Experimental Mechanics*, vol. 41, no. 1, pp. 29–39, 2001.

- 
- [33] A. E. “Size effects in materials due to microstructural and dimensional constraints: a comparative review,” *Acta Materialia*, vol. 46, no. 16, pp. 5611–5626, 1998.
- [34] Z. P. Bažant, “Size effect on structural strength: a review,” *Archive of Applied Mechanics*, vol. 69, no. 9-10, pp. 703–725, 1999.
- [35] O. Kraft, P. A. Gruber, R. Mönig, and D. Weygand, “Plasticity in confined dimensions,” *Annual Review of Materials Research*, vol. 40, pp. 293–317, 2010.
- [36] T. Zhu and J. Li, “Ultra-strength materials,” *Progress in Materials Science*, vol. 55, no. 7, pp. 710–757, 2010.
- [37] E. Hall, “The deformation and ageing of mild steel: III discussion of results,” *Proceedings of the Physical Society. Section B*, vol. 64, no. 9, p. 747, 1951.
- [38] N. Petch, “The cleavage strength of polycrystals,” *Journal of the Iron and Steel Institute*, vol. 174, pp. 25–28, 1953.
- [39] A. Chokshi, A. Rosen, J. Karch, and H. Gleiter, “On the validity of the Hall-Petch relationship in nanocrystalline materials,” *Scripta Metallurgica*, vol. 23, no. 10, pp. 1679–1683, 1989.
- [40] G. Nieman, J. Weertman, and R. Siegel, “Micro-hardness of nanocrystalline palladium and copper produced by inert-gas condensation,” *Scripta metallurgica*, vol. 23, no. 12, pp. 2013–2018, 1989.
- [41] J. R. Greer and J. T. M. De Hosson, “Plasticity in small-sized metallic systems: Intrinsic versus extrinsic size effect,” *Progress in Materials Science*, vol. 56, no. 6, pp. 654–724, 2011.
- [42] J. R. Greer, W. C. Oliver, and W. D. Nix, “Size dependence of mechanical properties of gold at the micron scale in the absence of strain gradients,” *Acta Materialia*, vol. 53, no. 6, pp. 1821–1830, 2005.

- [43] N. Fleck, G. Muller, M. Ashby, and J. Hutchinson, "Strain gradient plasticity: theory and experiment," *Acta Metallurgica et Materialia*, vol. 42, no. 2, pp. 475–487, 1994.
- [44] D. Kiener, W. Grosinger, G. Dehm, and R. Pippan, "A further step towards an understanding of size-dependent crystal plasticity: In situ tension experiments of miniaturized single-crystal copper samples," *Acta Materialia*, vol. 56, no. 3, pp. 580–592, 2008.
- [45] D. Dimiduk, M. Uchic, and T. Parthasarathy, "Size-affected single-slip behavior of pure nickel microcrystals," *Acta Materialia*, vol. 53, no. 15, pp. 4065–4077, 2005.
- [46] B. Schuster, Q. Wei, H. Zhang, and K. Ramesh, "Microcompression of nanocrystalline nickel," *Applied Physics Letters*, vol. 88, no. 10, p. 103112, 2006.
- [47] J.-Y. Kim and J. R. Greer, "Size-dependent mechanical properties of molybdenum nanopillars," *Applied Physics Letters*, vol. 93, no. 10, p. 101916, 2008.
- [48] M. D. Uchic, P. A. Shade, and D. M. Dimiduk, "Plasticity of micrometer-scale single crystals in compression," *Annual Review of Materials Research*, vol. 39, pp. 361–386, 2009.
- [49] H. Bei, S. Shim, G. M. Pharr, and E. P. George, "Effects of pre-strain on the compressive stress–strain response of Mo-alloy single-crystal micropillars," *Acta Materialia*, vol. 56, no. 17, pp. 4762–4770, 2008.
- [50] Z. Shan, R. K. Mishra, S. S. Asif, O. L. Warren, and A. M. Minor, "Mechanical annealing and source-limited deformation in submicrometre-diameter ni crystals," *Nature Materials*, vol. 7, no. 2, p. 115, 2008.
- [51] H. Gao, Y. Huang, W. Nix, and J. Hutchinson, "Mechanism-based strain gradient plasticity - I. Theory," *Journal of the Mechanics and Physics of Solids*, vol. 47, no. 6, pp. 1239–1263, 1999.

- 
- [52] H. Gao and Y. Huang, “Geometrically necessary dislocation and size-dependent plasticity,” *Scripta Materialia*, vol. 48, no. 2, pp. 113–118, 2003.
- [53] L. Kubin and A. Mortensen, “Geometrically necessary dislocations and strain-gradient plasticity: a few critical issues,” *Scripta Materialia*, vol. 48, no. 2, pp. 119–125, 2003.
- [54] A. G. Evans and J. W. Hutchinson, “A critical assessment of theories of strain gradient plasticity,” *Acta Materialia*, vol. 57, no. 5, pp. 1675–1688, 2009.
- [55] H. Mughrabi, “On the current understanding of strain gradient plasticity,” *Materials Science and Engineering: A*, vol. 387, pp. 209–213, 2004.
- [56] C. Motz, T. Schöberl, and R. Pippan, “Mechanical properties of micro-sized copper bending beams machined by the focused ion beam technique,” *Acta Materialia*, vol. 53, no. 15, pp. 4269–4279, 2005.
- [57] E. Demir, D. Raabe, and F. Roters, “The mechanical size effect as a mean-field breakdown phenomenon: Example of microscale single crystal beam bending,” *Acta Materialia*, vol. 58, no. 5, pp. 1876–1886, 2010.
- [58] P. J. Konijnenberg, S. Zaeferrer, and D. Raabe, “Assessment of geometrically necessary dislocation levels derived by 3D EBSD,” *Acta Materialia*, vol. 99, pp. 402–414, 2015.
- [59] J. Nye, “Some geometrical relations in dislocated crystals,” *Acta Metallurgica*, vol. 1, no. 2, pp. 153–162, 1953.
- [60] A. Ueno, N. Takami, and R. Sato, “Study on establishing creep testing method using miniature specimen of lead free solders,” in *ECF17, Brno, Czech Republic, 2008*, J. Pokluda, P. Lukas, P. Sandera and

- I. Dlouhy, Eds. New York: Curran Associates, Inc., 2008, pp. 1120–1127.
- [61] T. Hyde and W. Sun, “A novel, high-sensitivity, small specimen creep test,” *The Journal of Strain Analysis for Engineering Design*, vol. 44, no. 3, pp. 171–185, 2009.
- [62] F. Krieg, M. Mosbacher, M. Fried, E. Affeldt, and U. Glatzel, “Creep and oxidation behaviour of coated and uncoated thin walled single crystal samples of the alloy PWA1484,” in *Superalloys 2016: Proceedings of the 13th International Symposium of Superalloys*, M. Hardy, et al., Eds. Hoboken, NJ, USA: John Wiley & Sons, 2016, pp. 773–779.
- [63] Z. Wen, H. Pei, D. Li, Z. Yue, and J. Gao, “Thickness influence on the creep response of DD6 Ni-based single-crystal superalloy,” *High Temperature Materials and Processes*, vol. 35, no. 9, pp. 871–880, 2016.
- [64] A. Srivastava, S. Gopagani, A. Needleman, V. Seetharaman, A. Staroselsky, and R. Banerjee, “Effect of specimen thickness on the creep response of a Ni-based single-crystal superalloy,” *Acta Materialia*, vol. 60, no. 16, pp. 5697–5711, 2012.
- [65] M. Bensch, E. Fleischmann, C. H. Konrad, M. Fried, C. M. Rae, and U. Glatzel, “Secondary creep of thin-walled specimens affected by oxidation,” *Superalloys 2012*, pp. 387–94, 2012.
- [66] R. Hüttner, J. Gabel, U. Glatzel, and R. Völkl, “First creep results on thin-walled single-crystal superalloys,” *Materials Science and Engineering: A*, vol. 510, pp. 307–311, 2009.
- [67] R. Hüttner, R. Völkl, J. Gabel, and U. Glatzel, “Creep behavior of thick and thin walled structures of a single crystal nickel-base superalloy at high temperatures—experimental method and results,” *Superalloys*. Warrendale: TMS, p. 719, 2008.

- [68] M. Brunner, M. Bensch, R. Völkl, E. Affeldt, and U. Glatzel, “Thickness influence on creep properties for ni-based superalloy M247LC SX,” *Materials Science and Engineering: A*, vol. 550, pp. 254–262, 2012.
- [69] G. Mälzer, R. Hayes, T. Mack, and G. Eggeler, “Miniature specimen assessment of creep of the single-crystal superalloy LEK 94 in the 1000 °C temperature range,” *Metallurgical and Materials Transactions A*, vol. 38, no. 2, pp. 314–327, 2007.
- [70] D. Peter, F. Otto, T. Depka, P. Nörtershäuser, and G. Eggeler, “High temperature test rig for inert atmosphere miniature specimen creep testing,” *Materialwissenschaft und Werkstofftechnik*, vol. 42, no. 6, pp. 493–499, 2011.
- [71] D. Kiener, C. Motz, and G. Dehm, “Micro-compression testing: A critical discussion of experimental constraints,” *Materials Science and Engineering: A*, vol. 505, no. 1-2, pp. 79–87, 2009.
- [72] P. Shade, R. Wheeler, Y. Choi, M. Uchic, D. Dimiduk, and H. Fraser, “A combined experimental and simulation study to examine lateral constraint effects on microcompression of single-slip oriented single crystals,” *Acta Materialia*, vol. 57, no. 15, pp. 4580–4587, 2009.
- [73] D. Raabe, D. Ma, and F. Roters, “Effects of initial orientation, sample geometry and friction on anisotropy and crystallographic orientation changes in single crystal microcompression deformation: A crystal plasticity finite element study,” *Acta Materialia*, vol. 55, no. 13, pp. 4567–4583, 2007.
- [74] C. Frick, B. Clark, S. Orso, A. Schneider, and E. Arzt, “Size effect on strength and strain hardening of small-scale [1 1 1] nickel compression pillars,” *Materials Science and Engineering: A*, vol. 489, no. 1-2, pp. 319–329, 2008.

- [75] H. Zhang, B. E. Schuster, Q. Wei, and K. T. Ramesh, "The design of accurate micro-compression experiments," *Scripta Materialia*, vol. 54, no. 2, pp. 181–186, 2006.
- [76] K. Hemker and W. Sharpe, "Microscale Characterization of Mechanical Properties," *Annual Review of Materials Research*, vol. 37, no. 1, pp. 93–126, 2007.
- [77] W. N. Sharpe, "Murray lecture tensile testing at the micrometer scale: Opportunities in experimental mechanics," *Experimental Mechanics*, vol. 43, no. 3, pp. 228–237, 2003.
- [78] W. N. Sharpe, "A Review of Tension Test Methods for Thin Films," *MRS Proceedings*, vol. 1052, pp. DD01–01, 2007.
- [79] C. Kirchlechner, P. Imrich, W. Grosinger, M. Kapp, J. Keckes, J. Micha, O. Ulrich, O. Thomas, S. Labat, C. Motz *et al.*, "Expected and unexpected plastic behavior at the micron scale: An in situ  $\mu$ laue tensile study," *Acta Materialia*, vol. 60, no. 3, pp. 1252–1258, 2012.
- [80] A. Sergueeva, J. Zhou, B. Meacham, and D. Branagan, "Gage length and sample size effect on measured properties during tensile testing," *Materials Science and Engineering: A*, vol. 526, no. 1-2, pp. 79–83, 2009.
- [81] W. Yuan, Z. Zhang, Y. Su, L. Qiao, and W. Chu, "Influence of specimen thickness with rectangular cross-section on the tensile properties of structural steels," *Materials Science and Engineering: A*, vol. 532, pp. 601–605, 2012.
- [82] M. Heilmaier and B. Reppich, "Creep lifetime prediction of oxide-dispersion-strengthened nickel-base superalloys: A micromechanically based approach," *Metallurgical and Materials Transactions A*, vol. 27, no. 12, pp. 3861–3870, 1996.



- [83] M. Heilmaier, "Model-based description of the creep deformation and fracture behavior of oxide-dispersion strengthened nickel-base superalloys," *Dissertation*, Univ. Erlangen-Nürnberg, Düsseldorf: Fortschrittberichte Reihe 5: Grund- und Werkstoffe, Nr. 286, VDI Verlag Düsseldorf, 1993.
- [84] R. Pascoe and C. Newey, "The mechanical behaviour of the intermediate phase NiAl," *Metal Science Journal*, vol. 2, no. 1, pp. 138–143, 1968.
- [85] D. Miracle, "Overview No. 104 the physical and mechanical properties of NiAl," *Acta Metallurgica et Materialia*, vol. 41, no. 3, pp. 649–684, 1993.
- [86] R. D. Noebe, R. R. Bowman, and M. V. Nathal, "Physical and mechanical properties of the B2 compound NiAl," *International Materials Reviews*, vol. 38, no. 4, pp. 193–232, 1993.
- [87] E. Arzt and P. Grahle, "High temperature creep behavior of oxide dispersion strengthened NiAl intermetallics," *Acta Materialia*, vol. 46, no. 8, pp. 2717–2727, 1998.
- [88] H. Bei and E. George, "Microstructures and mechanical properties of a directionally solidified NiAl-Mo eutectic alloy," *Acta Materialia*, vol. 53, no. 1, pp. 69–77, 2005.
- [89] D. Johnson, X. Chen, B. Oliver, R. Noebe, and J. Whittenberger, "Processing and mechanical properties of in-situ composites from the NiAl-Cr and the NiAl-(Cr, Mo) eutectic systems," *Intermetallics*, vol. 3, no. 2, pp. 99–113, 1995.
- [90] A. Misra, Z. Wu, M. Kush, and R. Gibala, "Microstructures and mechanical properties of directionally solidified NiAl-Mo and NiAl-Mo (Re) eutectic alloys," *Materials Science and Engineering: A*, vol. 239, pp. 75–87, 1997.

- [91] K. R. Forbes, U. Glatzel, R. Darolia, and W. D. Nix, "High-temperature deformation properties of NiAl single crystals," *Metallurgical and Materials Transactions A*, vol. 27, no. 5, pp. 1229–1240, 1996.
- [92] W. J. Yang and R. A. Dodd, "Steady-State Creep and Associated Microstructures in Stoichiometric and Non-Stoichiometric Polycrystalline NiAl," *Metal Science Journal*, vol. 7, no. 1, pp. 41–47, 1973.
- [93] J. Bevk, R. A. Dodd, and P. R. Strutt, "The orientation dependence of deformation mode and structure in stoichiometric NiAl single crystals deformed by high temperature steady-state creep," *Metallurgical Transactions*, vol. 4, no. 1, pp. 159–166, 1973.
- [94] A. Ball and R. E. Smallman, "The deformation properties and electron microscopy studies of the intermetallic compound NiAl," *Acta Metallurgica*, vol. 14, no. 10, pp. 1349–1355, 1966.
- [95] A. Ball and R. Smallman, "The operative slip system and general plasticity of NiAl-II," *Acta Metallurgica*, vol. 14, no. 11, pp. 1517–1526, 1966.
- [96] R. Wasilewski, S. Butler, and J. Hanlon, "Plastic deformation of single-crystal NiAl," *Transactions of the Metallurgical Society of AIME*, vol. 239, no. 9, pp. 1357–1364, 1967.
- [97] T. Takasugi, S. Hanada, and O. Izumi, "Slip modes in B2-type intermetallic alloys," *Materials Transactions, JIM*, vol. 31, no. 6, pp. 435–442, 1990.
- [98] R. D. Field, D. Lahrman, and R. Darolia, "Slip systems in  $\langle 001 \rangle$  oriented NiAl single crystals," *Acta Metallurgica et Materialia*, vol. 39, no. 12, pp. 2951–2959, 1991.
- [99] N. J. Zaluzec and H. L. Fraser, "The origin of dislocations with  $b = \langle 110 \rangle$  in single crystals of  $\beta$ -NiAl compressed along  $\langle 001 \rangle$  at elevated temperatures," *Scripta Metallurgica*, vol. 8, no. 9, pp. 1049–1053, 1974.

- 
- [100] R. T. Pascoe and C. W. A. Newey, "Deformation Modes of the Intermediate Phase NiAl," *Physica Status Solidi (b)*, vol. 29, no. 1, pp. 357–366, 1968.
- [101] H. Frost and M. Ashby, *Deformation-mechanism maps: the plasticity and creep of metals and ceramics*. Oxford: Pergamon Press, 1982.
- [102] M. Nganbe and M. Heilmaier, "High temperature strength and failure of the Ni-base superalloy PM 3030," *International Journal of Plasticity*, vol. 25, no. 5, pp. 822–837, 2009.
- [103] M. Nganbe and M. Heilmaier, "Creep Behavior and Damage of Ni-Base Superalloys PM 1000 and PM 3030," *Metallurgical and Materials Transactions A*, vol. 40, no. 12, p. 2971, 2009.
- [104] C. Eberl, R. Thompson, D. Gianola, and S. Bundschuh, "Digital image correlation and tracking," (Matlab Central File ID:12413, The Mathworks, Inc., Natick, MA, 2006).
- [105] E. Abbe, "Beiträge zur Theorie des Mikroskops und der mikroskopischen Wahrnehmung," *Archiv für mikroskopische Anatomie*, vol. 9, no. 1, pp. 413–418, 1873.
- [106] B. Pan, H. Xie, Z. Wang, K. Qian, and Z. Wang, "Study on subset size selection in digital image correlation for speckle patterns," *Optics Express*, vol. 16, no. 10, pp. 7037–7048, 2008.
- [107] S. Yaofeng and J. H. Pang, "Study of optimal subset size in digital image correlation of speckle pattern images," *Optics and Lasers in Engineering*, vol. 45, no. 9, pp. 967–974, 2007.
- [108] M. A. Sutton, J. Yan, V. Tiwari, H. Schreier, and J.-J. Orteu, "The effect of out-of-plane motion on 2D and 3D digital image correlation measurements," *Optics and Lasers in Engineering*, vol. 46, no. 10, pp. 746–757, 2008.

- [109] J. Zhang, S. Li, Z. Yang, G. Li, W. Hui, and Y. Weng, "Influence of inclusion size on fatigue behavior of high strength steels in the gigacycle fatigue regime," *International Journal of Fatigue*, vol. 29, no. 4, pp. 765–771, 2007.
- [110] E. Ezugwu, Z. Wang, and A. Machado, "The machinability of nickel-based alloys: a review," *Journal of Materials Processing Technology*, vol. 86, no. 1-3, pp. 1–16, 1999.
- [111] H. Riedel, *Fracture at High Temperatures*. Materials Research and Engineering, Vol. 37. Berlin, Heidelberg: Springer, 1987.
- [112] N. E. Dowling, *Mechanical Behavior of Materials: International Edition*. Harlow: Pearson Higher Ed, 2013.
- [113] R. W. Hertzberg, R. P. Vinci, and J. L. Hertzberg, *Deformation and fracture mechanics of engineering materials*. Chichester: J. Wiley & Sons, 1996.
- [114] M. Ashby, "The deformation of plastically non-homogeneous materials," *The Philosophical Magazine: A Journal of Theoretical Experimental and Applied Physics*, vol. 21, no. 170, pp. 399–424, 1970.
- [115] R. Sedláček, C. Schwarz, J. Kratochvíl, and E. Werner, "Continuum theory of evolving dislocation fields," *Philosophical Magazine*, vol. 87, no. 8-9, pp. 1225–1260, 2007.
- [116] J. Kysar, Y. Saito, M. Oztop, D. Lee, and W. Huh, "Experimental lower bounds on geometrically necessary dislocation density," *International Journal of Plasticity*, vol. 26, no. 8, pp. 1097–1123, 2010.
- [117] W. D. Nix, "Mechanical properties of thin films," *Metallurgical Transactions A*, vol. 20, no. 11, p. 2217, 1989.
- [118] M. Shell De Guzman, G. Neubauer, P. Flinn, and W. D. Nix, "The Role of Indentation Depth on the Measured Hardness of Materials," *MRS Online Proceedings Library Archive*, vol. 308, p. 613, 1993.

- [119] F. Bachmann, R. Hielscher, and H. Schaeben, “Texture Analysis with MTEX Free and Open Source Software Toolbox,” *Texture and Anisotropy of Polycrystals III*, vol. 160, pp. 63–68, 2010.
- [120] I. Szabó, *Einführung in die technische Mechanik: nach Vorlesungen*. Berlin, Heidelberg: Springer, 2013.
- [121] N. Rusović and H. Warlimont, “Young’s modulus of  $\beta$ 2-NiAl alloys,” *Physica Status Solidi (a)*, vol. 53, no. 1, pp. 283–288, 1979.
- [122] R. Wasilewski, “Elastic constants and youngs modulus of NiAl,” *Transactions of the Metallurgical Society of AIME*, vol. 236, no. 4, pp. 455–457, 1966.
- [123] J. Jiang, T. Britton, and A. Wilkinson, “Measurement of geometrically necessary dislocation density with high resolution electron backscatter diffraction: effects of detector binning and step size,” *Ultramicroscopy*, vol. 125, pp. 1–9, 2013.
- [124] F. Di Gioacchino and J. Q. Da Fonseca, “Plastic strain mapping with sub-micron resolution using digital image correlation,” *Experimental Mechanics*, vol. 53, no. 5, pp. 743–754, 2013.
- [125] J. Jiang, T. Zhang, F. P. Dunne, and T. B. Britton, “Deformation compatibility in a single crystalline Ni superalloy,” *Proceedings of the Royal Society A: Mathematical, Physical and Engineering Sciences*, vol. 472, no. 2185, p. 20150690, 2016.
- [126] D. Yan, C. C. Tasan, and D. Raabe, “High resolution in situ mapping of microstrain and microstructure evolution reveals damage resistance criteria in dual phase steels,” *Acta Materialia*, vol. 96, pp. 399–409, 2015.
- [127] M. Mills, J. Angelo, M. Daw, J. Weinburg, and D. Miracle, “Fine structure of  $a\langle 011 \rangle$  dislocations and the mechanical properties of NiAl in the hard orientation,” *Materials Science and Engineering: A*, vol. 192, pp. 134–141, 1995.

- [128] R. Srinivasan, M. Daw, R. Noebe, and M. Mills, "Observations of glide and decomposition of  $a\langle 101 \rangle$  dislocations at high temperatures in NiAl single crystals deformed along the hard orientation," *Philosophical Magazine*, vol. 83, no. 9, pp. 1111–1135, 2003.
- [129] R. Srinivasan, M. Savage, M. Daw, R. Noebe, and M. Mills, "Decomposition of  $a\langle 111 \rangle$  and  $a\langle 101 \rangle$  dislocations in hard-oriented NiAl single crystals," *Scripta Materialia*, vol. 39, no. 4-5, pp. 457–464, 1998.
- [130] W. Yang and R. Dodd, "Steady-State creep and associated microstructures in stoichiometric and non-stoichiometric polycrystalline NiAl," *Metal Science Journal*, vol. 7, no. 1, pp. 41–47, 1973.

# Lebenslauf

## Persönliche Daten

Name	LiKang Luan
Geburtsdatum	04. August. 1988
Geburtsort	Shanghai
Staatsangehörigkeit	China

## Schulbildung

1994 – 1999	Grundschule
1999 – 2003	Mittelschule
2003 – 2006	Shanghai Jiao Tong Gymnasium
	Abschluss: Allgemeine Hochschulreife

## Studium

2006 – 2010	Polymerwerkstoffe und -technik an der Shanghai Universität, Abschluss: Bachelor of Science (B.Sc.)
2012 – 2015	Materialwissenschaft und Werkstofftechnik am KIT, Abschluss: Master of Science (M.Sc.)

## Berufliche Tätigkeit

2015 – 2019	Akademischer Mitarbeiter am Karlsruher Institut für Technologie (KIT), Institut für Angewandte Materi- alien (IAM)
seit 2019	Entwicklungsingenieur bei Dantec Dynamics